Numerical Multi-physics Analysis of Fracture Reactivation in Geothermal Reservoirs from Microscale to Macroscale Modeling

From the Faculty of Georesources and Materials Engineering of the RWTH Aachen University

to obtain the academic degree of

Doktor der Ingenieurwissenschaften

approved thesis

submitted by
Josselin Noël Marcel Ouf, M.Sc

Advisors: Univ.-Prof. Dr. rer. nat. Florian Amann
Univ.-Prof. Dr. Philip James Vardon

Date of the oral examination: 05.03.2025

This thesis is available in electronic format on the university library's website

Abstract

Geothermal energy stands as a promising avenue for low-carbon energy production. Traditional methods involve extracting hot water into one well and the injection of cold water in another, with hydrothermal systems relying on fluid flow through either pores or natural fractures in rock. Enhanced Geothermal Systems (EGS) are deployed in fractured/faulted rock settings where fluid flow is insufficient, necessitating enhanced permeability of fractures for improved heat transfer. Challenges persist in ensuring productivity, sustainability, and safety, with fault and fracture reactivation presenting significant concerns.

Continuous fluid extraction induces changes in mechanics, temperature, and fluid pressure, impacting rock mass and joints behavior significantly. Faults and fractures may experience opening, extension, or sliding, posing computational challenges due to couplings and nonlinearity. Discontinuum models are often computationally expensive, particularly in addressing mechanical contact problems, leading to the use of 2D or partially coupled models.

This thesis proposes an Equivalent Continuum Modeling (ECM) approach to characterize thermo-hydro-mechanical processes in pre-existing fractures. By avoiding computationally intensive treatments, such as solving mechanical contact problems, ECM is able to deliver a fully coupled solution and a 3D approach, facilitating a more realistic capture of flow rates while eliminating simplifications such as plain strain or stress.

The approach has been implemented and benchmarked against hydro-mechanical laboratory data, confirming its accuracy in reproducing fracture pressure and flow rate. The impact of injection on permeability changes during fracture stimulation is

calculated, revealing a twofold increase in permeability, which is largely unrecoverable.

Upscaling the approach, it was benchmarked against mesoscale data and analytical solutions, further confirming its accuracy in reproducing fracture pressure and flow rate. Furthermore, the numerical reproduction and analysis of water circulation data exhibit high accuracy. Moreover, the impact of injection on permeability changes during fracture stimulation is calculated, revealing a tenfold increase in permeability, with a significant portion being recoverable.

Incorporating temperature into the framework, the investigation of the propagation of cooling fronts in hydrothermal systems is conducted, analyzing their effect on fault stress changes and discussing their implications. Lastly, the ruptured area of the reactivated fault is quantified, finding that an increase in fault stiffness increases the ruptured area.

Samenvatting

Geothermische energie is een veelbelovende techniek voor energieproductie met een lage koolstofuitstoot. Traditionele methoden omvatten het winnen van warm water in de ene put en het injecteren van koud water in een andere put, waarbij hydrothermische systemen vertrouwen op vloeistofstroming door poriën of natuurlijke breuken in gesteente. Enhanced Geothermal Systems (EGS) worden ingezet in gebieden met gebroken/gescheurd gesteente waar vloeistofstroming ontoereikend is, waardoor verbeterde permeabiliteit van de breuken nodig is voor een betere warmteoverdracht. Uitdagingen blijven bestaan op het gebied van productie, duurzaamheid en veiligheid, waarbij her-activering van breuken en scheuren aanzienlijke zorgen met zich meebrengt.

Continue vloeistofwinning veroorzaakt mechanische, temperatuur en vloeistofdruk veranderingen, wat een aanzienlijke invloed heeft op het gedrag van het gebroken /gescheurde gesteente. breuken en scheuren kunnen openen, verlengen of verschuiven, wat numerieke uitdagingen met zich meebrengt vanwege gekoppeld en niet-linear gedrag. Discontinuee-modellen zijn vaak rekenintensief, vooral bij het aanpakken van mechanische contactproblemen, wat leidt tot het gebruik van 2D- of gedeeltelijk gekoppelde modellen.

Dit proefschrift stelt een Equivalent Continuum Modeling (ECM) benadering voor om de thermo-hydro-mechanische processen in bestaande breuken te karakteriseren. Door het vermijden van rekenintensieve behandelingen, zoals het oplossen van mechanische contactproblemen, kan ECM een volledig gekoppelde oplossing bieden en een 3D-benadering, wat het realistischer vastleggen van stroomsnelheden mogelijk maakt, terwijl vereenvoudigingen zoals vlakke rek of spanning worden geëlimineerd.

De benadering is geïmplementeerd en getest aan de hand van hydro-mechanische laboratoriumgegevens, waarbij de nauwkeurigheid bij het reproduceren van breukdruk en stroomsnelheid is bevestigd. De impact van injectie op permeabiliteitsveranderingen tijdens breukstimulatie wordt berekend, waarbij een verdubbeling van de permeabiliteit wordt onthuld, die grotendeels onherstelbaar is.

Door de benadering op te schalen, is deze getest aan de hand van mesoschaalgegevens en analytische oplossingen, wat verdere bevestiging geeft van de nauwkeurigheid bij het reproduceren van breukdruk en stroomsnelheid. Bovendien laten numerieke reproductie en analyse van watercirculatiegegevens een hoge nauwkeurigheid zien. Verder wordt de impact van injectie op permeabiliteitsveranderingen tijdens breukstimulatie berekend, waarbij een verhoging van de permeabiliteit met een factor tien wordt onthuld, waarbij een aanzienlijk deel herstelbaar is.

Door temperatuur in het raamwerk op te nemen, wordt het onderzoek naar de uitbreiding van koelfronten in hydrothermische systemen uitgevoerd, waarbij hun effect op veranderingen in breuklijnpanning wordt geanalyseerd en hun implicaties worden besproken. Tot slot wordt het gebied van de gereactiveerde breuklijn die is gescheurd gekwantificeerd, waarbij wordt vastgesteld dat een toename van de breuklijnstijfheid het gescheurde gebied vergroot.

Zusammenfassung

Geothermie stellt eine vielversprechende Methode zur Erzeugung kohlenstoffarmer Energie dar. Traditionelle Methoden beinhalten das Extrahieren von heißem Wasser aus einer Bohrung und das Einleiten von kaltem Wasser in eine andere, wohingegen hydrothermale Systeme auf den Fluidfluss durch Poren oder natürliche Brüche im Gestein angewiesen sind. Verbesserte Geothermische Systeme (VGS) werden in geklüfteten/ gestörten Gesteinseinheiten eingesetzt, in denen der Fluidfluss unzureichend ist, und für eine bessere Wärmeübertragung eine erhöhte Permeabilität von Brüchen erforderlich ist. Die Herausforderungen bestehen darin, Produktivität, Nachhaltigkeit und Sicherheit zu gewährleisten, wobei die Reaktivierung von Brüchen und Störungen erhebliche Bedenken erheben.

Kontinuierliche Fluidextraktion induziert Veränderungen in der Mechanik, der Temperatur und dem Fluiddruck, die das Verhalten von Gesteinsmassen und Klüften signifikant beeinflussen. Brüche und Störungen können Öffnungen, Extension oder Gleiten erfahren, was aufgrund von Kopplungen und Nichtlinearitäten zu rechnerischen Herausforderungen führt. Diskontinuumsmodelle sind oft rechenaufwändig, insbesondere bei der Behandlung mechanischer Kontaktprobleme, was zur Verwendung von 2D- oder teilweise gekoppelten Modellen führt.

Diese Arbeit schlägt einen Ansatz des Äquivalenten-Kontinuum-Modellierens (AKM) vor, um thermo-hydro-mechanische Prozesse in bereits vorhandenen Brüchen zu charakterisieren. Durch Vermeidung rechenaufwändiger Behandlungen, wie der Lösung mechanischer Kontaktprobleme, ist AKM in der Lage, eine vollständig gekoppelte Lösung und einen 3D-Ansatz zu liefern, sodass eine realistischere Erfassung von Flussraten

ermöglicht wird während sie Vereinfachungen wie die reine Dehnung oder Spannung beseitigt.

Der Ansatz wurde implementiert und anhand von hydro-mechanischen Labordaten überprüft, wodurch seine Genauigkeit bei der Reproduktion von Bruchdruck und Flussrate bestätigt wurde. Der Einfluss der Injektion auf Permeabilitätsänderungen während der Bruchstimulation wird berechnet, wobei eine zweifache, größtenteils nicht wiederherstellbare, Zunahme der Permeabilität festgestellt wird.

Der Ansatz wurde durch Hochskalierung an mesoskaligen Daten und analytischen Lösungen überprüft, wodurch seine Genauigkeit bei der Reproduktion von Bruchdruck und Flussrate weiter bestätigt. Darüber hinaus zeigen die numerische Reproduktion und die Analyse von Wasserzirkulationsdaten eine hohe Genauigkeit. Außerdem wird der Einfluss der Injektion auf Permeabilitätsänderungen während der Bruchstimulation berechnet, wobei eine zehnfache Zunahme der Permeabilität festgestellt wird, wobei ein erheblicher Teil wiederherstellbar ist.

Durch die Integration von Temperatur in die Modellierungsumgebung wird die Ausbreitung von Abkühlungsfronten in hydrothermalen Systemen untersucht, wobei ihre Auswirkungen auf Änderungen der Bruchspannung analysiert und ihre Implikationen diskutiert werden. Schließlich wird die Bruchfläche der reaktivierten Störung quantifiziert und festgestellt, dass eine Steifigkeitserhöhung der Störung die Bruchfläche vergrößert.

Acknowledgements

I would like to convey my appreciation to my mentors at RWTH Aachen University, namely Prof.Dr.rer.nat. Florian Amann, Dr. Mohammadreza Jalali, and Dr.ing. Kavan Khaledi. Their expertise, guidance, and encouragement were indispensable in bringing this thesis to completion. Additionally, I extend my gratitude to Prof.Dr. Philip Vardon from Delft University of Technology for providing valuable technical guidance, encouragement and support. Special thanks to Aardyn BV. for hosting me and sharing their industrial knowledge.

I would like to express my sincere gratitude to all the members of the EASY-GO ITN project, the RWTH Aachen Chair of Engineering Geology and the Delft University of Technology Geoscience and Engineering Department. Their support has made my academic journey a truly pleasant experience. A heartfelt acknowledgment goes to my friends and family who have consistently supported me. I am deeply thankful for Christina's support and love throughout this journey.

This research was conducted within the scope of the EAGYGO-ITN project. I express gratitude for the financial assistance provided by the European Union's Horizon 2020 research and innovation program under the Marie-Curie grant agreement No 956965.

The doctoral research has been carried out in the context of an agreement on joint doctoral supervision between RWTH Aachen University, Germany and Delft University of Technology, the Netherlands.

Contents

Abstract **i**

Acknowledgements **x**

1 Introduction **1**

1.1 Rationale 1

1.2 Multiphysics of porous media 3

1.2.1 Behavior of rock mass 3

1.2.2 Behavior of discontinuities 6

1.2.3 Field obeservation and numerical modeling 7

1.3 Problem definition and motivation 9

1.3.1 Enhanced Geothermal Systems 9

1.3.2 Hydrothermal sytems 12

1.3.3 Scales 13

1.3.4 Research question 14

1.4 Overview of the thesis 15

2 Experimental and numerical analysis of injection-induced permeability changes in pre-existing fractures[a] 16

2.1 Introduction 17

2.1.1 Background 17

2.1.2 State-of-the-art in hydraulic stimulation 18

2.1.3 Objectives 21

2.2 Methodology 22
2.2.1 Methodology for the laboratory experiments 22
2.2.2 Methodology for the coupled HM-modeling 27
2.3 Results and discussion 37
2.3.1 Injection flow rate versus time 37
2.3.2 Flow rate versus injection pressure 41
2.3.3 Injection-induced permeability change 42
2.4 Summary and Conclusion 49

3 Numerical Modeling of Hydro-Mechanical Processes during Hydraulic Testing of Pre-existing Fractures at the Grimsel Test Site, Switzerland[b] 51
3.1 Introduction 52
3.2 Grimsel Test Site 55
3.3 HS1 stimulation 56
3.4 Modeling approach 58
3.4.1 Fully coupled numerical simulator 58
3.4.2 Model Set up 59
3.4.3 Hydraulic & mechanics formulations 62
3.4.4 3D FE modeling of the experiments 62
3.5 Simulation results 64
3.6 Discussion and conclusion 74

4 Numerical Analysis of Far-Field Fault Reactivation Induced by Reservoir Cooling[c] 76
4.1 Introduction 77
4.2 Modeling approach 81
4.2.1 Fully coupled numerical simulator 81
4.2.2 Coupled thermo-hydro-mechanical equations 81
4.2.3 Model Set up 83

4.2.4 Slip Tendency . . . 88
4.2.5 Limitations . . . 89
4.3 Results . . . 89
4.3.1 Reservoir pore pressure and temperature . . . 90
4.3.2 Stress changes within the reservoir . . . 91
4.3.3 Stress changes at the fault . . . 92
4.4 Discussion . . . 101
4.4.1 Fault reactivation . . . 101
4.4.2 Hazards . . . 102
4.5 Summary and Conclusion . . . 103

5 Conclusions & Future Perspectives 105
5.1 Efficiency of Enhanced Geothermal Systems . . . 105
5.2 Safety in Hydrothermal Systems . . . 107
5.3 Future Perspectives . . . 108

References 110

A List of publications, conferences attendances and organised 134

B Curriculum Vitae 138

List of Tables

2.1 Hydro-mechanical parameters used in the numerical models 37

2.2 Input model parameters for the fracture permeability function 37

3.1 Injection steps within cycle 4 of HS1 58

3.2 Hydromechanical properties of the model. Properties were adopted from Doetsch et al. [2018][a], Keusen et al. [1989a][b], Nagra NIB 95-062 [c] and Krietsch et al. [2020][d]. 61

3.3 Parameters of the permeability function for the fault zone S1.3 61

4.1 Thermal, hydraulic and mechanical properties of the rock. Properties are based on Buijze et al. [2023] 86

4.2 Fluid properties of the model. Properties from International Association for the Properties of Water and Steam Wagner and Pruß [2002] 86

4.3 Parameters of the different scenarios modeled. Properties are based on Buijze et al. [2023] 87

List of Figures

1.1 Average life cycle greenhouse gas emissions. Source - IPCC [2014] . . . 2
1.2 Conceptual integration of Thermal, Hydraulic and Mechanical couplings 5
1.3 Fracture stimulation (a) Hydraulic fracturing achieved by injecting fluid at a pressure exceeding the intact rock tensile stress, (b) Hydro-shearing is on pre-existing fractures at a pressure that exceed fracture failure line [Gischig and Preisig, 2015]. 11

2.1 Figure showing the overall objectives of this study including 1) design and perform laboratory experiments that scale down the hydraulic shearing process, 2) develop numerical models capable of reproducing the injection-induced permeability change in pre-existing fractures 23
2.2 A schematic representation of triaxial testing setup for hydro-shearing; a) a granite block with a vertical fault plane is shown. The fluid is injected through a borehole with a diameter of 20 mm. Water can flow out at the fault boundaries. The injection interval is isolated by a double packer system; b) the injection unit consisting of a flow pump and a pressure transducer; c) the true triaxial loading apparatus 24
2.3 Injection protocols for the conducted hydraulic stimulation tests along with the adopted injection pressure in the numerical simulations; a) Test 1, isotropic loading/smooth fracture; b) Test 2, isotropic loading/rough fracture; c) Test 3, shear loading/rough fracture; d) Test 4, shear loading/rough fracture 26

2.4 a) Slip-weakening Mohr-Coulomb model to describe the frictional strength of the fracture zone; b) Schematic representation of the non-linear flow rate in a fracture as a result of fuild injection, modified after Krietsch et al. [2020] 29
2.5 a) Hydro-mechanical boundary conditions for the numerical modeling of the fluid injection tests; b) the finite element mesh of the granite block and fracture zone 30
2.6 Mesh convergence; a) Test 1, smooth fracture flow rate; b) Test 2, 3, 4, rough fracture flow rate; c) Test 3, 4, rough fracture equivalent plastic strain 34
2.7 Flow rate evolution obtained during hydraulic stimulation tests along with the numerical modeling results; a) Test 1, isotropic loading/smooth fracture; b) Test 2, isotropic loading/rough fracture; c) Test 3, shear loading/rough fracture; d) Test 4, shear loading/rough fracture 36
2.8 Flow rate versus injection pressure along with the numerical modeling results; a) Test 1, isotropic loading/smooth fracture; b) Test 2, isotropic loading/rough fracture; c) Test 3, shear loading/rough fracture; d) Test 4, shear loading/rough fracture 40
2.9 Changes in hydraulic aperture and effective normal stress obtained from numerical modeling; a) hydraulic aperture in Test 1, isotropic loading/smooth fracture; b) hydraulic aperture in Test 2 c) hydraulic aperture in Test 1, isotropic loading/smooth fracture; d) hydraulic aperture in Test 2 44
2.10 Changes in hydraulic aperture and permeability of fracture obtained from numerical modeling; a) hydraulic aperture in Test 1, isotropic loading/smooth fracture; b) hydraulic aperture in Test 2, isotropic loading/rough fracture; c) permeability in Test 1, isotropic loading/smooth fracture; d) permeability in Test 2, isotropic loading/rough fracture . . 45

2.11 Changes in hydraulic aperture and permeability of rough fracture obtained from numerical modeling; a) hydraulic aperture in Test 3; b) hydraulic aperture in Test 4; c) permeability change in Test 3; d) permeability change in Test 4 47

2.12 a) The contour plot of normal effective stress on the fracture plane for Test 3; b) the distribution of normal effective stress along a horizontal line passing through; c) the initial effective stress state in Test 3 and the required condition to satisfy the Mohr-Coulomb failure condition; d) the fracture A vertical cut though the fracture showing contour plot b_{shear} value in Test 3 48

3.1 Grimsel In-situ Stimulation and Circulation Test Site - Modified after Krietsch et al. [2018] 56

3.2 In-situ Injection INJ2: Six Injection Steps of Cycle 4 Post-Stimulation Phase - Modified from Krietsch [2019] 57

3.3 Numerical model with boundary conditions and location of PRP2 and INJ2 60

3.4 The mesh of fault within the model showing a refined area around the injection point 63

3.5 Mesh convergence study for plastic strain and pore pressure 64

3.6 Tangential plastic strain at mesh density; a) 428 192 elements b) 508 132 elements c) 646 644 elements d) 715 056 elements 65

3.7 a) Injection pressure at INJ2, b) Flow rate at INJ2, c) Fracture pressure at PRP2 67

3.8 Flow rate vs Injection pressure at INJ2 68

3.9 Fracture permeability and aperture change; a) Aperture variation over time at INJ2, b) aperture variation over time at PRP2, c) permeability change at INJ2, d) permeability change at PRP2 69

3.10 Fracture pressure at different steps; **a)** Step 1 : Injection pressure 2.33 MPa; flow rate 1.82 l/min; time 680 s, **b)** Step 2: Injection pressure 3.07 MPa; flow rate 3.26 l/min; time 1260 s, **c)** Step 3: Injection pressure 3.51 MPa; flow rate 4.3 l/min; time 1720 s, **d)** Step 4: Injection pressure 4.27 MPa; flow rate 6.57 l/min; time 2080 s **e)** Step 5: Injection pressure 5.37 MPa; flow rate 15.00 l/min; time 2730 s , **f)** Step 6: Injection pressure 6.45 MPa; flow rate 25.00 l/min; time 3000 s 72

4.1 Diagram illustrating stress changes in a geothermal reservoir [Vardon, 2024] (Personal Communication): a) Components contributing to the final stress state; b) Mohr's circle and failure envelope demonstrating thermo-hydro-mechanical stress alterations. Line colors/types in (a) correspond to Mohr's circles in (b). 79

4.2 Model domain and geometry 84

4.3 Boundary conditions of the model (locations of the cross-sections refer to Fig. 2 at the center-point of the Y and X axes of the domain, respectively): a) Cross-section XZ , b) Cross-section YZ. 87

4.4 Nodes and meshes: a) Reservoir cross section, b) Fault 88

4.5 Distribution inside the reservoir of a) Pore pressure, b) Temperature.Distance is along the scan line in figure 4.2 91

4.6 Plan view of stresses at the center of the reservoir after 27.5 years of injection a) σ'_{xx} - Scenario 1 b) σ'_{zz} - Scenario 1 c) σ'_{xx} - Scenario 3 d) σ'_{zz} - Scenario 3 92

4.7 a) Temperature and pore pressure at middle of the fault b) Tangential shear stress acting on the middle of the c) Normal effective stress acting on the middle of the fault d) Fault Slip Tendency Evolution 94

4.8 Representation of effective stress evolution at the middle of the fault at Z = -3470m with Mohr's Circles; a) Scenario 1, b) Scenario 2, c) Scenario 3, d) Scenario 4 95

4.9 Fault slip tendency: a) Initial Condition b) Scenario 1 - 27.5 years production c) Scenario 2 - 27.5 years production d) Scenario 3 - 27.5 years production e) Scenario 4 - 27.5 years production f) Scenario 1 - 55 years production g) Scenario 2 - 55 years production h) Scenario 3 - 55 years production i) Scenario 4 - 55 years production 100

4.10 Ruptured area of the fault for different fault stiffness 101

Nomenclature

α	Stress dependency coefficient [1/Pa]
α_b	Biot-Willis coefficient [-]
β	Volumetric thermal expansion coefficient [1/°C]
λ	Thermal conductivity [W/°C·m]
$\mathbb{C}$	Constitutive behaviour tensor [Pa]
μ	Viscosity [Pa/s]
ν	Poisson's ratio [-]
ϕ_0	Static Friction angle [°]
ϕ_r	Residual friction angle [°]
ψ	Dilation angle [°]
ρ	Density [kg/m^3]
σ_n	Normal stress [Pa]
τ	Shear stress [Pa]
ε	Strain tensor [%]
ε_{ps}	Equivalent plastic shear strain [%]

ε_{vol} Volumetric strain [%]

ε^p Plastic strain [%]

ξ Thermal energy per unit volume [J/m^3]

σ Cauchy stress tensor [Pa]

σ' Effective stress tensor [Pa]

b_{el}^{max} Maximum elastic opening [m]

b_h Hydraulic aperture [m]

b_{ini} Initial fracture opening [m]

b_{shear} Irreversible aperture [m]

b_{shear}^{max} Maximum shear opening [m]

C Specific heat capacity [J/kg·°C]

c Cohesion [Pa]

E Young's modulus [Pa]

F^T Heat flux [W/m2]

G Shear modulus [Pa]

g Gravitational acceleration [m/s^2]

g_p Plastic flow potential [Pa]

h Enthalpy [J]

K Bulk modulus [Pa]

k Permeability tensor [m^2]

k_f	Fracture permeability [m^2]
n	Porosity [%]
p_f	Pore pressure [Pa]
q_f	Darcy velocity [m/s]
R	Softening rate [-]
s_f	Fracture spacing [1/m]
ST	Slip tendency [-]
T	Temperature [°C]

Chapter 1

Introduction

1.1 Rationale

The global demand for heating and electricity production has surged in tandem with the growth of the world population. The escalating interest in utilising low carbon emission technologies for heat and electricity production positions geothermal energy as a contender to provide a major contribution to addressing this challenge. Additionally, several countries are actively advocating for a reduction in their reliance on nuclear energy. Geothermal energy emits only an average of 38 g of CO_2 per kW/h of energy produced, making it one of the lowest carbon-emitting technologies, as shown in Figure 1.1 IPCC [2014]. Geothermal technology can be used globally, with different technologies suiting different geological locations and energy demand characteristics. It requires minimal land surface and requires limited resources and raw materials, fostering energy self-sufficiency and reducing reliance on foreign resources.

Geothermal energy has been utilised for millennia, primarily for heating and various thermal applications. A significant milestone in its commercial utilisation occurred with the construction of the world's first geothermal power plant in Lardarello, Italy, in 1913 [Parri and Lazzeri, 2016]. The advent of steam power generation systems marked the beginning of worldwide endeavors to harness geothermal energy. In Iceland, Einarsson [1942] pioneered the first fluid circulation-dominant geothermal system, and in

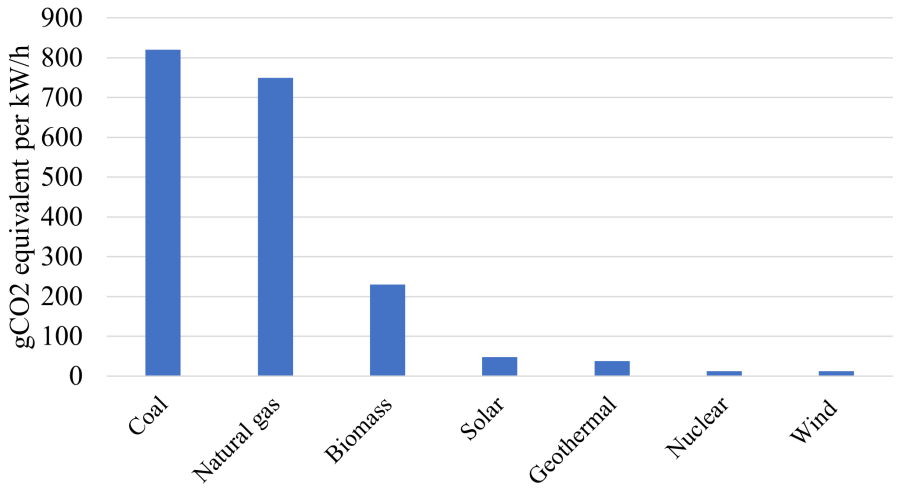


Figure 1.1: Average life cycle greenhouse gas emissions. Source - IPCC [2014]

the 1960s, significant exploration and development efforts were made. The first power plants commissioned in the USA were at The Geysers in California, while extensive study programs were initiated in other part of USA, Turkey, Mexico, Japan, Chile, El Salvador [Grant, 2013]. As of 2021, the global production of electricity from geothermal sources reached 15.96 gigawatts electric (GWe). Additionally, in 2020, the deployment of geothermal energy for heating and cooling purposes amounted to 107 gigawatts thermal (GWth) [IRENA, 2023].

Geothermal energy production can be economically competitive compared to other technologies. Based on data from the US National Renewable Energy Laboratory (2022), the cost per kilowatt-hour (kW/h) for geothermal energy ranges from $0.055 to $0.396. In comparison, biomass costs around $0.144 per kW/h, solar energy ranges from $0.031 to $0.366 per kW/h, and nuclear power costs $0.081 to $0.082 per kW/h. Another challenge facing the widespread adoption of geothermal energy is its public acceptance. A number of projects have resulted in induced seismic activity, prompting the shutdown of geothermal operations [Kim et al., 2018, Häring et al., 2008, Vörös and Baisch, 2022]. This seismicity has raised public concern and fostered a 'not in my backyard' effect, hindering the initiation of additional geothermal projects [Baria et al., 2007].

This thesis contributes to advancing geothermal energy by focusing on the simulation of fracture reactivation in geothermal reservoirs, both for enhancing and controlling water flow in fractured reservoirs and for the impact of reservoir cooling on faults. This endeavor aligns with the global goal of improving the cost-effectiveness and safety of geothermal energy. Ultimately, this can bolster public acceptance of geothermal technology.

1.2 Multiphysics of porous media

1.2.1 Behavior of rock mass

Porous media such as rocks, soils, or powders, consist of a solid phase forming the skeleton of the material and pores which contain fluid(s). The characteristics of the solid skeleton are determined by petrofabric properties [Turner and Weiss, 1963], and influence the behavior of the material. The pores often host one or more fluids, such as gas, water, oil or brine. The interaction between the solid and fluid phases results in coupled multi-physics problems. Additionally, changes in temperature can significantly alter the behavior of a porous media. The concept of thermo-poroelasticity involves a dynamic interplay between changes in temperature, mechanics, and hydraulics. Alterations in temperature lead to corresponding changes in mechanics and hydraulics. Similarly, adjustments in hydraulics induce changes in both thermal and mechanical aspects, while modifications in mechanics result in concurrent changes in hydraulics and thermal propertie. Hence, a thorough examination of rocks necessitates understanding of thermal, hydraulic, and mechanical behavior, including the intricate relationships and interactions among them. These interdependencies are illustrated in Fig. 1.2, highlighting the interconnected nature of these factors in shaping the behavior of geological materials

Energy obeys the law of conservation, meaning that the total energy within an isolated system remains finite. Within this framework, thermal energy involves heat

transfer, e.g. by conduction, a process where heat transfers from a hotter region to a cooler one within a continuous medium. Temperature and heat flow are interconnected, determined by factors such as the mass of the objects involved, the temperature change, and the specific heat capacity of those objects (see Fig. 1.2).

Hydraulic behaviour operates under the law of conservation of mass, where the total mass within an isolated system remains constant. Fluid velocity is determined by factors such as permeability, fluid viscosity, porosity, and the gradient of pore pressure. In groundwater flow analyses, laminar flow is often assumed as the dominant condition. Ground flow is considered laminar if the Reynolds number is below 1 [Murthy, 1989]. Fluid kinetics are defined by pressure-driven flow, which is influenced by pore geometry, pressure, and flow rate (see Fig. 1.2).

Mechanics encompasses managing both linear and angular momentum to maintain symmetry within the tensor and uphold the general principle of equilibrium. Strain and displacement relationships are typically linearized, assuming small strain behaviour, which may be typically below 1 % strain [Malvern, 1969, Bower, 2009]. For strains exceeding this threshold, a nonlinearized large strain formulation is commonly adopted. The constitutive behaviour establishes the link between stress and strain, which can result in fully reversible strain in elasticity, irreversible strain in plasticity or irreversible brittle strain. Meanwhile, the compatibility equation ensures the compatibility among all infinitesimally small components (see Fig. 1.2).

The initial exploration of the coupling between fluid and solid was undertaken by Terzaghi [1943], who applied Archimedes's theory to soil mechanics and introduced the concept of effective stress. Subsequent advancements in this concept were made by Skempton [1954] and Biot [1955]. Building upon these foundations, Geertsma [1957a] and Zimmerman [1990] further developed the understanding of the interactions between fluid and solid phases, specifically addressing changes in porosity resulting from changes in fluid pressure and/or stress conditions. The permeability of porous materials can be influenced by strain, and this relationship has been explored in laboratory experiments. Researchers such as Fatt and Davis [1952], Bernabe [1986], Han and Dusseault

[2003], integrated these experiments into mathematical models for reservoir simulation.

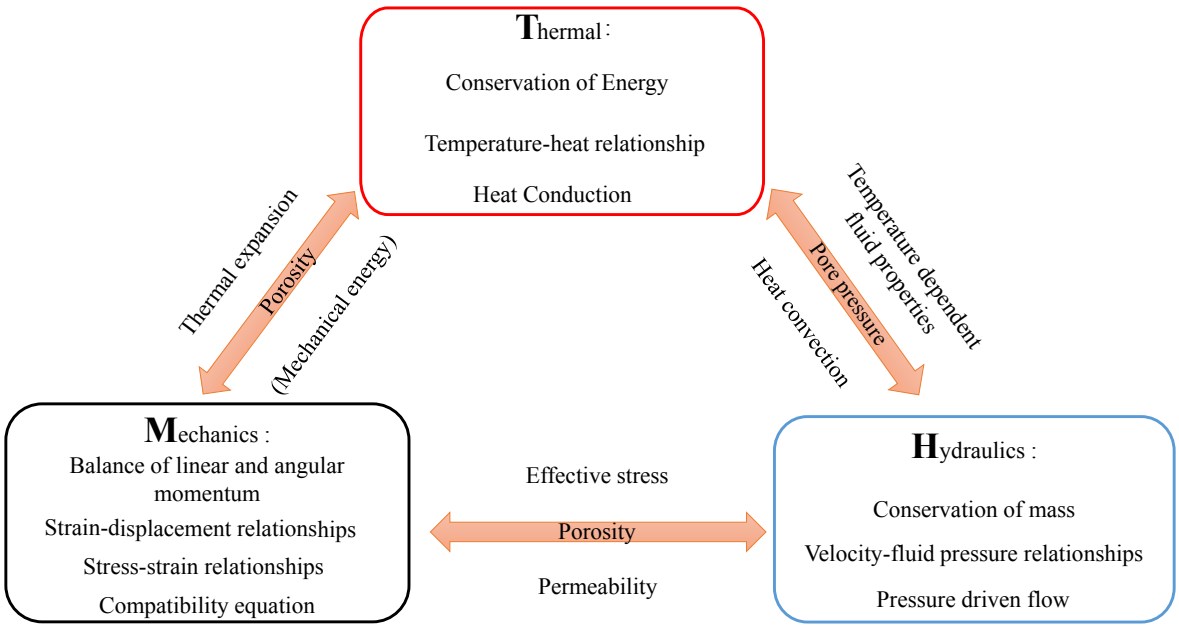


Figure 1.2: Conceptual integration of Thermal, Hydraulic and Mechanical couplings

The inception of thermo-elasticity traces back to Duhamel [1832], who demonstrated the influence of temperature on stress. The development of linear thermo-poroelasticity, integrating the mechanics of porous media and temperature, followed a similar trajectory as the coupling between fluid and solid, as highlighted by Geertsma [1957b]. Linear theories in this field were further refined by McTigue [1986], Palciauskas and Domenico [1989], focusing on saturated porous rock. Ongoing research is now directed towards the exploration of non-linear and thermodynamically consistent thermo-poroelasticity and plasticity [Puzrin, 2012, Ma et al., 2017, Golchin et al., 2021, 2022]. It is worth noting that in many instances, changes in internal energy induced by mechanical deformation that occurs during plasticity are often overlooked.

A major hydraulic and thermal coupling is heat advection, i.e. the thermal energy carried by a fluid moving. This process is governed by Darcy's law, with the quantity of energy governed by the internal enthalpy of the fluid phase. Experiments conducted at various scales demonstrate that alterations in temperature significantly impact fluid properties, as noted by Wagner and Pruß [2002]. Another facet of hy-

drothermal coupling encompasses fluid expansion resulting from thermal increments, leading to variations in pore pressure, as investigated by Ghabezloo and Sulem [2009].

1.2.2 Behavior of discontinuities

Rock masses are further characterized by the presence of joints and faults, wherein fluid is commonly found. Joints represent fractures and cracks that have undergone minimal or no transverse displacement [Price, 2016]. Closely spaced joints may be seen as an integral aspect of the rock fabric. Additionally, micro-cracks can also be considered inherent features within the rock fabric itself. To determine whether joints and micro-cracks can be considered inherent to the rock mass itself, researchers employ an index known as the Representative Elementary Volume (REV) [Long et al., 1982], where both the scale of the discontinuities and the scale of the problem considered are important. Oda [1988] proposed a method for assessing the REV based on surveys of joints within rock masses. In tunneling studies, Palmstrom [1995] introduced a concept similar to REV called the Continuity Factor (CF) concept. It serves to determine whether a discontinuity should be considered as part of the rock matrix. These methodologies take into account the scale of investigation, and based on certain criteria, discontinuities are either integrated into the rock matrix or treated as individual features.

Faults, on the other hand, are fracture surfaces where relative displacement has occurred transverse to the fracture. While faults are typically considered to be individual structures, they can amalgamate into fault zones, with thickness ranging from approximately 10 meters to 1 kilometer [Myers and Aydin, 2004]. Within these fault zones, one or more gouges are often present. Joints and faults gouge can be clean or filled with very fine crushed particles or even sealed [Mandl, 2005].

The joints and fault properties such as stiffness and permeability are dependent on the geometry of fractures. Since the actual geometry of discontinuities is often too complex for practical engineering considerations, a common simplification is to

treat each discontinuity as two parallel planar rock surfaces. This simplification is commonly referred to as the "parallel plate assumption" [Snow, 1965]. The fluid flux through a fracture, modeled with a parallel plate assumption, can be computed using the linearised Navier-Stokes equations. The fracture transmissivity is expressed as proportional to the cube of the aperture, as established by Witherspoon et al. [1980], Zimmerman and Bodvarsson [1996]; this relationship is commonly referred to as the "cubic law". Witherspoon et al. [1980] shows that the cubic law in marble fractures is not valid in the high-stress regime, where apertures are relatively small. However, in the medium and low-stress regimes, the law remains valid. The hydraulic behavior of a fracture is significantly influenced by the effective stress acting on the fracture, which both impact the aperture as highlighted by Cook [1992].

Laboratory tests have been conducted to investigate discontinuity closure, as discussed in studies by Goodman [1976], Bandis et al. [1983]. These studies reveal that discontinuity closure is influenced by the normal stress applied to the discontinuity and the normal stiffness of the discontinuity. Mated joints (i.e., joints that fit together precisely) have been observed to experience less closure than unmated joints. The shear displacement of fractures was examined at the laboratory scale by Goodman [1976], Olsson and Barton [2001]. Their study revealed that fractures often dilate during shearing, attributed to the presence of asperities where two sides of a fracture slide over each other. When these asperities overlap, an irreversible process named asperity locking takes place. Fracture sliding depends on friction coefficient and the applied shear stress.

1.2.3 Field obeservation and numerical modeling

The Groß Schönebeck facility in Germany serves as a geothermal research center focusing on various geothermal studies. The rock mass at this facility predominantly consists of sandstone. Several experiments have been conducted to assess and characterize the behavior of the rock mass and its discontinuities [Reinicke et al., 2005, Huenges,

2002]. Of particular interest are experiments on fracture stimulation [Zimmermann and Reinicke, 2010], which revealed the complex response of fractures to hydraulic stimulation in real reservoir settings. This study was further analyzed numerically by Jacquey et al. [2015], demonstrating that the opening of a large hydraulic fracture induces compression in the vicinity of the stimulated well, leading to a significant pore pressure response.

In Newberry Volcano, Oregon, USA various experiments have been conducted in Enhanced Geothermal System (EGS) system [Sammel et al., 1988]. The stimulation and production processes associated with EGS created significant perturbations to the physical and chemical environment, leading to coupled Thermal-Hydrological-Mechanical-Chemical (THMC) phenomena. Various experiments have been conducted to assess and characterize the behavior of the rock mass and its discontinuities [Sonnenthal et al., 2012]. Of particular relevance is the hydraulic shearing study by Petty et al. [2013], which investigated how different fractures responded to various injection scenarios. Rinaldi et al. [2015] investigated this experiment numerically to examine the extent of the simulation zone under fully and partially saturated conditions.

In Mont Terri, Switzerland, various experiments have been conducted to investigate the behavior of rock masses and discontinuities within an underground rock laboratory (URL) containing Opalinus Clay [Bossart et al., 2018]. Following an extensive campaign characterizing the geological settings and rock properties, diverse thermo-hydro-mechanical-chemical coupled processes were studied for geothermal applications [Bossart et al., 2018]. Additionally, several fault reactivation procedures were carried out at the field scale (meter-scale) [Guglielmi et al., 2017, 2020], revealing complex hydromechanical behavior of the faults. Notably, these reactivations showed significant increases in permeability associated with relatively small, sub-millimeter slip movements. Further analysis, conducted by Rutqvist et al. [2020], extended these findings numerically, comparing different numerical approaches based on the data from fault reactivations. The results demonstrated that various numerical methods can accurately reproduce the observed field behavior.

At other underground laboratories such as Grimsel, Switzerland, various experiments have been undertaken to evaluate and understand the behavior of rock masses and their discontinuities [Amann et al., 2018]. Of particular interest are experiments on fracture stimulation conducted by Krietsch et al. [2020]. These tests have revealed insights into water circulation, rock deformation, and seismic behavior resulting from stimulation. At a larger scale, similar experiments are currently being conducted at Bedretto, Switzerland [Ma et al., 2021]. Furthermore, there are ongoing efforts to develop geothermal facilities aimed at gathering more data and exploring new experimental scenarios, such as the campus geothermal well in Delft, the Netherlands [Vardon et al., 2020].

1.3 Problem definition and motivation

In this thesis, I have concentrated on the numerical modeling of the coupled thermal, hydraulic and mechanical behavior of discontinuities in Enhanced Geothermal Systems (EGS) and hydrothermal systems.

1.3.1 Enhanced Geothermal Systems

Deep geothermal energy, is a promising technology for sustainable power generation, in most locations harnessed from depths of 3 to 5 kilometers below the Earth's surface within the continental crust [Amann et al., 2018]. To be economically viable, the temperature at these depths should exceed 120°C [Hirschberg et al., 2014, Saar, 2017]. However, the challenge lies in the limited permeability and porosity of the reservoir at such depths, hindering efficient fluid circulation [Manning and Ingebritsen, 1999]. At these depths, fluid tends to flow primarily through fractures rather than the rock matrix.

In the 1970's, efforts to enhance the permeability of such systems led to the development of Enhanced Geothermal Systems (EGS), starting at Fenton Hill, USA [Breede et al., 2013]. The core concept behind EGS involves boosting the system permeability

by injecting fluids into fractures for a short period before beginning production. This injection process includes hydraulic fracturing, where new fractures are created, and hydraulic shearing, which involves reactivating pre-existing fractures through shear sliding [Amann et al., 2018, Luo et al., 2023]. Fractures can be improved either through Hydraulic Fracturing (HF), leading to the creation of new fractures or the extension of pre-existing ones, or through Hydraulic Shearing (HS), resulting in the enhanced permeability of pre-existing fractures [Gischig and Preisig, 2015]. Fig.1.3 shows both of these processes.

In HF, water is injected until it induces tensile failure, causing the rock to crack. This process is usually followed by the injection of proppant to maintain the fracture's openness. Fig. 1.3a shows schematically this processes and the accompanying Mohr's circle, which must move leftwards until meeting the tensile limit of the intact rock. On the other hand, HS involves injecting water into existing fractures until they reaches shear failure, causing the rock to slide and dilate, with the Mohr's circle moving leftwards to intersect the shear failure surface of the fracture, as shown in Fig. 1.3b. This sliding and dilation in HS are accompanied by asperities locking, which helps to keep the fracture open upon fluid pressure release, as discussed in studies such as Pine and Batchelor [1984], Cladouhos et al. [2009]. Notably, these mechanisms often occur simultaneously, as highlighted in the work of McClure and Horne [2014], Gischig and Preisig [2015].

EGS (Enhanced Geothermal Systems) offers a crucial advantage in the ability to utilise diverse geological environments, enabling widespread implementation globally. However, several EGS projects have faced setbacks due to inadequate site investigation and characterization or a lack of physical understanding of the system. For instance, the Fenton Hill project in the USA (1974–1995), situated in a granite rock setting, aimed to create a reservoir at a depth of 4.4 km with a temperature of 300°C and test a 60 kWe binary cycle power generation system. Despite efforts, the project was terminated due to an inability to achieve the expected capacity [Panel, 2006]. Similarly, the Rosemanowes project in the UK (1977–1991) focused on granite rocks and aimed to maintain a flow capacity of 50–100 kg/s over a 5-year operational period without

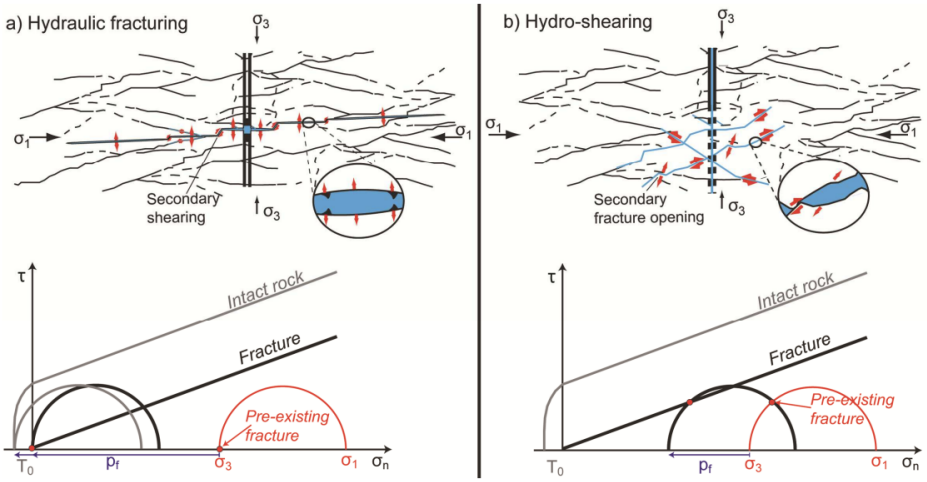


Figure 1.3: Fracture stimulation (a) Hydraulic fracturing achieved by injecting fluid at a pressure exceeding the intact rock tensile stress, (b) Hydro-shearing is on pre-existing fractures at a pressure that exceed fracture failure line [Gischig and Preisig, 2015].

temperature decline. However, the reservoir's dependence on natural fractures led to difficulties in fluid flow control, with fluid loss exceeding 70% [Law, 2011]. In Japan, the Hijiori project (1981–1986) marked Japan's first EGS site, demonstrating a 130 kWe binary power system. Despite achieving a maximum temperature of 250°C at a depth of 180 0m, fluid loss surpassed 70%, even with injection and production wells merely 50 m apart [Panel, 2006]. In Basel, Switzerland (2005–2006), a hydraulic fracturing test conducted at approximately 5000 m depth and 200°C temperature triggered numerous micro-earthquakes, prompting the test's premature halt. Subsequently, a magnitude 3.4 earthquake caused damage to local structures mere hours after injection ceased [Lu, 2018].

Some geothermal project have achieved success due to comprehensive characterization and design. For instance, the Soultz-sous-Forêts project in France (1987-present) stands out as the first commercial-scale EGS power plant in the country, boasting an installed capacity of 1.5 MWe. With a production flow capacity of 25 kg/s, Soultz-sous-Forêts EGS operates as a commercially viable geothermal power plant by leveraging an artificially fractured reservoir. The success of this endeavor hinged on site characteristics, particularly the natural fissures and their interconnectedness, as highlighted

in Lu [2018].

In this thesis, I have focused on reproducing numerically HS with a focus on coupling hydraulics and mechanics. Other authors have investigated the coupled processes of HS at large scale in various EGS project sites, with noteworthy instances such as Soultz-sous-Foret in France [Baisch et al., 2010], Fenton Hill in New Mexico, USA [Rinaldi and Rutqvist, 2019], Groß Schönebeck in Germany [Blöcher et al., 2018] and Pohang in South Korea [Yoo et al., 2021]. There is a scarcity in the literature regarding numerical modeling that accurately replicates smaller-scale hydraulic shearing (HS), where experimental conditions are well-characterised and experimental results are closely monitored [Amann et al., 2018, Rinaldi and Rutqvist, 2019].

1.3.2 Hydrothermal sytems

A hydrothermal system involves the hot fluid extraction and cold fluid (re)injection into a porous and permeable hot aquifer, with the extraction of the heated fluid taking place in another well. Typically found at depths of 1 to 4 kilometers, these systems typically exhibit temperatures ranging from 20 to 160°C in sedimentary rocks [Piesnack, 2023, Buijze et al., 2023]. The relatively high permeability and porosity of the aquifer enable the injection and extraction of fluids at elevated flow rates. While hydrothermal systems have traditionally found application in heating and cooling applications, recent advancements in the Organic Rankine Cycle have unveiled their potential to play a pivotal role in electricity generation [Tchanche et al., 2014]. Despite being primarily feasible in sedimentary or volcanic settings, this technology is utilised globally. Hydrothermal systems are more utilised than EGS because the drilling depth required for hydrothermal is typically shallower compared to EGS, resulting in lower drilling costs, and reduced technical complexity. Additionally, unlike EGS which often requires extensive fracture stimulation to enhance permeability and heat extraction, sedimentary or volcanic geothermal reservoirs often possess naturally occurring permeability, facilitating the extraction of heat without the need for costly and technically challenging

stimulation techniques.

Controlling fault reactivation is critical for the successful development of geothermal energy. Cold water injection in hydrothermal system can cause fault reactivation leading to micro-seismicity [Moeck et al., 2009a, Deichmann and Giardini, 2009]. In a study by Jacquey et al. [2015], analysis of a synthetic case revealed that a fault positioned between an injector and a producer well tends to experience slipping predominantly as a consequence of thermal effects, rather than pore pressure effects. Conducting a numerical poro-thermo-elasticity study, [Jacquey et al., 2016] focused on assessing how changes in pore pressure and temperature influence the stability of a fault at the Groß Schönebeck geothermal site. The study emphasised the importance of incorporating thermo-poroelastic coupling to accurately model a geothermal scenario. Moreover, Kivi et al. [2022] demonstrated in a 2D synthetic model that faults located 1 km away from the injector and producer can undergo reactivation primarily due to thermal effects. In this scenario, stress change results from reservoir contraction, as the cooling front does not reach the faults. There is a limited amount of papers in the literature investigating fault reactivation due to long term cooling.

1.3.3 Scales

In this framework, I have explored coupled physical processes concerning different time and length scales. The study of discontinuities inherently requires the investigation of dynamic processes, varying across both time and space. Observing certain properties becomes feasible at specific spatial scales, while others remain inaccessible. Monitoring rock mass and discontinuities at a high resolution is often unattainable at the reservoir scale. In contrast, achieving a high spatial density of monitoring is more manageable at the meso-scale and laboratory scale.

At the laboratory scale (cm), precise control of settings and high sensor density provide detailed insights. However, this scale only represents a limited behavior, typically involving a single fracture with a restricted amount of rock mass. The initial

knowledge, encompassing the stress tensor, permeability, pore pressure, and temperature, is precisely measured with minimal spatial variation. Moving to the meso-scale (deca-meter), the spatial density of monitoring remains accurate. Nevertheless, measuring initial conditions such as the stress tensor, permeability, pore pressure, and temperature is well-executed, but non-homogeneity often exists across experimental settings. At the kilometer-scale, reservoir processes extend beyond localized effects, impacting a larger area and volume, which enhances accuracy. However, obtaining data and establishing a high sensor density pose significant challenges. Additionally, initial conditions are typically highly non-homogeneous.

Numerical simulations are well-suited for investigating coupled physics occurring at various scales. They prove instrumental in deriving equations that can effectively bridge different time and length scales across diverse settings, accounting for various initial conditions and heterogeneities.

1.3.4 Research question

Following on from the gaps in the literature mentioned above and the need for development of geothermal energy I have selected the following questions:

1. What physical processes drive hydraulic shearing on a small scale? How can I incorporate them into a numerical simulator to give accurate predictions?

2. Is it possible to leverage the observed physical processes of hydraulic shearing at a small scale to simulate meso-scale reservoirs? How does water propagate within a fracture during hydraulic shearing?

3. How does the cooling of a reservoir induce reactivation of faults in the far-field? What mechanisms contribute to far-field fault activation, and how sensitive is fault reactivation to changes in stiffness?

1.4 Overview of the thesis

This section presents the overview of thesis. The questions mentioned above are tackled in each chapter.

Chapter 2: This chapter presents a dual approach, combining laboratory experiments produced by another Ph.D. candidate and numerical modeling, to investigate injection-induced permeability changes in pre-existing fractures. The study replicates hydraulic stimulation of natural fractures and faulted zones through a pressure-controlled fluid injection experiment in a laboratory-scale granite block under true triaxial stress conditions.

Chapter 3: This study upscales the fully coupled hydro-mechanical framework developed in the previous chapter to model hydraulic shearing in a mesoscale reservoir in Grimsel, Switzerland. The experiment focuses on a ductile-brittle fault within non-permeable granite.

Chapter 4: This study presents a thermo-hydro-mechanical framework tailored for modeling hydrothermal systems within a faulted synthetic reservoir, reflecting current production scenarios in the Netherlands and Germany. The reservoir, composed of porous and permeable sandstone, undergoes a process involving cold water injection and hot water extraction. A fault, situated 750 meters from the injector is investigated as to whether it is reactivated.

Chapter 5: This chapter gives the conclusions of the overall results presented in the thesis and presents future perspectives.

Chapter 2

Experimental and numerical analysis of injection-induced permeability changes in pre-existing fractures[a]

Abstract

This chapter presents a combined laboratory and numerical investigation on the injection-induced permeability changes in pre-existing fractures. The analyses conducted were primarily based on the results of an innovative laboratory experiment designed to replicate the key mechanisms that occur during hydraulic stimulation of naturally fractured rocks and/or faulted zones. The experiment involved pressure-controlled fluid injection into a laboratory-scale pre-existing fracture within a granite block, which was subjected to true triaxial stress conditions. Rough and smooth fractures are investigated, and the results are discussed. Based on the experimental results, two contributing mechanisms were considered to describe the pressure-driven permeability changes in pre-existing fractures: 1) elastic opening/closure leading to a reversible permeability change, and 2) fracture sliding in shear mode, causing dilation and hence an irreversible permeability increase. With these assumptions, an aperture-dependent permeability function was adopted to couple the hydraulic flow with the mechanical deformations along the fracture. Subsequently, a 3D coupled hydro-mechanical model was developed to

[a]This chapter has been published in Geomechanics for Energy and the Environment [Ouf et al., 2024b].

replicate fluid-injection tests conducted at various conditions, including different stress conditions and fracture surface roughness. The employed modeling framework effectively captured the experimental observations. The results indicate that the maximum permeability increases twofold.

2.1 Introduction

2.1.1 Background

The utilization of geothermal energy for electricity generation is considered to be technically and economically viable at temperatures above 120 °C [Saar, 2017]. To reach such temperatures, in most locations deep wells must be drilled to depths of 3 to 5 km [Lu, 2018], depending on the local geothermal gradient and the presence of permeable zones at the targeted site, which are usually found in the form of naturally fractured rocks and/or faulted zones. Therefore, fractured zones play an important role in deep geothermal systems as they are the main conduits for fluid flow and heat transfer. However, unlike shallow hydrothermal systems in porous formations, deep geothermal resources are typically characterized by hot-dry conditions and exhibit low permeability values (less than 10^{-16} m^2 [Saar and Manga, 2004, Achtziger-Zupančič et al., 2017]), which present challenges for water circulation and heat extraction from these resources. An engineering solution to artificially enhance the permeability in deep formations is the so-called hydraulic stimulation technique, which involves injecting high-pressure fluid, usually water or brine, into a low-permeability rock mass in order to reactivate pre-existing fractures in shear mode (HS: hydro-shearing) or potentially creating new fractures in tensile mode (HF: hydro-fracturing) [Gischig et al., 2020]. However, high-pressure fluid injection into a geothermal reservoir inevitably induces micro-seismic events around the injection zone, primarily due to the reactivation of critically stressed fractures in shear mode.

From an engineering perspective, two competing, but inter-connected, objectives

should be targeted in any hydraulic stimulation practice, i.e. 1) significantly increasing the permeability of the reservoir to an economically viable level, and 2) simultaneously controlling the induced seismicity below a hazardous level [Amann et al., 2018]. HS has been successfully implemented in numerous Enhanced Geothermal Systems (EGS), often resulting in a permeability increase of up to 2-3 orders of magnitude. Notable examples include Soultz-sous-Forets in France [Evans et al., 2005, Gérard et al., 2006], Cooper Basin in Australia [Bendall et al., 2014], Fenton Hill in New Mexico, USA [Kelkar et al., 2016, Brown, 1995]. Although a significant portion of seismic events that occur during hydraulic stimulation are below the sensitivity level, it is possible that reservoir stimulation may result in induced seismicity above a hazardous threshold. Such seismic events have been unfortunately experienced in the past in a limited number of EGS projects, as demonstrated by incidents in Pohang in Korea [Kim et al., 2018], Basel in Switzerland [Häring et al., 2008] and Vendenheim near Strasbourg in France [Schmittbuhl et al., 2021] which raised public concerns. Nonetheless, the sustainability of permeability enhancement over time may be uncertain. For example, in the hydraulic stimulation test conducted as part of the St1 Deep Heat Project in southern Finland, permeability initially increased by two orders of magnitude but gradually returned to its natural value after pressure recovery [Kukkonen et al., 2023]. These examples highlight the complexity of hydraulic stimulation outcomes and the factors influencing the permeability enhancement.

2.1.2 State-of-the-art in hydraulic stimulation

To effectively increase the permeability of a geothermal reservoir through hydraulic stimulation while mitigating the induced seismicity, it is important to have a comprehensive understanding of various influencing factors [Kivi et al., 2023], including the site characteristics (in-situ stress state, pore pressure, temperature), fault/fracture properties (type, dip, dip direction, frictional strength, permeability, etc), host rock properties (stiffness, UCS, tensile strength, permeability, heat conductivity, etc) and

the injection data (the injection type, duration, location, etc). Numerous field investigations have been conducted over the past decades to explore the underlying processes that occur during reservoir stimulation at different spatial and temporal scales (e.g. see [McClure and Horne, 2014] for a comprehensive review). Among them, the hydraulic stimulation experiments on fractured granite at Grimsel Test Site (GTS) [Gischig et al., 2020, Amann et al., 2018] and the fault-reactivation experiment in clay shale at Mont-Terri Underground Rock Laboratory (MT-URL) [Guglielmi et al., 2017, 2021, Jeanne et al., 2018] are worth mentioning. These field experiments have provided valuable insights into the risks, limitations, and technical challenges associated with hydraulic stimulation in real-size geothermal systems.

The roughness of fractures significantly affects their hydromechanical behavior. Barton [1973] demonstrated that fractures with varying Joint Roughness Coefficients (JRCs) exhibit differences tangential stiffness, normal stiffness, friction angle, cohesion and dilation angle when subjected to different shear and normal loads. Tsang and Witherspoon [1981] findings indicate that under normal loading, fracture roughness impacts the initial aperture and the variation of normal aperture, consequently affecting the flow rate, which tends to be higher in rough fractures. Moreover, differences in fracture roughness give rise to varying contact areas. Consequently, the stress exerted in the contact region exceeds predictions solely based on dividing the total load by the total fracture area. The presence of shear stress can induce damage to the fracture surface, altering the asperity geometry through processes such as abrasion, smoothing, or roughness enhancement. The extent of these changes depends on the initial fracture roughness and the applied load [Gentier et al., 2000, Sausse, 2002].

In addition to field investigations, numerous laboratory-scale experiments have been designed over the past decades with the aim of down-scaling the fluid injection process in geothermal reservoirs (see e.g. [Zoback et al., 1977, Deb et al., 2020, Zhang et al., 2020, Wang et al., 2024]). These small-scale laboratory experiments provide the means to constrain various field-related parameters that can naturally be subjected to uncertainties. This allows for the investigation of fundamental hydro-mechanical

processes occurring during both reservoir stimulation and geothermal operation under pre-defined/controlled conditions. An essential aspect in this context which has been investigated experimentally, is the changes in fracture permeability resulting from fluid injection. Numerous experimental studies have indicated that fracture permeability tends to increase as the effective normal stress applied to the fracture decreases as a result of increases in fluid pressure (e.g. see [Ye and Ghassemi, 2018, Ishibashi et al., 2018, Li et al., 2023]). Dilation triggered by shearing has been identified as the primary mechanism responsible for the irreversible increase in hydraulic aperture, and consequently a sustainable enhancement in the fracture permeability [Almakari et al., 2020].

Another crucial aspect in the context of geothermal reservoir engineering, which has been the subject of intensive research in recent years, is the development of reliable numerical models capable of reproducing the coupled hydro-mechanical processes in deep geothermal systems. In general, the numerical approaches introduced to describe the coupled multi-physics processes in geothermal reservoirs can be categorized into two groups [Pandey et al., 2018]: 1) continuum-based models and 2) discontinuum models. In continuum-based models, the fractured zones and faults are considered as a porous media with equivalent thermo-hydro-mechanical properties. This modeling approach has been widely employed in geothermal reservoir modeling to describe injection-induced fault reactivation [Jeanne et al., 2018, Park et al., 2020, Cappa et al., 2022], induced seismicity [Rutqvist et al., 2013, 2015], as well as the temporal and spatial development of temperature and fluid pressure [Rutqvist et al., 2002, Yuan et al., 2020]. In contrast, discontinuum models rely on the explicit representation of fractures in the rock matrix. The most common discontinuum modeling techniques include 1) FEM-DEM/cohesive zone modeling [Lisjak et al., 2014, Grasselli et al., 2015], 2) Discrete Fracture Network using interface element [Gischig and Preisig, 2015], 3) embedded lower dimensional element [Watanabe et al., 2012]. While continuum-based models offer a simplified representation of fractured zones and faults by treating them as porous media, discontinuum models take a more explicit approach by directly representing

fractures within the rock matrix. Both modeling strategies have their strengths and limitations, and the choice between them depends on the specific geothermal reservoir characteristics and the phenomena under investigation.

2.1.3 Objectives

There is a scarcity in the literature regarding numerical modeling and experimental set-up that accurately replicates smaller-scale HS, where experimental conditions are well-characterised and experimental results are closely monitored [Amann et al., 2018, Rinaldi and Rutqvist, 2019]. Most laboratory experiments conducted so far have been conducted in triaxial apparatuses, leading to limitations in representing realistic stress conditions. Additionally, the predominant use of cylindrical samples with restricted dimensions has resulted in boundary conditions close to the injection point and limited representativeness of fracture surfaces. To address these limitations, our study introduces a novel approach. I employ results from a unique true triaxial machine coupled with injection into an artificial fault at a decimeter scale. This setup offers a controlled environment for exploring the hydromechanical behavior of pre-existing fractures. The true triaxial machine allows for precise stress control, ensuring that experimental conditions can better replicate real-world scenarios. Secondly, injecting fluids into an artificial fault at a decimeter scale provides a fracture surface that is more representative than cylindrical samples, which are often limited in length.

In contrast to previous methods where fracture behavior modeling, such as with TOUGH-FLAC, utilized a staggered coupling approach resulting in a partially coupled solution, the numerical approach employed here within the MOOSE framework is fully coupled.

The focus in this study lies on the mechanisms that lead to permeability enhancement in pre-existing fractures as a result of pressurized fluid injection. During reservoir stimulation, fluid injection increases fluid pressure and reduces the effective normal stress on pre-existing fractures. This may trigger sliding along critically stressed frac-

tures, resulting in irreversible fracture opening (dilation) and, consequently, an increase in their permeability. Carefully down-scaled laboratory and modeling analyses can be useful to illuminate the relationship between permeability and mechanical characteristics in pre-existing fractures, as illustrated in Fig. 2.1. With this motivation, this study aimed to achieve the following objectives:

- To develop and validate a suitable modeling framework to describe the hydro-mechanical processes resulting from high-pressure fluid injection in pre-existing fractures. The developed model provides a numerical description for the injection-induced permeability changes. The numerical modeling used is fully coupled and solved without staggering.

Staggering in the Finite Element Method (FEM) and Finite Volume Method (FVM) involves distributing variables across computational grids to improve stability, accuracy, and convergence, especially in coupled problems like fluid-structure interaction. In FEM, different variables (e.g., displacement, velocity, pressure) are assigned to different mesh points, helping prevent numerical oscillations and improving coupling, though it adds complexity [Permann et al., 2020]. In FVM, velocity components are defined at the cell faces and pressure at the cell centers, which prevents issues with pressure-velocity coupling and ensures mass conservation in fluid dynamics simulations. While both methods enhance stability and reduce oscillations, staggering increases computational complexity and may introduce grid dependency, making it crucial for accurately simulating coupled systems [Permann et al., 2020].

2.2 Methodology

2.2.1 Methodology for the laboratory experiments

A series of fluid-injection tests into pre-existing fractures were conducted at room temperature (20 °C) using a True Triaxial Rock Testing Machine. The testing apparatus

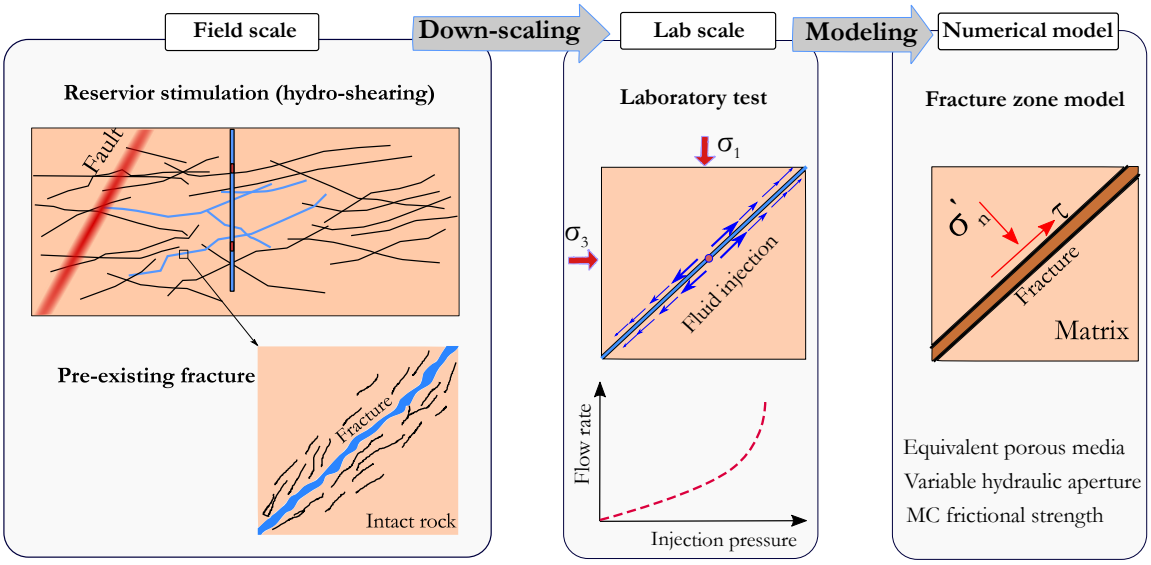


Figure 2.1: Figure showing the overall objectives of this study including 1) design and perform laboratory experiments that scale down the hydraulic shearing process, 2) develop numerical models capable of reproducing the injection-induced permeability change in pre-existing fractures

was originally developed to investigate fracture initiation and propagation in intact rock during hydraulic fracturing experiments [Siebert, 2020] and these data were used to calibrate and validate numerical modeling [Deb et al., 2020, 2021]. The setup and sample configuration were modified for the purpose of the experiments presented in this study.

Sample preparation and experimental apparatus

The rock used in the experiments was an isotropic, fine-grained and low-permeability granite (Tittinger Feinkorn) cored from the Höhenberg quarry in Bavaria, Germany. It was composed of 45% quartz, 25% potassium feldspar, 20% plagioclase, and 7.5% biotite [Clauser et al., 2015]. The samples were cuboid-shaped, saw cut, and polished to a size of 300 mm × 300 mm × 450 mm with a precision of ± 0.05 mm and parallelity of ± 0.001 mm. A discontinuty/fracture (laboratory-scale fault) was then created by saw cutting the cuboid into two prisms along the diagonal of the sample (Fig. 2.2). The

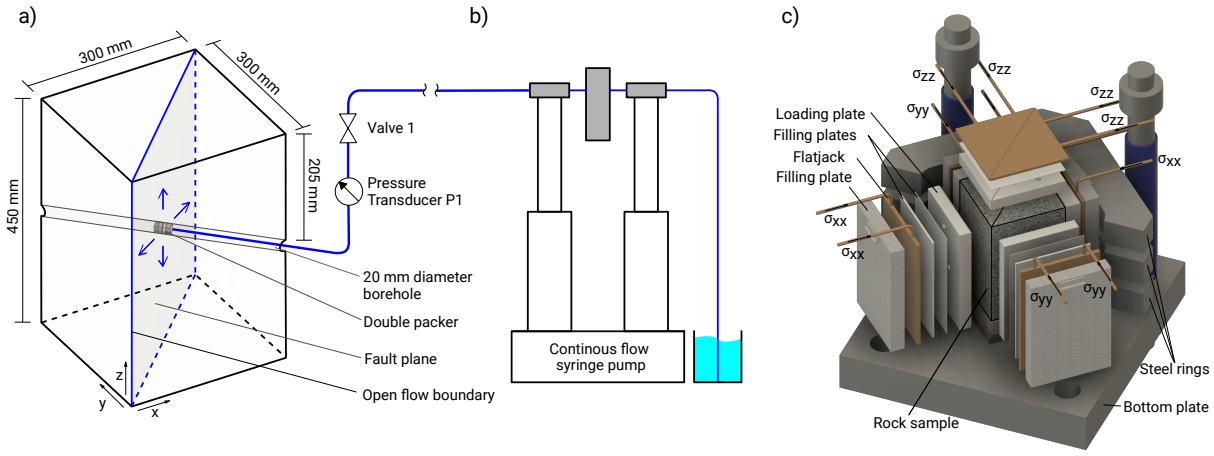


Figure 2.2: A schematic representation of triaxial testing setup for hydro-shearing; a) a granite block with a vertical fault plane is shown. The fluid is injected through a borehole with a diameter of 20 mm. Water can flow out at the fault boundaries. The injection interval is isolated by a double packer system; b) the injection unit consisting of a flow pump and a pressure transducer; c) the true triaxial loading apparatus

resulting surfaces were further ground and polished. Two roughness values were chosen for the fracture plane in the tests: 1) a smooth fracture surface polished with 1200 grit silicon carbide (SiC) powder and 2) the rough surface fracture polished with 40 grit SiC powder. The samples also contained a borehole with a diameter of 20 mm, crossing the fracture plane perpendicularly (Fig. 2.2). A double packer system was employed to establish a 2 mm-long isolated interval along the borehole, containing the fracture. During the experiments, the deionized water was injected at room temperature by a dual-pump setup of two ISCO 500D syringe pumps allowing continuous flow of up to 200 ml/min. The fluid was transferred by a steel capillary with a diameter of 2 mm into the isolated interval. The two packers were not connected allowing free kinematic movement along the isolated interval. The injection pressure was measured by a Keller 300x pressure transducer outside the sample and flow was controlled by a valve between the packer and the pump (Fig. 2.2).

The granite block was confined by three sets of oil-filled flatjacks, which were independently controlled by a system of three Automatic Pressure Controller syringe

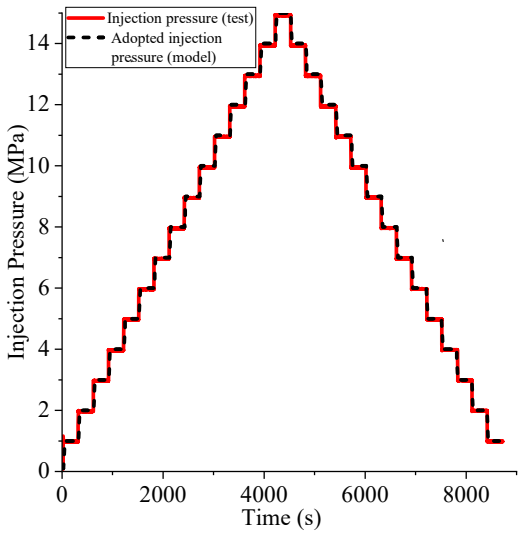
pumps (Wille VPC). The horizontal stresses were both applied by two opposing, rectangular flat jacks (σ_{xx} and σ_{yy} in Fig. 2.2). The vertical stress (σ_{zz}) was induced by two sets of opposing, triangular flatjacks. The stresses were transferred to the granite block by steel load plates, covered with teflon foil to reduce friction between metal and rock. The loading unit was held in place by several filling plates and three steel rings at the side and two steel plates at the top and bottom. The fracture was drained to all sides. All corners of the rock blocks were open to the atmosphere and bevelled edges of the fracture allowed discharge to the top and bottom between the sample and load plates.

Testing procedures and injection protocols

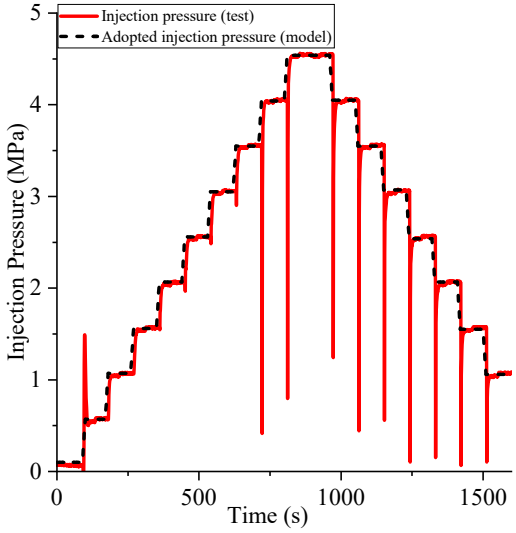
The following hydraulic tests were conducted considering different settings in terms of the applied stress conditions and fracture surface roughness:

- Test 1 (isotropic loading/smooth fracture): in the first test, a granite block with a smooth fracture plane was isotropically loaded at the constant stress of $\sigma_{xx} = \sigma_{yy} = \sigma_{zz}$= 10 MPa. The initial normal stress applied on the fracture plane was then σ_n = 10 MPa. The fluid injection process involved step-wise increasing the water pressure in the isolated interval by 1 MPa every 300 seconds until it reached almost 15 MPa. Subsequently, the pressure recovery was performed by gradually decreasing the pressure by 1 MPa every 300 seconds until it returned to 1 MPa (Fig. 2.3a).

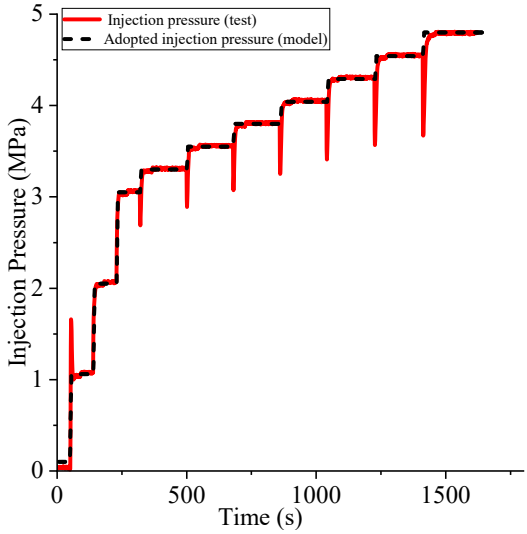
- Test 2 (isotropic loading/rough fracture): in the second test, the injection test was performed on a sample with a rough fracture plane. The sample was isotropically confined at the stress of $\sigma_{xx} = \sigma_{yy} = \sigma_{zz}$= 3 MPa. Accordingly, the initial normal stress applied on the fracture plane was σ_n = 3 MPa. The water injection process consisted of step-wise increment of water pressure by 0.5 MPa every 80 seconds until it reaches 4.5 MPa, followed by a gradual decrease of 0.5 MPa every 80



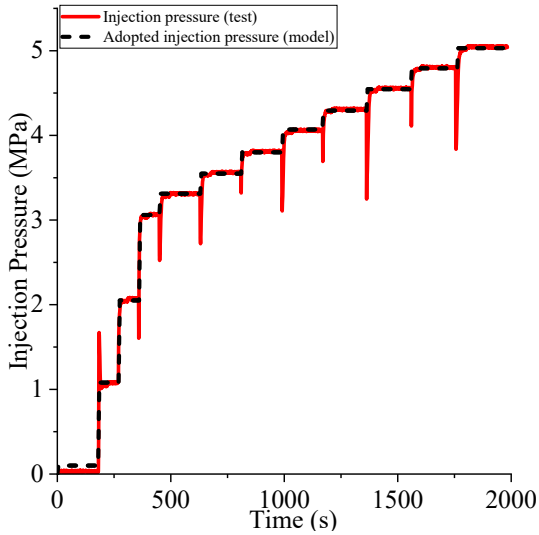
(a) $\sigma_n = 10$ MPa and $\tau = 0.0$ MPa



(b) $\sigma_n = 3$ MPa and $\tau = 0.0$ MPa



(c) $\sigma_n = 3$ MPa and $\tau = 1.0$ MPa



(d) $\sigma_n = 3$ MPa and $\tau = 1.0$ MPa

Figure 2.3: Injection protocols for the conducted hydraulic stimulation tests along with the adopted injection pressure in the numerical simulations; a) Test 1, isotropic loading/smooth fracture; b) Test 2, isotropic loading/rough fracture; c) Test 3, shear loading/rough fracture; d) Test 4, shear loading/rough fracture

seconds until it returns to almost 1 MPa (Fig. 2.3b).

- Tests 3 and 4 (shear loading/rough fracture): two tests were performed on a sample with a rough fracture plane subjected to a pre-defined shear stress. The applied stresses to the granite block in these tests were $\sigma_{xx} = 4$ MPa, $\sigma_{yy} = 2$ MPa, and $\sigma_{zz} = 3$ MPa, theoretically resulting in a mean stress of $\sigma_n = (\sigma_{max} + \sigma_{min})/2 = 3$ MPa, and the shear stress of $\tau = (\sigma_{max} - \sigma_{min})/2 = 1$ MPa. The injection process involves gradually increasing the water pressure until it reaches almost 5 MPa (Figs. 2.3c and 2.3d). When further increasing the injection pressure, the flow rate rose sharply until it reached the upper limit of the injection pump, which was then shut off. Accompanied by a distinct stress drop, this prevented the accomplishment of a step-down phase as seen in tests 1 and 2.

All tests were planned with a normal stress of 10 MPa, but when the rough sample was tested, the fracture was too permeable to reach injection pressures in the range of 10 MPa within the capacity of the injection pump.

2.2.2 Methodology for the coupled HM-modeling

An Equivalent Continuum Modeling (ECM) approach was employed to describe the hydro-mechanical processes in pre-existing fractures. To accomplish this, the fracture was modeled as a finite-thickness porous medium with equivalent hydro-mechanical properties. The intact rock was considered as a low-permeable material. An aperture-dependent permeability function was adopted to describe the permeability changes of the fracture zone. The fracture permeability model was implemented by the authors in the multi-physics finite element code MOOSE framework [Permann et al., 2020]. I also employed the PorousFlow and TensorMechanics module to solve the coupled hydro-mechanical equations [Wilkins et al., 2020]. The coupled equations to be solved in both the fracture zone and the intact rock include: 1) the momentum balance equation, and

2) the mass balance of the liquid phase. The following subsections provide more details on the theoretical and modeling assumptions employed in this study.

Mechanical formulations

The following equation holds across the entire domain (intact rock and fracture) to satisfy the balance of linear momentum (the gravitational forces and inertia effects are neglected):

$$\nabla . \boldsymbol{\sigma} = 0. \tag{2.1}$$

The total stress $\boldsymbol{\sigma}$ in the above equation is related to the effective stress $\boldsymbol{\sigma}^{'}$ and the pore pressure p_f through the Biot's effective stress concept (i.e. $\boldsymbol{\sigma} = \boldsymbol{\sigma}^{'} + \alpha_b p_f \boldsymbol{I}$; α_b: Biot coefficient). The changes in the effective stress value $\boldsymbol{\sigma}^{'}$ in both the intact rock and the fracture domain are governed by the selected mechanical constitutive models. In this study, the intact granite was modeled as an isotropic linear elastic material (i.e. Hooke's law defined through two elastic parameters Young's modulus E and Poisson's ratio ν). Additionally, a slip-weakening Mohr-Coulomb plastic model was used to describe the frictional strength, shear-induced dilation and irreversible deformation in the fracture zone. The Mohr-Coulomb yield criterion (onset of plastic shear deformation) is generally defined as follows:

$$\tau = \tan\phi \ \sigma_n^{'} + c \tag{2.2}$$

where, τ is the shear stress and $\sigma_n^{'}$ is the effective normal stress on the fracture plane. The parameters ϕ and c are the friction angle and the cohesion, respectively. It was assumed that, upon reaching the failure criterion in Eq. 2.2, the friction angle decreases from its initial static value ϕ_0 to a residual value ϕ_r due to shear sliding. The following exponential function was used to describe the slip-weakening behavior:

$$\phi = \phi_r + (\phi_0 - \phi_r) \exp\left(-R \ \varepsilon_{ps}\right) \tag{2.3}$$

where ε_{ps} is the plastic shear strain and R is a parameter that controls the rate of friction weakening (Fig. 2.4a). I acknowledge that this method is mesh-dependent, regularisation methods could be used to tackle this effect.

Shear failure induced dilation is represented by the dilation angle, ψ, which controls the magnitude of the volumetric strain during plastic deformation. The Mohr-Coulomb plastic strain is generally defined as follows:

$$\varepsilon^p = \lambda \frac{\partial g_p}{\partial \sigma} \tag{2.4}$$

where, ε^p is the plastic strain, λ is the lagrange multiplier and g_p the plastic flow potential. The plastic flow potential in Mohr-Coulomb is generally defined as:

$$g_p = \tan\psi \ \sigma_n^{'} + c \tag{2.5}$$

Where ψ is the dilation angle. It was assumed that the friction angle is superior to the dilation angle, therefore the flow rule is non-associated.

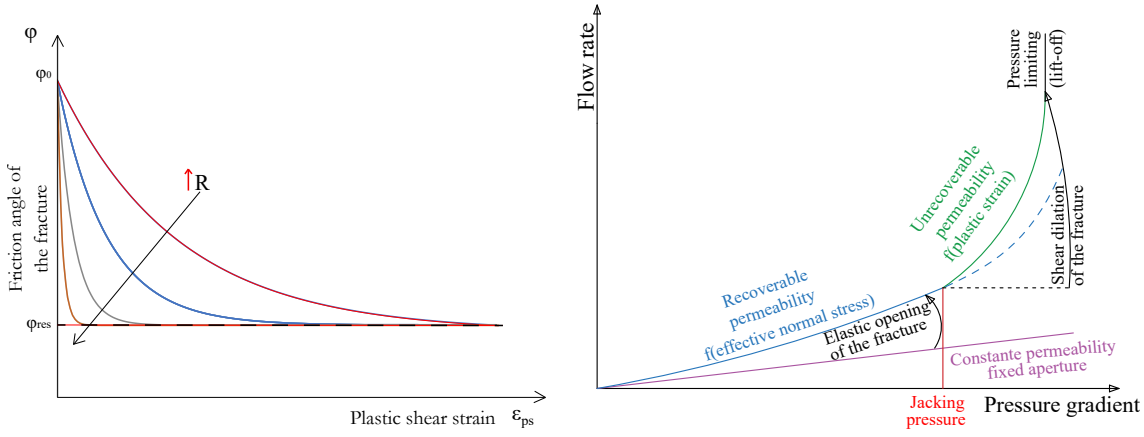
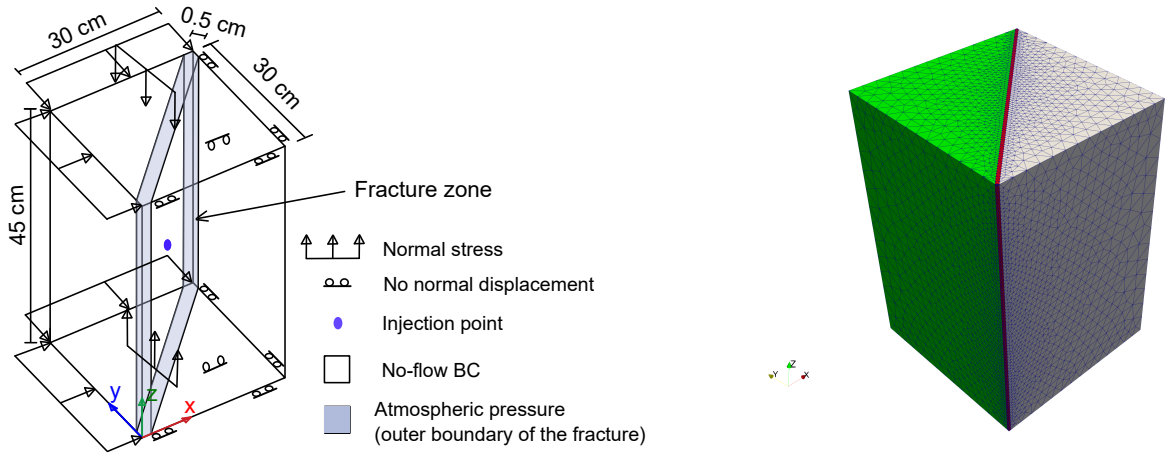


Figure 2.4: a) Slip-weakening Mohr-Coulomb model to describe the frictional strength of the fracture zone; b) Schematic representation of the non-linear flow rate in a fracture as a result of fuild injection, modified after Krietsch et al. [2020]



(a) (b)

Figure 2.5: a) Hydro-mechanical boundary conditions for the numerical modeling of the fluid injection tests; b) the finite element mesh of the granite block and fracture zone

Hydraulic formulations

The equation for the mass balance of liquids in a porous medium is generally defined as:

$$\frac{\partial(n\ \rho_f)}{\partial t} + (n\ \rho_f)\frac{\partial \varepsilon_{vol}}{\partial t} = -\boldsymbol{\nabla} \cdot \boldsymbol{q}_f + q^*, \tag{2.6}$$

where q^* is the source term (injection), n the porosity, ρ_f fluid density. The term ε_{vol} is the volumetric strain, which is a coupling term showing the effect of mechanical deformation on the water pressure. Assuming a constant bulk modulus for water (K_f = 2.0 GPa), the following equation was used to describe the changes in water density ρ_f as a function of the pore water pressure p_f:

$$\frac{\partial \rho_f}{\partial t} = \frac{\rho_f}{K_f}\frac{\partial p_f}{\partial t} \tag{2.7}$$

The generalized Darcy's law was used to describe the flow velocity of water $\boldsymbol{q}_f$ (unit: m/s) in Eq. 2.6 (neglecting gravitational pressure gradient):

$$\boldsymbol{q}_f = -\rho_f \frac{\boldsymbol{k}}{\mu_f} \,.\, (\boldsymbol{\nabla} p_f) \tag{2.8}$$

In the above equation, p_f is the pore pressure (compression positive) and μ_f is the dynamic viscosity of water. The quantity $\boldsymbol{k}$ is the intrinsic permeability tensor of the medium. In this study, the intact granite was modeled as a low-permeable material with a constant permeability. On the other hand, a permeability function dependent on the hydraulic aperture was taken into account for the fracture zone to replicate the highly non-linear flow rates typically observed during hydro-shearing field experiments (Fig. 2.4b). The cubic-law model developed by Tsang and Witherspoon [1981] was used to formulate the permeability of the fracture zone k_{fracture}, assuming a laminar flow within parallel planar fracture surfaces, i.e.

$$k_{\text{fracture}} = \frac{b_h^3}{12} s_f \tag{2.9}$$

In this equation, b_h is the hydraulic aperture and s_f fracture spacing. The fracture spacing parameter might be useful to estimate the equivalent permeability of a fractured rock medium consisting of a set of persistent fractures with the same spacing and the same apertures [Min et al., 2004]. It should be also noted that the substitution of Eq. 2.9 in Eq. 2.8 yields directly the volumetric flow rate across the fracture (unit: m^3/s). It is well-known that the hydraulic aperture in a fracture may change as a result of mechanical factors such as stress and deformation [Lee and Cho, 2002]. Therefore, it was assumed that the hydraulic aperture b_h consists of three parts (as illustrated in Fig.2.4b), i.e. 1) a constant term b_{ini}, 2) a reversible part b_{el} and 3) an irreversible part b_{shear}:

$$b_h = b_{ini} + b_{el} + b_{shear} \tag{2.10}$$

The reversible part of the aperture function was described through the model proposed

by Rutqvist et al. [2002], Rutqvist and Tsang [2003]. According to this model, the reversible hydraulic aperture b_{el} is an exponential function of the effective normal stress $\sigma_n^{'}$ applied to the fracture plane:

$$b_{el} = b_{el}^{max} \exp(\alpha \sigma_n^{'}) \tag{2.11}$$

where, b_{el}^{max}, and α are the model parameters, controlling the magnitude and the rate of aperture change as a function of the normal effective stress. The last term in Eq. 2.10 refers to the changes in hydraulic aperture due to shear slip along the fracture (hydro-shearing). The model proposed by Rinaldi and Rutqvist [2019] was adopted to describe the fracture shear dilation and the resulting changes in hydraulic aperture. Accordingly, the irreversible part of the hydraulic aperture b_{shear} was defined through the equivalent plastic shear strain ε_{ps} and the dilation angle ψ:

$$b_{shear} = \max\left(\frac{\varepsilon_{ps}\ tan(\psi)}{s_f},\ b_{shear}^{max}\right) \tag{2.12}$$

The magnitude of equivalent plastic shear strain ε_{ps} depends on the Mohr-Coloumb friction angle defined for the fracture zone, while the irreversible fracture opening is controlled by the dilation angle ψ. It should be noted that the irreversible aperture opening b_{shear} was limited to a cut-off parameter b_{shear}^{max}. This parameter defines the maximum irreversible opening that can be achieved as a result of shear sliding.

3D FE modeling of the experiments

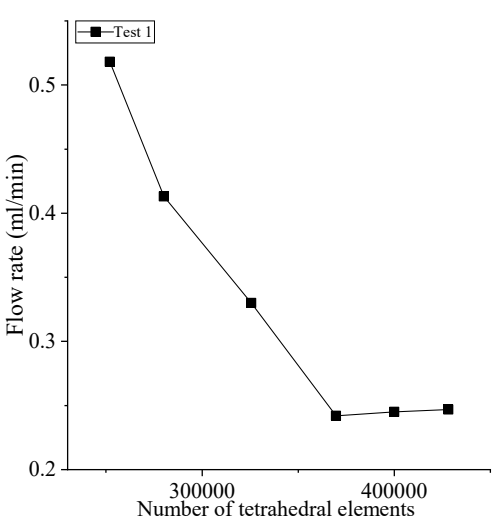
Fig 2.5 presents the geometry of the model and its finite element mesh created in the MOOSE framework. I utilized the Galerkin Finite Element Method (FEM) employing Lagrange shape functions of first order. For numerical approximation of integrals over the reference element, I employed quadrature techniques, typically utilizing Gaussian Quadrature. Utilizing the MOOSE framework, I have utilised the B-bar approach to mitigate volumetric locking [Giudicelli et al., 2024]. To address concerns regarding shear locking, I maintained element aspect ratios close to 1 during our investigations. Fur-

thermore, I exercised caution in selecting fracture thickness and final mesh count to prevent the occurrence of very thin elements, which could potentially introduce undesirable numerical artifacts caused by shear-locking.

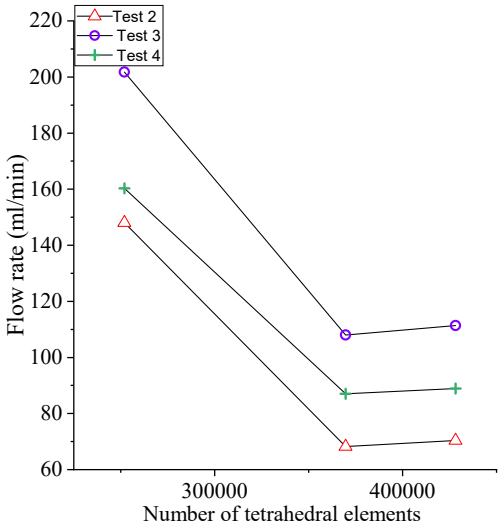
The fracture zone was modeled using thin 3D continuum elements with an equivalent thickness of 5 mm. I have refined the center of the model at the injection point, specifically focusing on the fracture. At its center, the width of the fracture is represented by 4 elements. Fig. 3.5 demonstrates the sensitivity of the model to changes in mesh density. As the number of elements increases, particularly in the vicinity of the injection point, the model's accuracy improves. Figs. 2.6*a* and 2.6*b* illustrate how the maximum flow rate converges with increasing mesh density and Fig 2.6*c* illustrate how the equivalent plastic strain converges with increasing in mesh density. The modeling results remained unchanged as the number of elements exceeded ca. 370 000 tetrahedral elements. The final model used for the simulation of the experiments had of ca. 430 000 tetrahedral elements and ca. 72 000 nodes. With a relatively stable flow rate, dependent on permeability and plastic properties, the model appears appropriately meshed.

Before model calibration, a series of preliminary simulations were carried out to determine a suitable thickness for the fracture zone. Two criteria were taken into account to use a reasonable thickness for the fracture zone: 1) ensuring that the fracture zone is not excessively thick to be representative of the problem scale 2) preventing potential numerical problems (e.g., insufficient elements across the thickness, possibly shear-locking due to inappropriate aspect ratio of elemets) associated with an extra thin fracture zone. Moreover, the phenomenon of strain localization results in uneven fluid pressure distributions, significantly influencing the apparent frictional characteristics of the fracture zone and its permeability [Rattez et al., 2018b,a, Platt et al., 2014, Stathas and Stefanou, 2023].

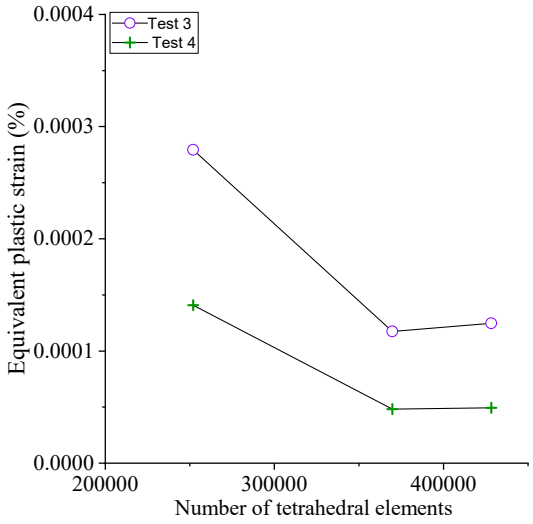
The fluid flow was set to zero on the outer boundaries of the granite bulk to define the hydraulic boundary conditions. A constant pressure of 0.1 MPa was applied to the outer boundaries of the fracture zone, considering its connection to the atmo-



(a) Smooth fracture



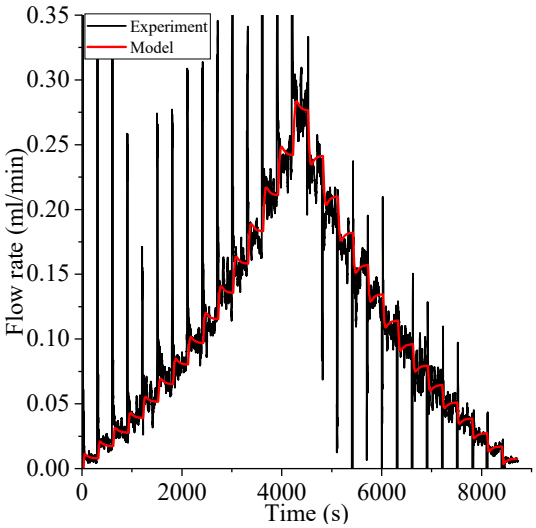
(b) Rough fractures



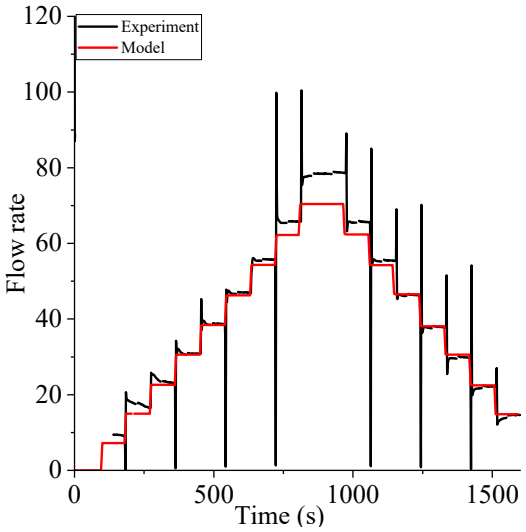
(c) Rough fractures

Figure 2.6: Mesh convergence; a) Test 1, smooth fracture flow rate; b) Test 2, 3, 4, rough fracture flow rate; c) Test 3, 4, rough fracture equivalent plastic strain

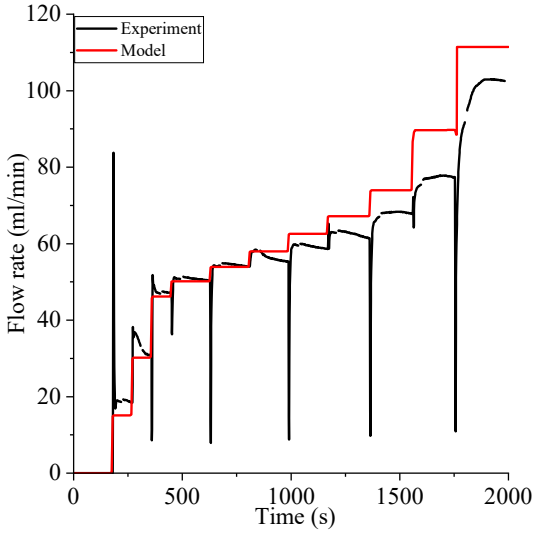
sphere. Both the rock and fracture zone were assumed to be fully saturated before and during the experiments. An initial pore pressure of 0.1 MPa was assumed in the entire model. The fracture zone homogenization was idealized as an equivalent porous medium. To compute the equivalent permeability for a single joint, I assumed high porosity, which allows the permeability to be represented as a continuum. This assumption ensures that the equivalent permeability reflects the hydraulic properties of the joint, accounting for the increased flow capacity due to the high porosity. Rutqvist et al. [2020] conducted a comparative study on fracture stimulation techniques, evaluating both continuum and discontinuum methods. The injection process was modeled as a singular point injection. Fig. 2.3 also shows the injection pressures applied in the numerical models. The mechanical boundary conditions were defined by constraining one half-block in all directions, while the other half was subjected to constant external loads corresponding to the values implemented in the tests. This approach was used to ensure that deformations can be induced within the fracture zone by the injection process (both opening and sliding). The goal was to analyze the direct impact of injection, without the interference of additional mechanical influences. The end friction effect resulting from the contrast of elastic properties between steel load plates and the rock samples was not incorporated in the model. The hydro-mechanical properties of intact granite (see Table 2.1), such as elastic parameters, porosity, and permeability, were primarily derived from previous studies on comparable rocks (e.g. [Siebert et al., 2017, Selvadurai et al., 2019]). The model parameters associated with the fracture zone, including both the slip-weakening Mohr-Coulomb model and the aperture-dependent permeability function, were determined through back-calculation by calibrating the model against the conducted laboratory experiments (Table 2.2).



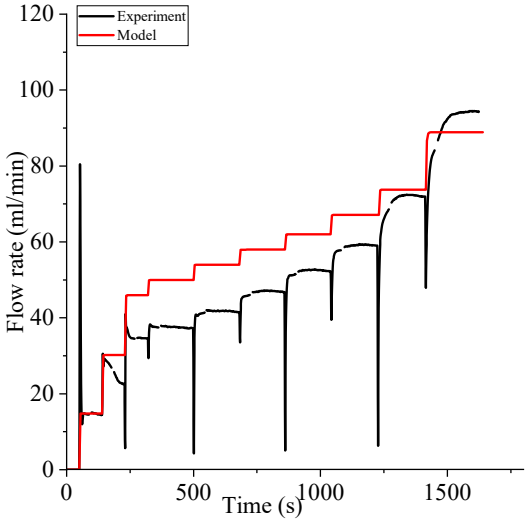
(a) Test 1: $\sigma_n = 10$ MPa and $\tau = 0.0$ MPa



(b) Test 2: $\sigma_n = 3$ MPa and $\tau = 0.0$ MPa



(c) Test 3: $\sigma_n = 3$ MPa and $\tau = 1.0$ MPa



(d) Test 4:$\sigma_n = 3$ MPa and $\tau = 1.0$ MPa

Figure 2.7: Flow rate evolution obtained during hydraulic stimulation tests along with the numerical modeling results; a) Test 1, isotropic loading/smooth fracture; b) Test 2, isotropic loading/rough fracture; c) Test 3, shear loading/rough fracture; d) Test 4, shear loading/rough fracture

Table 2.1: Hydro-mechanical parameters used in the numerical models

Parameters	Unit	Granite	Fracture zone
Mechanical model			
Young modulus (E)	GPa	37	37
Poisson's ratio (ν)	-	0.3	0.3
Cohesion (c)	MPa	-	0.0
Static friction angle (ϕ_0)	°	-	37
Residual friction angle (ϕ_r)	°	-	20
Dilation angle (ψ)	°	-	15
Softening rate (R)	-	-	3000
Hydraulic model			
Biot coefficient (α_b)	-	1	1
Fluid density (ρ_f)	kg/m^3	1000	1000
Fluid viscosity (μ_f)	MPa*s	10^{-9}	10^{-9}
Fluid bulk modulus (K_f)	GPa	2	2
Rock density (ρ_r)	kg/m^3	2640	2640
Porosity (n)	%	1.5	95
Permeability tensor (k)	m^2	10^{-22}	Table 2.2

Table 2.2: Input model parameters for the fracture permeability function

Parameters	Unit	Test 1 (smooth)	Test 2 (rough)	Test 3 (rough)	Test 4 (rough)
b_{el}^{max}	μm	16.5	115	115	115
b_{ini}	μm	0.85	10	10	10
α	MPa^{-1}	0.06	0.005	0.005	0.005
b_{shear}^{max}	μm	-	-	28	28
s_f	m^{-1}	1	1	1	1

2.3 Results and discussion

2.3.1 Injection flow rate versus time

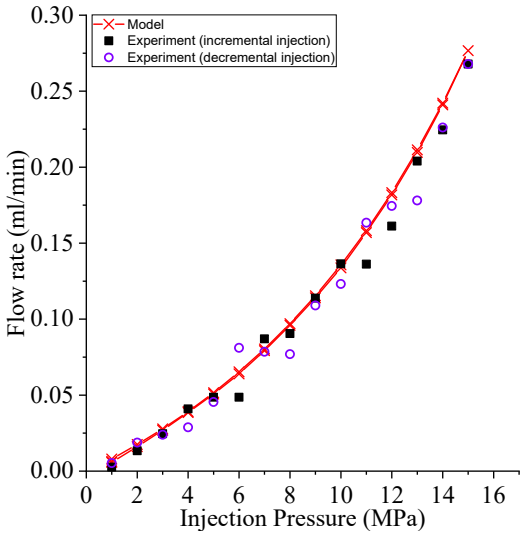
Fig. 2.7 shows the injection flow rate (unit: ml/min) obtained within the experiments. In the first test, isotropic loading/smooth frature, the injected flow rate gradually increased to approximately 0.27 ml/min as the injection pressure reached step-wise to a maximum of 15 MPa (Fig. 2.7a). The monitored flow rate showed a sudden increase at the beginning of each pressure interval followed by a rapid decrease to a steady-state

value. The large fluctuations observed in the flow rate were probably due to low injectivity which made the pump regulation difficult. During the pressure recovery stage, as the pressure reduced to zero, the obtained flow rates were nearly identical to those observed during the injection stage for the same injection pressure. This observation indicates a reversible opening/closure mechanism in the fracture. The maximum flow rate achieved at the injection pressure of 15 MPa was very small (about 0.27 ml/min), indicating a minimal hydraulic aperture of the fracture due to the small asperities at the fracture plane and the high isotropic confining stress applied to the sample. The impact of these two factors, i.e. applied confining stress and fracture roughness, on the hydraulic flow paths was highlighted in the results of the second test (Fig. 2.7b). In this test, the larger asperities on the rough fracture plane created a more substantial flow path along the fracture. The injection flow rate monitored during the test reached 80 ml/min when the injection pressure was almost 4.5 MPa (i.e., almost 2 orders of magnitude larger than in the first test). The flow rate values in their steady-state condition exhibited a consistent increase of around 8 ml/min per constant pressure increment of 0.5 MPa. This observation suggests that while there may not have been a significant absolute aperture change compared to Test 1, while there may not have been a significant absolute aperture change compared to Test 1, the relative permeability gain was not substantial due to the already high initial permeability. In the last two tests, the impact of injection-induced shear slip on the flow rate evolution was investigated, where the fracture was subjected to a pre-defined shear stress of τ=1 MPa (Figs. 2.7c and 2.7c). Although the normal stresses applied to the fracture surface in the last two tests were similar to that of Test 2, the flow rate experienced a significant increase during the final pressure increment, rising from around 80 ml/min to a value surpassing 100 ml/min. This rapid increase in the injection flow rate was probably associated with the development of larger flow paths resulting from shear slip and dilation.

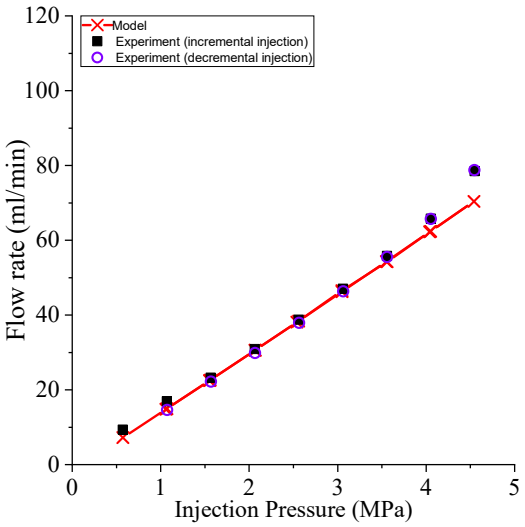
The results of the numerical models are also depicted in Fig. 2.7. In the absence of shear loading, the hydraulic aperture function in Eq. 2.10 includes only the initial and

reversible terms (b_{ini}, b_{el}). The testing results of isotropically loaded samples (tests 1 and 2) were utilized to back-calculate the parameters required for the initial and reversible hydraulic aperture model for both smooth and rough surfaces. On the other hand, the flow rate evolution in Tests 3 and 4 were adopted to estimate the irreversible term of hydraulic aperture function b_{shear} as well as the frictional properties of the fracture zone. The model calibration resulted in two different sets of parameters for the smooth and rough fracture surfaces (Tables 2.1 and 2.2). The aperture is an equivalent effective aperture computed alongside the equivalent permeabilities using the cubic law.

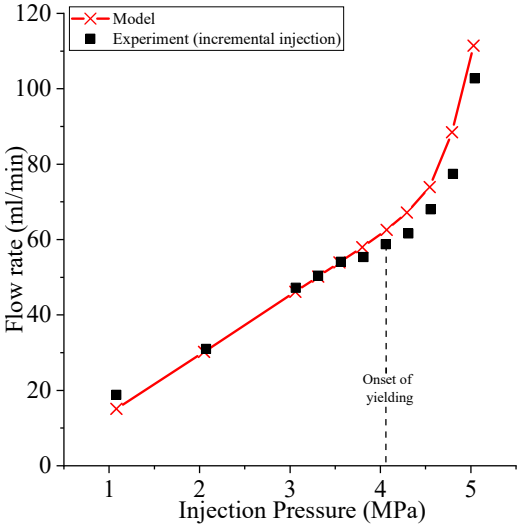
In Test 1, the numerical maximum flow rate is 3.6% lower than the experimental value. However, overall, the experiment and test exhibited a similar trend. For Test 2, the numerical maximum flow rate is 11.8% lower than the experimental one. Despite this, the experiment and test generally followed a close trend, with some discrepancies noted particularly at an injection pressure of 4 MPa. Test 3 showed a numerical maximum flow rate 8.4% higher than the experimental value. Although the experiment and test generally followed a similar trend, there were some deviations, especially noticeable at an injection pressure of 3.8 MPa. This discrepancy tended to increase with higher injection pressures. In Test 4, the numerical maximum flow rate is 5.8% lower than the experimental one. Overall, the experiment and test exhibited some deviation, especially notable at an injection pressure of 3 MPa. However, as shearing commenced, the model and experiment became more aligned. The model's testing is confined to a specific range of stresses and fluxes. The maximum injection pressure reaches 15 MPa for a smooth fracture and 4.5 MPa for a rough fracture. The stress range varies from 10 MPa for a smooth fracture to 3 MPa for a rough fracture. These values represent a subset of realistic hydraulic, tectonic and gravitational stress ranges that could occur in certain reservoirs.



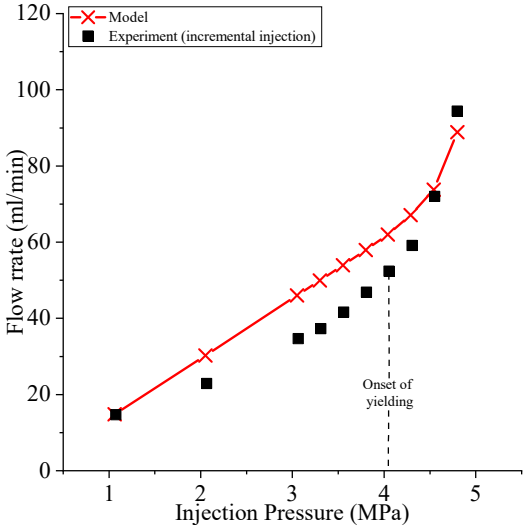
(a) Test 1: $\sigma_n = 10$ MPa and $\tau = 0.0$ MPa



(b) Test 2: $\sigma_n = 3$ MPa and $\tau = 0.0$ MPa



(c) Test 3: $\sigma_n = 3$ MPa and $\tau = 1.0$ MPa



(d) Test 4: $\sigma_n = 3$ MPa and $\tau = 1.0$ MPa

Figure 2.8: Flow rate versus injection pressure along with the numerical modeling results; a) Test 1, isotropic loading/smooth fracture; b) Test 2, isotropic loading/rough fracture; c) Test 3, shear loading/rough fracture; d) Test 4, shear loading/rough fracture

2.3.2 Flow rate versus injection pressure

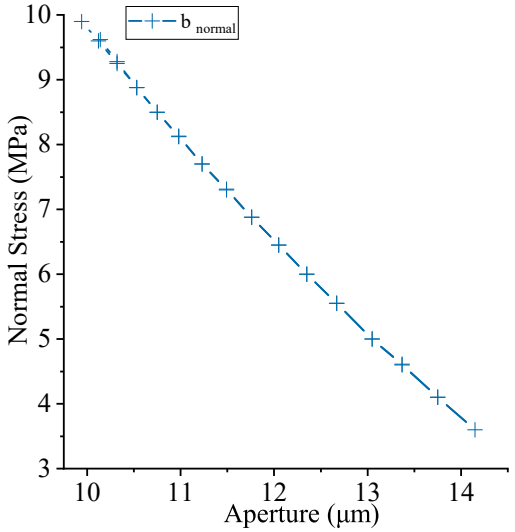
The relationship between injection pressure and the resulting flow rate is depicted in Fig. 2.8. In the first test, the flow rate showed a linear increase up to an injection pressure of nearly 4 MPa, indicating a constant hydraulic aperture within this pressure range. However, beyond 4 MPa, the flow rate curve deviated from linearity and gradually increased as the injection pressure elevated to 15 MPa (Fig. 2.8a). Since no shear stress was applied in this test, the deviation from linearity is likely a result of the normal opening and closure of the fracture induced by the high injection pressure. During the pressure recovery phase, the flow rate values followed the same nonlinear curve, indicating the reversibility of the process. The model incorporated the aperture function b_{el} in Eq. 2.11 to describe the reversible nonlinear evolution of flow rate as a result of changes in the effective normal stress on the fracture plane. However, this non-linear evolution of flow rate was not observed in the second test. The results exhibited an almost perfectly linear increase in flow rate up to an injection pressure of 4.5 MPa (Fig. 2.8b). This observation suggests that mechanical deformations in the fracture, such as opening and closure, had a negligible impact on hydraulic behavior. Two key factors support this observation: 1) the injection pressure was not sufficiently high to substantially open the fracture, and 2) the shear stress on the fracture plane was zero in this test (no sliding). Figs. 2.8c and 2.8d depict the flow rate-pressure curves for the injection tests on rough fractures subjected to a predefined shear stress. In both experiments, the flow rate exhibited an almost linear increase with the rising injection pressure, up to a pressure of almost 4.5 MPa (similar to test3). Subsequently, a pronounced and rapid increase in flow rate occurred as the pressure approached 5 MPa. The rate of change in flow curve was notably higher than that observed in the first test. Hence, this abrupt rise in flow is thought to be due to dilation and consequently leading to an irreversible increase in flow rate.

2.3.3 Injection-induced permeability change

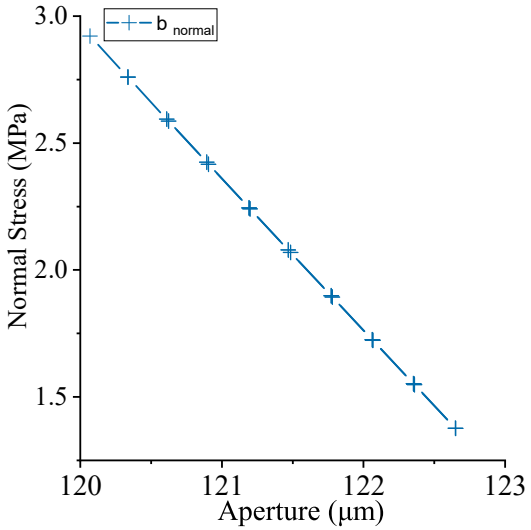
During the experiments, the hydraulic parameters such as hydraulic aperture and fracture permeability were not directly measured. Instead, these parameters were inferred from numerical modeling results, calibrated using other measurable quantities including flow rate and pressure. Figures 2.10 and 2.11 illustrate changes in hydraulic aperture values and resulting permeabilities around the injection point derived from the numerical modeling results. The quantity b_{normal} in these figures represents the summation of the initial and reversible terms of the aperture function, i.e., $b_{\text{normal}} = b_{\text{ini}} + b_{\text{el}}$. Figs. 2.10a and 2.10b depict changes in b_{normal} in tests 1 and 2, respectively (b_{shear} was zero in the absence of shearing). In the first test, the hydraulic aperture b_{normal} increased from the initial value of 10 μm to 14 μm as the injection pressure reached 15 MPa. A similar increase in hydraulic aperture b_{normal} was obtained by the model for the second test, i.e., from the initial value of 120 μm to 123 μm for a pressure increase of 4.5 MPa. The back-calculated hydraulic aperture for the rough fracture surface was nearly one order of magnitude larger than that of the smooth fracture, explaining the possible reason for the substantially different flow rates observed in Tests 1 and 2. In addition, the relative change in hydraulic aperture for the rough fracture, i.e., the ratio between the aperture opening and the initial hydraulic aperture, was much smaller than that of the smooth fracture. Consequently, the induced changes in aperture were expected to have a minor influence on permeability in Test 2. The permeability evolution in tests 1 and 2 around the injection point are depicted in Figs. 2.10c and 2.10d, respectively. The back-calculated permeability of the rough fracture was almost 3 orders of magnitude larger than the permeability of smooth fracture. For the smooth fracture, the fracture permeability increased from 9.0e-17 m^2 to 2.1e-16 m^2 (almost double), while for the rough fracture, permeability remained almost constant at approximately 1.5e-13 m^2. The changes in effective normal stress at the injection point on the fracture plane have been also shown in Figs. 2.10c and 2.10d. In both cases, the effective normal stress decreased during the fluid injection phase, fol-

lowed by a reversible increase during the pressure recovery phase. Figs 2.9*a* and 2.9*b* illustrate how the aperture changes around the injection point based on the effective normal stress for both smooth and rough fractures. Similarly, Figures 2.9c and 2.9d illustrate how the aperture changes with injection pressure. In a smoother fracture, the asperities (roughness) are smaller, resulting in a smaller aperture when two blocks come into contact, as compared to a rough fracture with larger asperities. Additionally, due to the higher initial stress and smoother fracture walls, the initial aperture is lower in smooth fractures, and the relative change in aperture with stress variation is more pronounced compared to rough fractures. For instance, when the effective normal stress drops by approximately 185%, the aperture of a smooth fracture increases by about 40%, whereas for a rough fracture, a drop of about 114% in effective normal stress leads to only a 2.25% increase in aperture. Consequently, the opening and closing behavior of a rough fracture is significantly less than that of a smooth fracture due to differences in their stiffness.

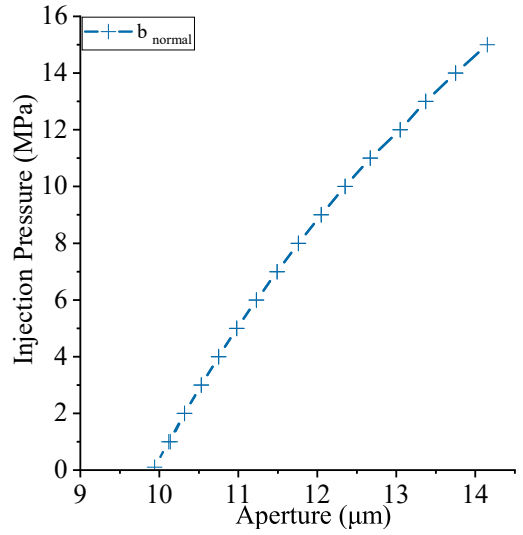
In Tests 3 and 4, the total hydraulic aperture includes both b_{normal} and b_{shear} terms. The evolution of these terms are shown in Figs. 2.11a and 2.11b. The magnitude of changes in b_{normal} obtained for tests 3 and 4 was similar to that of Test 2, given the nearly identical surface roughness and injection protocols in these tests. However, a rapid increase in the irreversible part of hydraulic aperture, b_{shear}, was obtained when the injection pressure exceeded almost 4 MPa. This abrupt increase in b_{shear} resulted from plastic shear strain around the injection point, leading to dilation and subsequently irreversible shear-induced opening. In Test 3, an increase of almost 27 μm was obtained for the irreversible hydraulic aperture b_{shear} when the injection pressure reached 5 MPa (Fig. 2.11a). The calculated b_{shear} value at the peak pressure in Test 4 was lower than in Test 3, but the rapid increase was still remarkable (Fig. 2.11b). Figs. 2.11c and 2.11d show the changes in effective normal stress at the injection point and resulting permeability for Tests 3 and 4, respectively. The permeability increase in Test 3 was more pronounced, likely due to the lower normal stress reached and higher plastic strain.



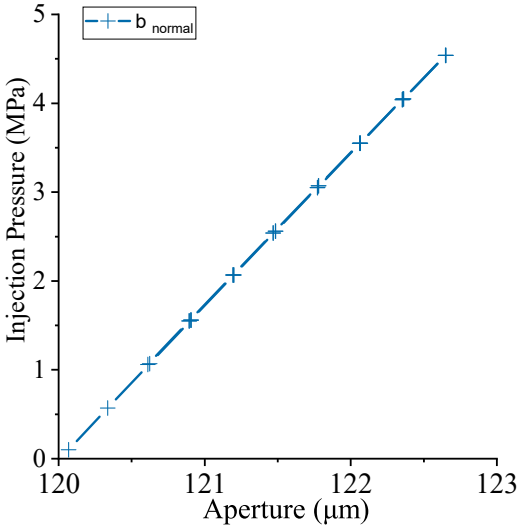
(a) Test 1: $\sigma_n = 10$ MPa and $\tau = 0.0$ MPa



(b) Test 2: $\sigma_n = 3$ MPa and $\tau = 0.0$ MPa

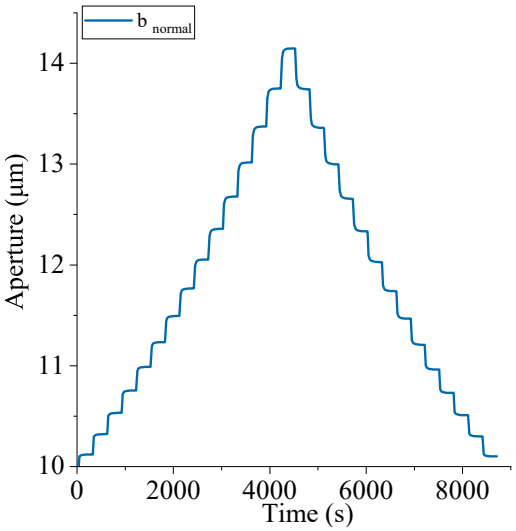


(c) Test 1: $\sigma_n = 10$ MPa and $\tau = 0.0$ MPa

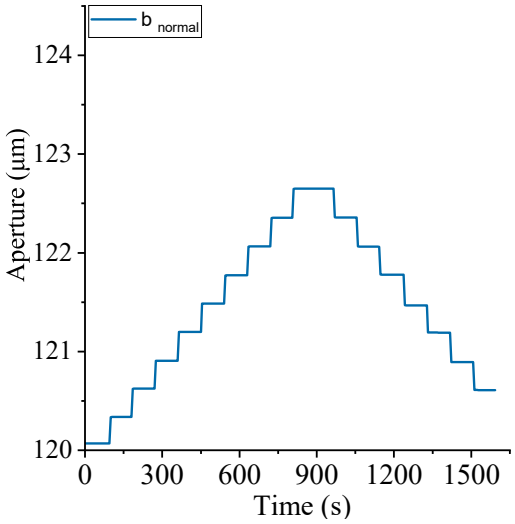


(d) Test 2: $\sigma_n = 3$ MPa and $\tau = 0.0$ MPa

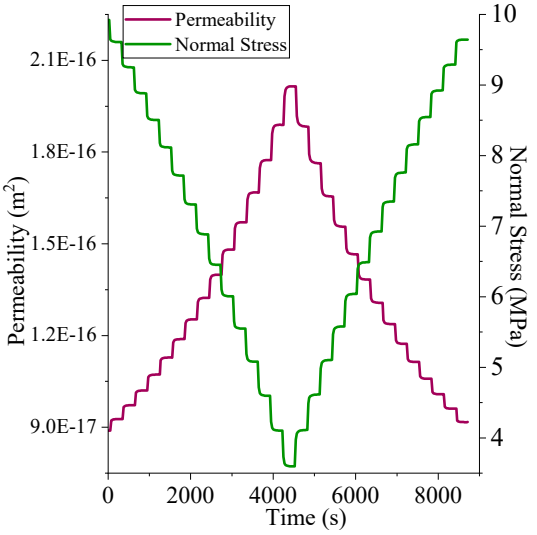
Figure 2.9: Changes in hydraulic aperture and effective normal stress obtained from numerical modeling; a) hydraulic aperture in Test 1, isotropic loading/smooth fracture; b) hydraulic aperture in Test 2 c) hydraulic aperture in Test 1, isotropic loading/smooth fracture; d) hydraulic aperture in Test 2



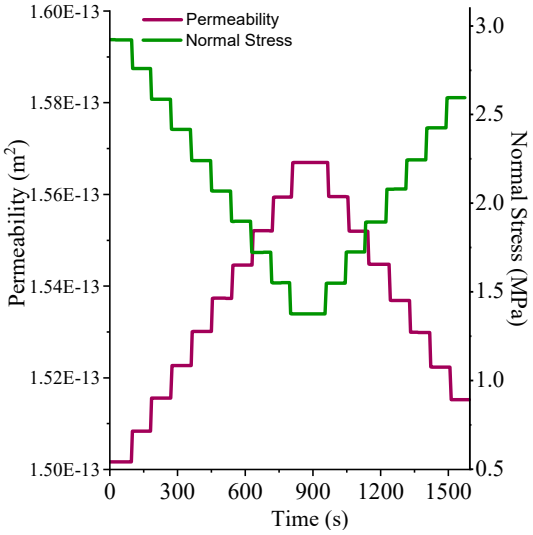
(a) Test 1: $\sigma_n = 10$ MPa and $\tau = 0.0$ MPa



(b) Test 2: $\sigma_n = 3$ MPa and $\tau = 0.0$ MPa



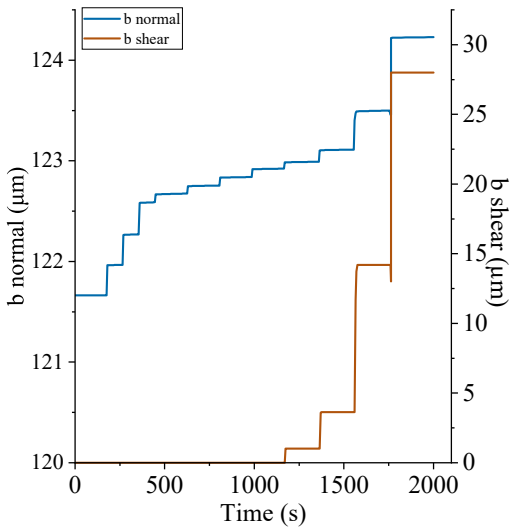
(c) Test 1: $\sigma_n = 10$ MPa and $\tau = 0.0$ MPa



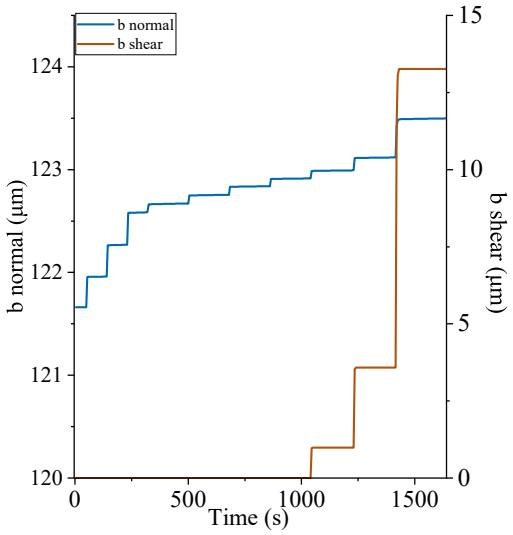
(d) Test 2: $\sigma_n = 3$ MPa and $\tau = 0.0$ MPa

Figure 2.10: Changes in hydraulic aperture and permeability of fracture obtained from numerical modeling; a) hydraulic aperture in Test 1, isotropic loading/smooth fracture; b) hydraulic aperture in Test 2, isotropic loading/rough fracture; c) permeability in Test 1, isotropic loading/smooth fracture; d) permeability in Test 2, isotropic loading/rough fracture

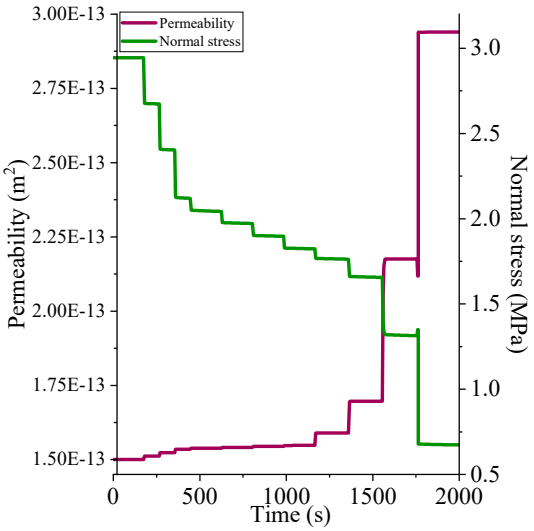
The permeability value increased by almost twofold in this experiment. Fig. 2.12a depicts the contour plot of effective normal stress $\sigma_n^{'}$ on the fracture plane for Test 3, obtained from the numerical modeling. As illustrated, there is a high gradient in the normal stress distribution around the injection point. Fig. 2.12b displays the distribution of effective normal stress value along a horizontal line along the fracture. The remarkable normal stress gradient results from the fracture's connection to the atmosphere, leading to a substantial fluid pressure gradient from the injection point towards the fracture boundaries. The lowest value of effective normal stress is obtained around the injection point, where the fluid pressure is highest. As shown in Fig. 2.12c, theoretically, the onset of plastic dilation occurs when the effective normal stress on the fracture plane reduces to a value of 1.4 MPa (assuming a friction angle of 37°, Table 2.1). Under this stress condition, the Mohr-Coulomb plastic yield criteria were satisfied, leading to the initiation of shear-induced dilation. The contour plot of b_{shear} parameter on the fracture plane is shown in Fig. 2.12d (for Test 3). The distribution of this parameter is directly correlated with the plastic strain developed along the fracture plane. Modeling results indicate that shear-induced dilation and irreversible aperture increase are localized within a small zone, with a diameter of 8.4 mm, around the injection point. The size and distribution of the plastic dilation zone depend on the effective stress distribution on the fracture plane. As indicated in Fig. 2.12b, only a small zone, approximately 8.4 mm in diameter, experiences an effective normal stress less than 1.4 MPa.



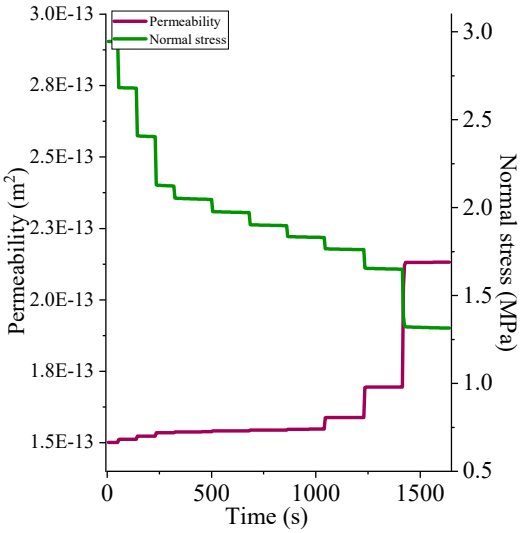
(a) Test 3: $\sigma_n = 3$ MPa and $\tau = 1.0$ MPa



(b) Test 4: $\sigma_n = 3$ MPa and $\tau = 1.0$ MPa



(c) Test 3: $\sigma_n = 3$ MPa and $\tau = 1.0$ MPa



(d) Test 4: $\sigma_n = 3$ MPa and $\tau = 1.0$ MPa

Figure 2.11: Changes in hydraulic aperture and permeability of rough fracture obtained from numerical modeling; a) hydraulic aperture in Test 3; b) hydraulic aperture in Test 4; c) permeability change in Test 3; d) permeability change in Test 4

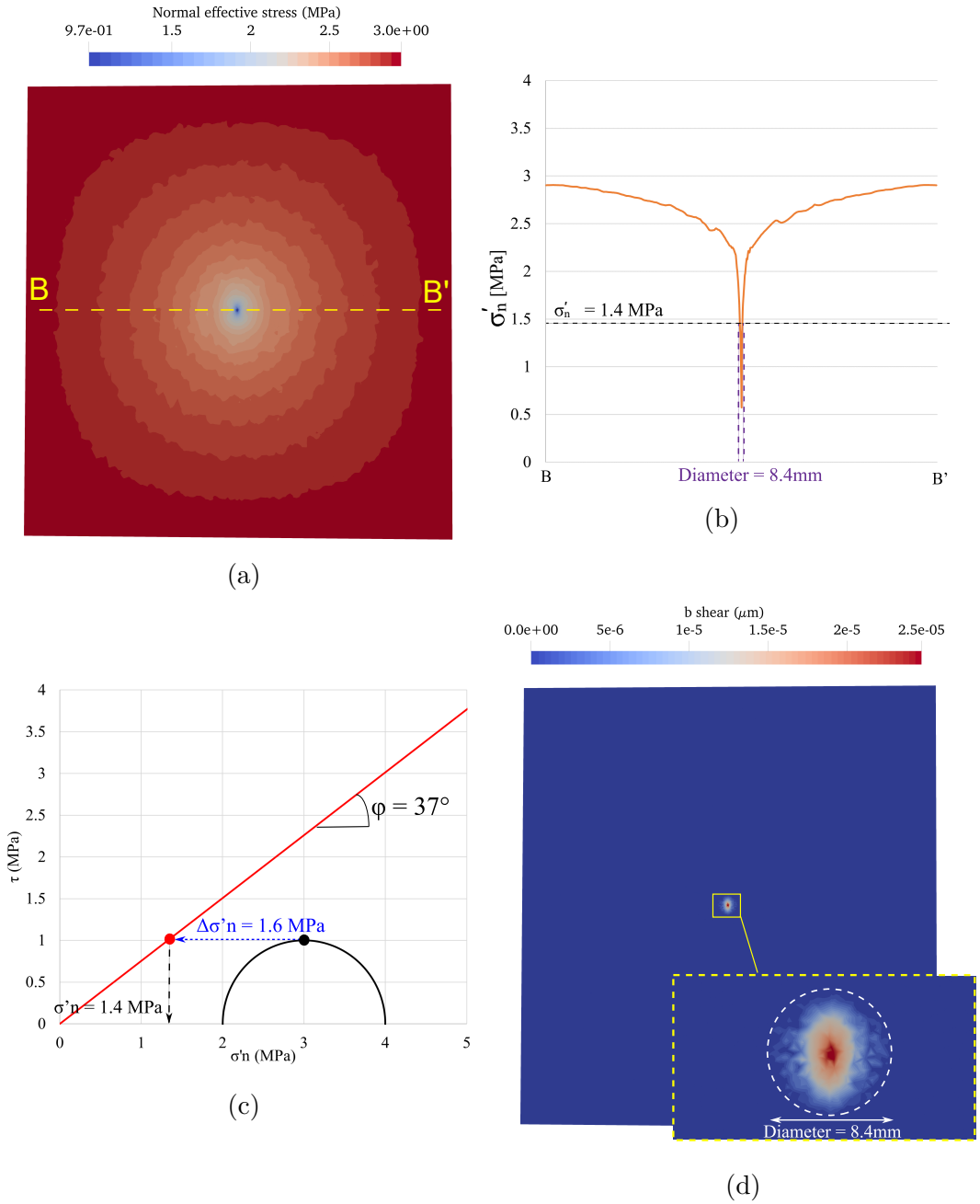


Figure 2.12: a) The contour plot of normal effective stress on the fracture plane for Test 3; b) the distribution of normal effective stress along a horizontal line passing through; c) the initial effective stress state in Test 3 and the required condition to satisfy the Mohr-Coulomb failure condition; d) the fracture A vertical cut though the fracture showing contour plot b_{shear} value in Test 3

2.4 Summary and Conclusion

Understanding the evolution of fracture permeability is crucial for characterizing fluid transport in fractured rocks and developing strategies to enhance the productivity during hydraulic stimulation of geothermal reservoirs. An important factor in this context is how fluid pressure affects permeability. In this study, I used a series of laboratory experiments with pressure-controlled injection into smooth and rough fractures in granite under pre-stressed conditions. A coupled hydro-mechanical modeling framework was employed to describe the permeability of fracture taking into account the changes in hydraulic aperture as a function of effective normal stress and plastic shear-induced dilation. Moreover, a slip-weakening Mohr-Coulomb model was used to describe the progressive shear slide under compression and the post-failure behavior of pre-existing fractures.

The study involved deriving hydraulic parameters, such as hydraulic aperture and fracture permeability, from numerical modeling results calibrated with measurable quantities like flow rate and pressure. The experiments showed substantial differences in flow rate evolution between smooth and rough fractures, highlighting the important role of fracture asperities on the permeability. Additionally, the tests with pre-defined shear stress on the fracture plane exhibited notable increases in irreversible permeability due to plastic shear strain, leading to significant slide-induced dilation, showing a nearly twofold increase in permeability. The roughness of a fracture influences the changes in permeability induced by fluid injection. Rough fractures exhibit fewer changes during stimulation compared to smooth fractures. However, initiating shear sliding in smooth fractures is more complex. Additional sources of complexity include thermo-hydro-chemo-mechanical effects, creep, and heterogeneities can alter the fracture behavior. To tackle these challenges, an extension of the experimental setup and numerical framework is necessary. For example, a more detailed analysis of the fracture surface topography before and after a test could help to assess stress heterogeneity and validate the permanent aperture changes. Further research in this direction is impera-

tive to explore various scenarios and derive useful, quantitative conclusions applicable to real-world reservoir.

Chapter 3

Numerical Modeling of Hydro-Mechanical Processes during Hydraulic Testing of Pre-existing Fractures at the Grimsel Test Site, Switzerland[b]

Abstract

This chapter presents a fully coupled hydro-mechanical framework for modeling hydraulic shearing in a mesoscale reservoir located at the Grimsel Test Site, Switzerland. The experiment was conducted on a ductile-brittle fault embedded in low-permeable granite. I observe that normal fracture opening temporarily increases flow capacity, while fracture sliding locks asperities, leading to a non-recoverable increase in flow. To couple these processes, I use a poro-elasto-plastic constitutive framework and employ a permeability function that depends on several parameters, such as dilation angle, in-situ stresses, residual aperture and maximum aperture. My results capture the recorded pressure responses well, and indicate that the permeability changes by one order of magnitude during the experiment.

[b] This chapter has been published in Geomechanics for Energy and the Environment [Ouf et al., 2024a].

3.1 Introduction

In deep geothermal systems, fluid predominantly flows through the network of fractures rather than directly through the host rock. These pre-existing fractures serve as the primary conduits for fluid movement between the injection and extraction wells. The fracture network is limiting the ability of a reservoir to carry enough heat [Saar, 2011] and fluid flow to be economically viable [Breede et al., 2013]. The permeability at these depths is often less than 10^{-16} m^2 [Manning and Ingebritsen, 1999], making it difficult to achieve an economically viable flow rates in the reservoir. To enhance the permeability in fractures at these depths, hydraulic stimulation can be employed. Such systems are referred to as Enhanced Geothermal systems (EGS).

Hydraulic stimulation for EGS includes the creation of new fractures due to hydraulic fracturing (HF) and/or dilation of existing fractures due to hydraulic shearing (HS). In HF, a fluid is injected into the rock until it fails under tensile opening, causing the creation of new cracks and the extension of existing ones. Proppants might be utilized to maintain these fractures open. In contrast, HS opens existing fractures by injecting fluid. Due to anisotropic stress conditions, natural rough fractures which support shear stresses may dilate upon hydraulic shearing and interlock once the fluid injection stops [Pine and Batchelor, 1984, Cladouhos et al., 2009]. Studies by McClure and Horne [2014], Gischig and Preisig [2015] have shown that both HS and HF processes share common mechanisms, although one mechanism may prevail over the other. Our study focuses exclusively on Hydraulic Testing of Pre-existing Fractures (HTPF). Notably, our proposed framework concentrates on modeling HS, with the modeling of HF being beyond the scope of this chapter.

On the laboratory scale, considerable research efforts have been devoted to investigating the correlation between effective stress and permeability in fractures. These studies involved conducting laboratory-scale tests, which subsequently yielded empirical relationships widely employed in practical applications [Barton, 1973, Goodman, 1974, Bandis et al., 1983, Yeo et al., 1998]. Meso-scale (decameter scale) reservoirs were

studied to bridge laboratory test scale to reservoir scale, which contribute to improving the understanding of fracture hydraulics and mechanics during stimulation [Jung, 1989, Rutqvist, 1995, Guglielmi et al., 2015]. Petty et al. [2013] explore the responses of different fractures to different injection scenarios. In a separate study, Krietsch et al. [2020] found that these tests provided valuable insights into water circulation, rock deformation, and seismic activity triggered by stimulation. Guglielmi et al. [2017] demonstrates on a meso-scale that minor slip movements, typically sub-millimeter in size, lead to substantial increases in permeability. Rutqvist [2012] shows that stress and permeability relationships are scale dependent. Zimmermann and Reinicke [2010] investigated the fracture conductivity of a real-scale reservoir to gain insights into its long-term injectivity. Recently, Kukkonen et al. [2023] stimulate fractures at a depth of 6km, the permeability was almost fully recovered, with only minor permeability gain upon pressure release.

Numerical modeling plays a crucial role in enhancing our understanding of hydraulic stimulation mechanisms. It allows for the estimation of fracture properties through the calibration of numerical models, including fracture normal and shear stiffnesses, as well as the dilation angle. Several EGS project sites have been investigated using numerical modeling techniques. Notable examples include Soultz-sous-Foret in France [Baisch et al., 2010], Fenton Hill in New Mexico, USA [Rinaldi and Rutqvist, 2019], Groß Schönebeck in Germany [Blöcher et al., 2018], and Pohang in South Korea [Yoo et al., 2021].

Fracture stimulation, induced by water injection, has notable effects on porosity, intrinsic permeability, and local effective stress. In addressing fracture problems, two primary categories of numerical approaches are employed: the continuum and discontinuum representation of fractures. Rutqvist et al. [2020] conducted a comparative study on fracture stimulation techniques, evaluating both continuum and discontinuum methods. Their findings indicate that both approaches adequately reproduce the key hydro-mechanical processes taking place within the faults. The implicit representation of fractures captures the impact of fractures by using an equivalent porous media. Var-

ious examples of well-known codes that utilise this approach are OpenGeoSys [Kolditz et al., 2012], MOOSE framework [Permann et al., 2020], TOUGH-FLAC [Itasca, 2011, Rutqvist, 2017], and CODE_BRIGHT [Gens et al., 1996]. Conversely, the explicit representation of fractures attempt to more realistically include the geometry and impact of fractures, and almost always require some special treatment. Notable examples of these techniques are FEM-DEM/cohesive zone modeling [Lisjak et al., 2014, Grasselli et al., 2015], 2) Discrete Fracture Network using interface elements [Gischig and Preisig, 2015], 3) Embedded lower dimensional elements [Watanabe et al., 2012] which are employed for explicit fracture modeling.

In order to attain a more comprehensive understanding of the processes underpinning hydraulic shearing on a broader scale, several in-situ investigations have been undertaken, for example, the In-situ Stimulation and Circulation (ISC) experiments at the Grimsel Test Site in Switzerland [Amann et al., 2018, Jalali et al., 2018, Krietsch et al., 2018]. These investigations encompassed a range of tests, including hydraulic fracturing and hydraulic shearing, aimed to improve the understanding on fault responses under varying hydraulic stimulation conditions. By integrating the hydromechanical responses of the rock mass, these studies have significantly deepened our understanding of the intricate reactions of faults when subjected to hydraulic stimulation.

The objective of this work is to numerically replicate a selected stimulation at the Grimsel test site. In this study, a continuous modeling approach is utilized. It considers the fault zone as an equivalent porous media, incorporating both the normal elastic opening of the fracture and the shear-slip dilation that happens during hydraulic shearing. The objectives of this study are:

- Accurately reproduce the flow rate and injection pressure at the injection well by including HS processes.
- Simulating the fracture pressure propagation during stimulation within a fault zone.
- Evaluation the model's reliability and predictive capabilities in representing real-

world hydraulic shearing scenarios

3.2 Grimsel Test Site

The In-situ Stimulation and Circulation (ISC) experiment at the Grimsel Test Site, located in Switzerland, aims to investigate open questions related to deep geothermal reservoirs. Specifically, the focus is on understanding the interaction among hydraulics, mechanics, and seismicity of the rock and fractures during reservoir stimulations, using the site as a decameter-scale analog reservoir [Amann et al., 2018]. To accomplish this, the experiment is conducted under various stress states and hydraulic conditions and monitored through a combination of geophysical, hydrological, and geomechanical techniques.

The Grimsel test site is located within two granite units, the Grimsel Granodiorite and Central Aar Granite, and is situated approximately 480m below the surface. Fig. 3.1 shows the investigated volume of the ISC contains two sets of shear zones, namely the ductile shear zones S1.1, S1.2, S1.3, and the brittle-ductile shear zones S3.1 and S3.2 [Keusen et al., 1989b]. The investigation revealed the presence of three S1 shear zones and two S3 shear zones, which have an average orientation of 142/77 (dip direction/dip) and 183/65, respectively [Krietsch et al., 2019].

Furthermore, the S1 and S3 shear zones are identifiable from the surface and can be traced back to a distance of approximately 500 meters [Schneeberger et al., 2017]. The average thickness of S1 ranges from 173 to 1670 mm, while S3 ranges from 38 to 312 mm [Krietsch et al., 2018]. The investigated ISC volume is intersected by two tunnels, the AU-tunnel and VE-tunnel. These tunnels were excavated in 1983. Additionally, the observed in-situ pressure in the experimental rock volume of the ISC is around 0.2-0.3 MPa, as a result of long-term drainage of the nearby tunnel [Krietsch et al., 2018].

An extensive campaign to characterize the in-situ stress conditions was conducted on the site [Krietsch et al., 2019]. The principal stress obtained from inverting strains and additional constraints from hydraulic fracturing give on average; $\sigma_1 = 13$ MPa

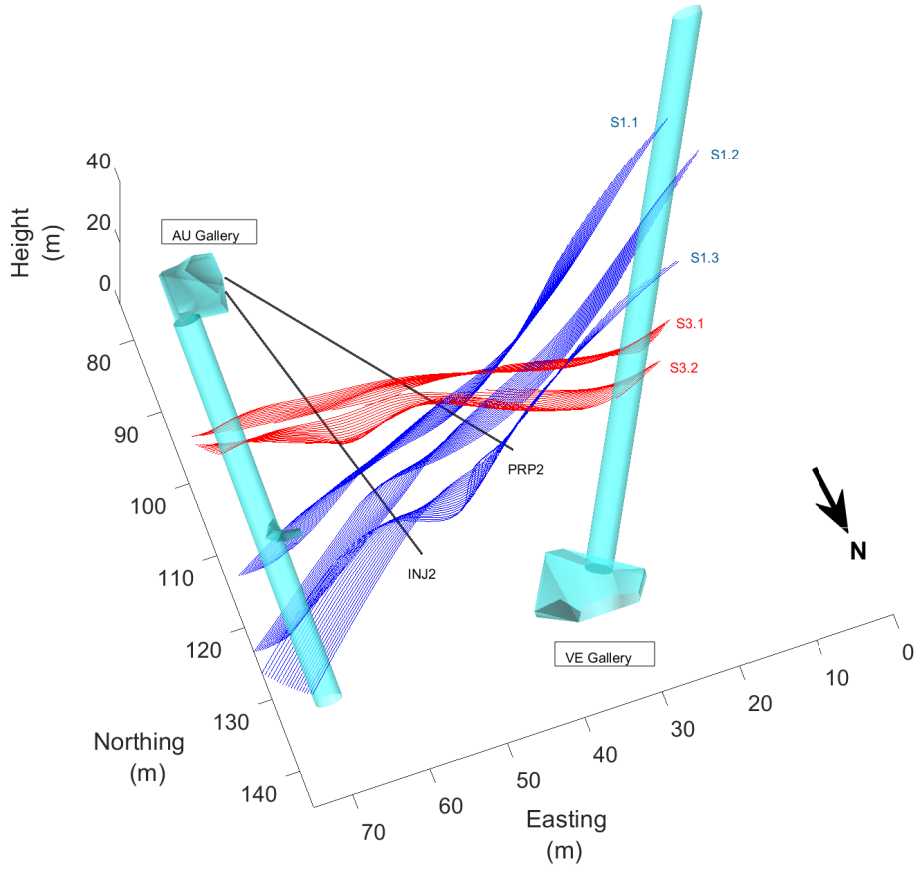


Figure 3.1: Grimsel In-situ Stimulation and Circulation Test Site - Modified after Krietsch et al. [2018]

135/15 (dip direction/dip), σ_2 = 8 MPa 21/43, σ_3 = 6.25 MPa 234/33. The complete GTS data can be found at the following link: https://doi.org/10.3929/ethz-b-000276170 [Doetsch et al., 2018].

3.3 HS1 stimulation

The HS1 experiment was carried out on February 15, 2017, in the injection borehole INJ2 with the objective to increase the permeability by stimulating the ductile shear zone S1.3 with high pressure injections using a straddle packer system. An additional

fracture pressure monitoring system, labeled PRP2, was located 10.72 m from the injection point [Krietsch et al., 2020].

The injection protocol comprised four cycles, with the first two cycles serving as pre-stimulation phases (i.e. two consecutive pressure controlled HTPF tests (hydraulic testing of pre-existing fractures), with the objectives: 1) to break down cohesive bonds 2) to reopen existing fractures and 3) to determine the initial injectivity and normal stress across the fault zone. The third cycle, referred to as the main stimulation phase, was flow rate controlled and caused the fault zone to open and shear. Injection pressure reduction during flow rate increase during the third stimulation cycle suggested a mixed mode response between hydraulic shearing and hydraulic fracturing [Krietsch et al., 2020]. The final cycle (i.e. a pressure controlled HTPF test) aimed to determine the final injectivity and potential changes in normal stress conditions. This study specifically focuses on the last cycle (Cycle 4). The comprehensive details of stimulation process can be found in the refs [Krietsch et al., 2020] and [Krietsch, 2019].

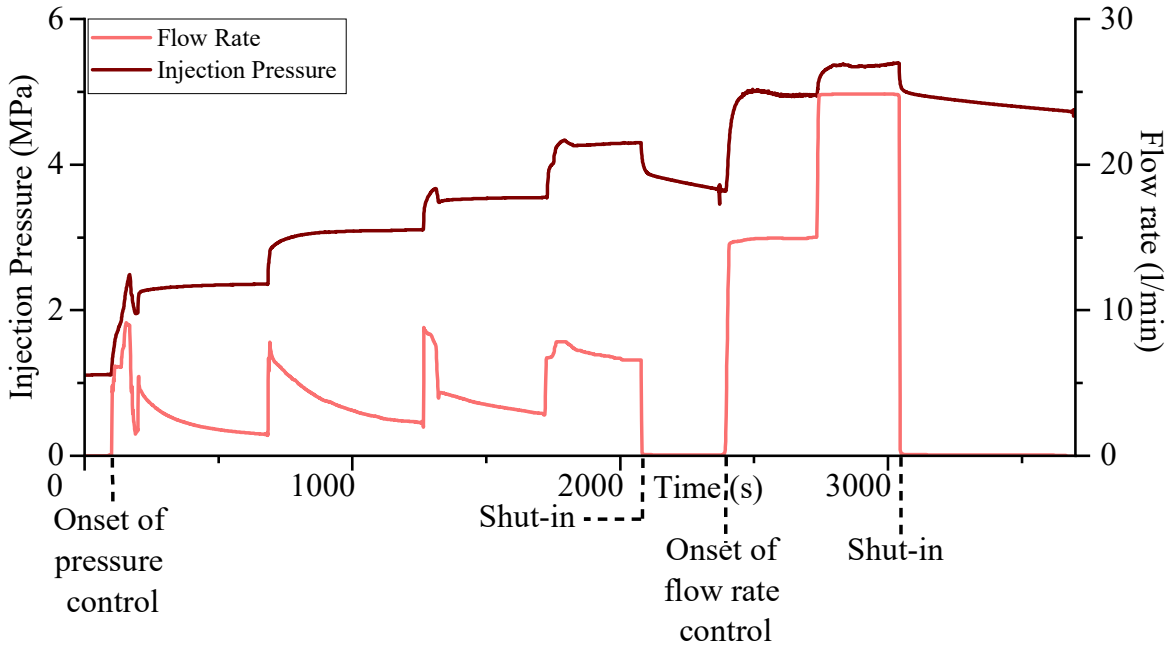


Figure 3.2: In-situ Injection INJ2: Six Injection Steps of Cycle 4 Post-Stimulation Phase - Modified from Krietsch [2019]

The various injection steps of cycle 4 are illustrated in Fig. 3.2, with a summary of

these steps is provided in Table 3.1, highlighting the parameters controlled. In total, cycle 4 consists of six steps and includes two shut-in periods (i.e. injection is temporarily stopped).

Table 3.1: Injection steps within cycle 4 of HS1

Step	Control	Value	Duration
Step 1	Pressure control	2.32 MPa	592.5 s
Step 2	Pressure control	3.07 MPa	677 s
Step 3	Pressure control	3.51 MPa	450 s
Step 4	Pressure control	4.27 MPa	365 s
Shut-in	-	-	335 s
Step 5	Flow rate control	15 l/min	340 s
Step 6	Flow rate control	25 l/min	308 s
Shut-in	-	-	760 s

3.4 Modeling approach

3.4.1 Fully coupled numerical simulator

The primary objective of this study is to replicate the fracture behavior observed during the cycle 4 injection of the HS1 experiment. The numerical model was developed using the Multiphysics Object-Oriented Simulation Environment (MOOSE) framework [Permann et al., 2020], which is an open-source finite element method (FEM) platform created by Idaho National Laboratories. This framework offers a flexible and hybrid parallel environment designed for solving multiphysics and multi-component problems in an implicit manner. MOOSE relies on advanced mesh libraries such as libMesh that provide support for adaptive mesh refinement (AMR) computations in parallel [Kirk et al., 2006]. It relies on PETSc (Portable, Extensible Toolkit for Scientific Computation) for the scalable (parallel) solution of scientific applications modeled by partial differential equations [Balay et al., 2017].

An Equivalent Continuum Modeling approach (ECM) was utilized to characterize the hydro-mechanical processes within pre-existing fractures, eliminating the need

for computationally intensive treatments such as solving mechanical contact problems. This simplifies the adoption of the approaches explored here. ECM is able to deliver a fully coupled solution and a 3D approach, facilitating a more realistic capture of flow rates while eliminating simplifications such as plain strain or stress. The ECM approach facilitates the solution of fully coupled multi-physics problems with greater ease compared to other methods. Specifically, ECM enables the solution of the kernel in an unstaggered scheme, which is notably more complex when using a discontinuum approach. As a result, the approaches explored in this study have the potential for widespread adoption due to their enhanced efficiency and applicability.

In this method, the fracture was represented as a finite-thickness porous medium with equivalent hydro-mechanical properties, while the intact rock was treated as a low-permeability material. To account for changes in permeability within the fracture zone, an aperture-dependent permeability function was employed. The fracture permeability model was integrated into the multi-physics finite element code MOOSE framework [Wilkins et al., 2020, 2021], with additional support from the PorousFlow and TensorMechanics modules to solve the coupled hydro-mechanical equations.

3.4.2 Model Set up

The modelling domain was 90 m × 90 m × 50 m (see Fig. 4.2), with only the S1.3 fault and the bulk rock modeled, and inclusion of the injection point INJ2. Pore pressures are extracted at the location of the PRP2 fracture pressure probe. Following Krietsch et al. [2018], the fault width in the model was assumed to be 80 centimeters with a dip direction/dip of 142/77. The positive Y-axis is aligned with the North direction and the positive X-axis with the East direction, while the positive Z-axis points upwards Fig. 4.2.

The tunnels present at the test sites were not modelled. Hydraulically, the fault zone was represented as a permeable porous medium, whose permeability depends on an aperture function (see Section 2.2.2). Mechanically, the stress-strain relationship in

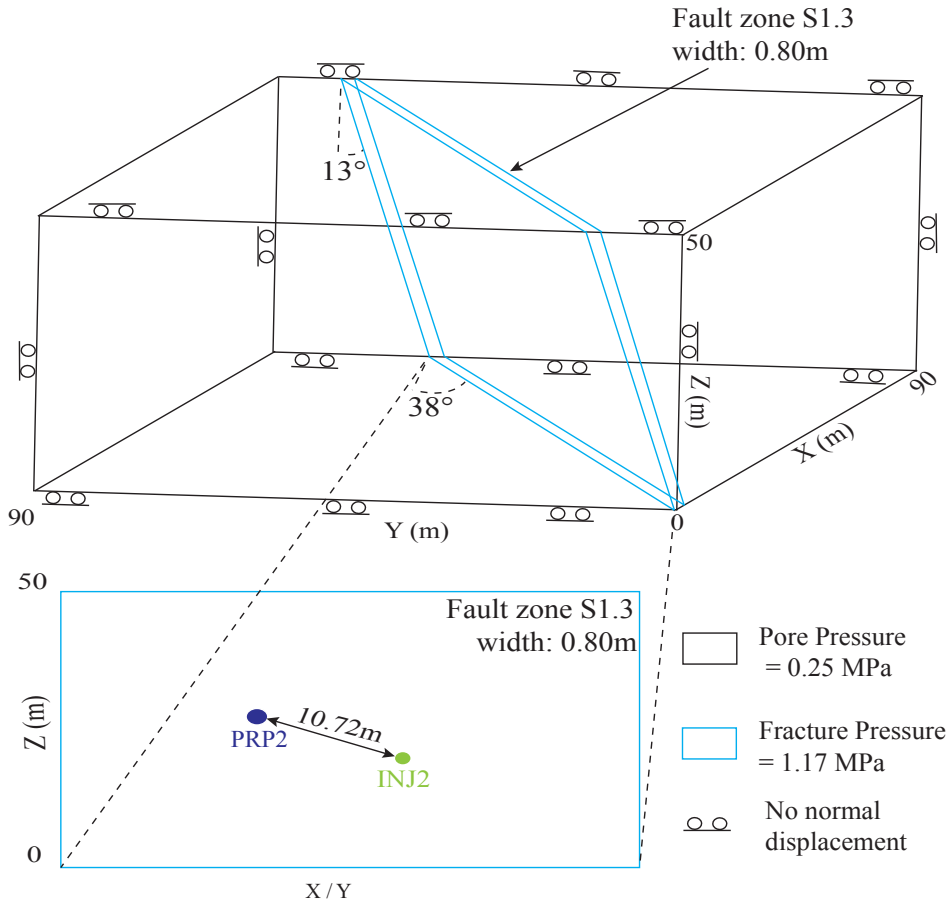


Figure 3.3: Numerical model with boundary conditions and location of PRP2 and INJ2

the fault zone was based on an elasto-plastic Mohr-Coulomb law, softening is not included in this framework. The host rock permeability was assumed to be constant (i.e. stress independent). The stress-strain relationships of the host rock was assumed to be linear elastic (i.e. Hooke's law with Young's modulus E and Poisson's ratio ν). The injection process was simulated using a single point (0D element) positioned at the location of INJ2. The fault pressure was tracked at a node located at the same position as probe PRP2, which was 10.72 m away from INJ2 (Fig. 4.2). The model is considered isothermal, with both the bulk rock and fault zone assumed to be fully saturated. The hydraulic boundary conditions were established for granite rock with no-flow boundaries, whereas the fault zone was assigned a boundary condition of 1.17 MPa water pressure matching the initial measured in situ pressures. Consequently, the

Table 3.2: Hydromechanical properties of the model. Properties were adopted from Doetsch et al. [2018][a], Keusen et al. [1989a][b], Nagra NIB 95-062 [c] and Krietsch et al. [2020][d].

Parameters	Symbol	Granite Bulk	Fault zone
Geomechanical			
Biot coefficient	(α_b)	1	1
Young Modulus	(E)	47 GPa[a]	30 GPa[a]
Poisson's ratio	(ν)	0.3[a]	0.25[a]
Rock density	(ρ_r)	2640 kg/m^3[a]	2640 kg/m^3[a]
Porosity	(n)	1 %[b]	75 %
Cohesion	(c)	-	0[c]
Friction angle	(ϕ_r)	-	25°[b]
Dilation angle	(ψ)	-	24°
Hydrogeological			
Permeability	(k)	(k_{bulk}) 10^{-22} m^2[b]	(k_{frac}) variable
Fluid density	(ρ_f)	1000 kg/m^3[d]	1000 kg/m^3[d]
Fluid Viscosity	(μ_f)	10^{-9} MPa.s[d]	10^{-9} MPa.s[d]
Fluid Bulk modulus	(K_f)	2 GPa[d]	2 GPa[d]

Table 3.3: Parameters of the permeability function for the fault zone S1.3

Parameters	Symbol	Fault zone
Initial aperture	(b_{ini})	17 (μm)
Maximum elastic aperture	(b_{max})	800 (μm)
Stress dependency	(α)	0.275 (MPa^{-1})
Fracture spacing	(s_f)	1 (m^{-1})

fracture accommodated leak-off. The initial water pressure was 1.17 MPa in the fault zone and 0.25 MPa in the host rock. Both initial and boundary condition are based on Krietsch et al. [2018], Krietsch [2019]. The mechanical boundary conditions were set as no displacement boundaries in the direction normal to the domain boundaries Fig. 4.2. The initial stress tensor used was adapted from Krietsch et al. [2019], and reported in Section 3.2, and gravity is not included in the model, due to the limited size and high water pressures. The model boundaries (vertical faces) are perpendicular to the principal stress directions. The neglect of gravity is also present in other fracture stimulation studies with high dip angles, such as 65° in Rutqvist et al. [2020] and 70

to 90° in Cappa et al. [2006].

Fracture zone homogenisation can be idealised as an equivalent porous medium in the case of GTS ductile shear zone due to the small variation in permeability within the fault zone, as discussed by Wenning et al. [2018]. Assuming linear flow and homogenization over the entire interval, the continuum equivalent porous media was reproduced with the fault zone width and fault zone properties given by Doetsch et al. [2018]. Properties for the host rock and fracture zone are summarized in Table 4.1. The parameters used in the Table 3.3 are parameters of the permeability function for the fault zone S1.3. They are calibrated to reproduce as closely as possible the observations. The initial aperture was assumed 20 μm which is based on the measured hydraulic conductivity of 7×10^{-9} m/s [Brixel et al., 2020]. The parameters used to calibrate are non-unique. The fault zone contains a single fracture as suggested by the geophysics investigation [Doetsch et al., 2020]. I reproduced the injection scenario following the protocol shown in Table 3.1. The simulation began 100 seconds before the start of injection cycle 4. The pressure-controlled injection was carried out in four steps from 100 to 2075 seconds, while the flow rate was monitored. The injection was stopped between 2075 s and 2445 s followed by the two flow rate controlled steps. During the flow rate control phase from 2445 s to 3025 s, fracture pressure was monitored. The injection was stopped at 3025 s, and the stimulation was completed at 3800 s.

3.4.3 Hydraulic & mechanics formulations

The same formulation as Chapter 2 is used for this model. Softening is not modeled in this chapter.

3.4.4 3D FE modeling of the experiments

The mesh within the fault zone was finer compared to the host rock and further refined between PRP2 and INJ2. The whole model consists of ca. 120 000 nodes and ca. 710 000 elements (Fig. 3.4). I employed the Galerkin finite element method with first-order La-

grange shape functions. Quadrature techniques, primarily Gaussian Quadrature, were used for numerical integration over the reference element. To mitigate volumetric locking, I utilized the b-bar approach within the MOOSE framework, as elaborated in the provided link MOOSE SolidMechanics. In addressing concerns about shear locking, I kept element aspect ratios close to 1 throughout our investigations. Additionally, I exercised caution in determining fracture thickness and final mesh count to avoid very thin elements that might introduce distortion and unwanted numerical artifacts.

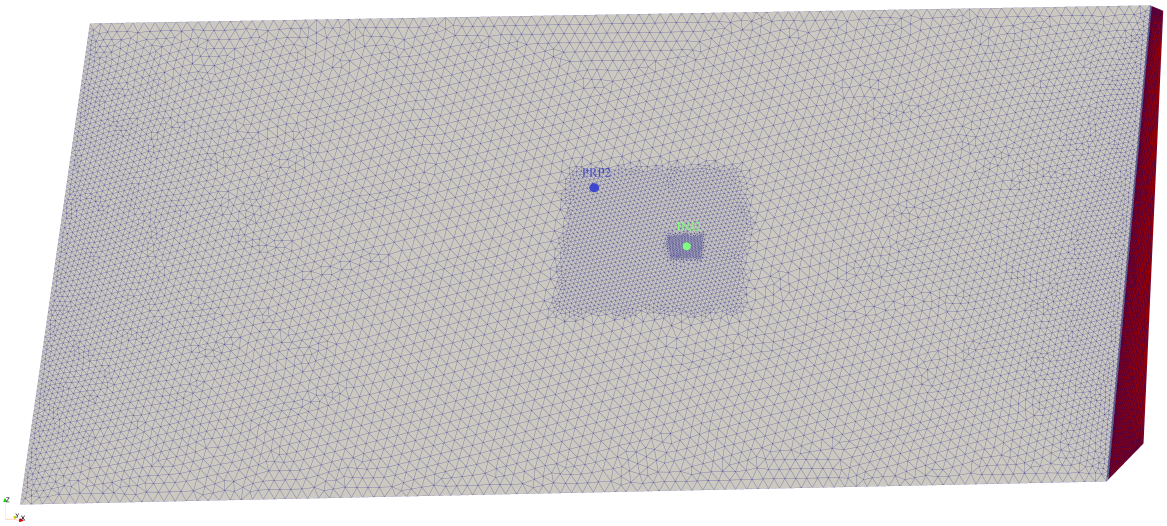


Figure 3.4: The mesh of fault within the model showing a refined area around the injection point

Fig. 3.5 highlights the model's sensitivity to variations in mesh density. I evaluated the maximum injection pressure response at INJ2 across six steps. I have increased the number of elements and nodes only in the refined area, which is shown in Fig. 3.4. As the number of elements increases, the accuracy of the model improves. Fig. 3.5 illustrate the convergence of the maximum pressure and plastic tangential strain response with increasing mesh density. Convergence is achieved with 508 132 tetrahedral elements, and the final model, with 715 056 tetrahedral elements, is considered the most accurate. To prevent distortion and numerical artifacts, further increases in the number of elements were avoided. With a stable plastic tangential strain and pressure response influenced by permeability and plastic properties the model appears to be appropriately

meshed.

Fig. 3.6 shows the evolution of tangential plastic strain at different elements. Mechanical convergence is again achieved at 508 132 tetrahedral elements. Figs. 3.6b and 3.6c illustrate the same tangential plastic strain pattern across the fault.

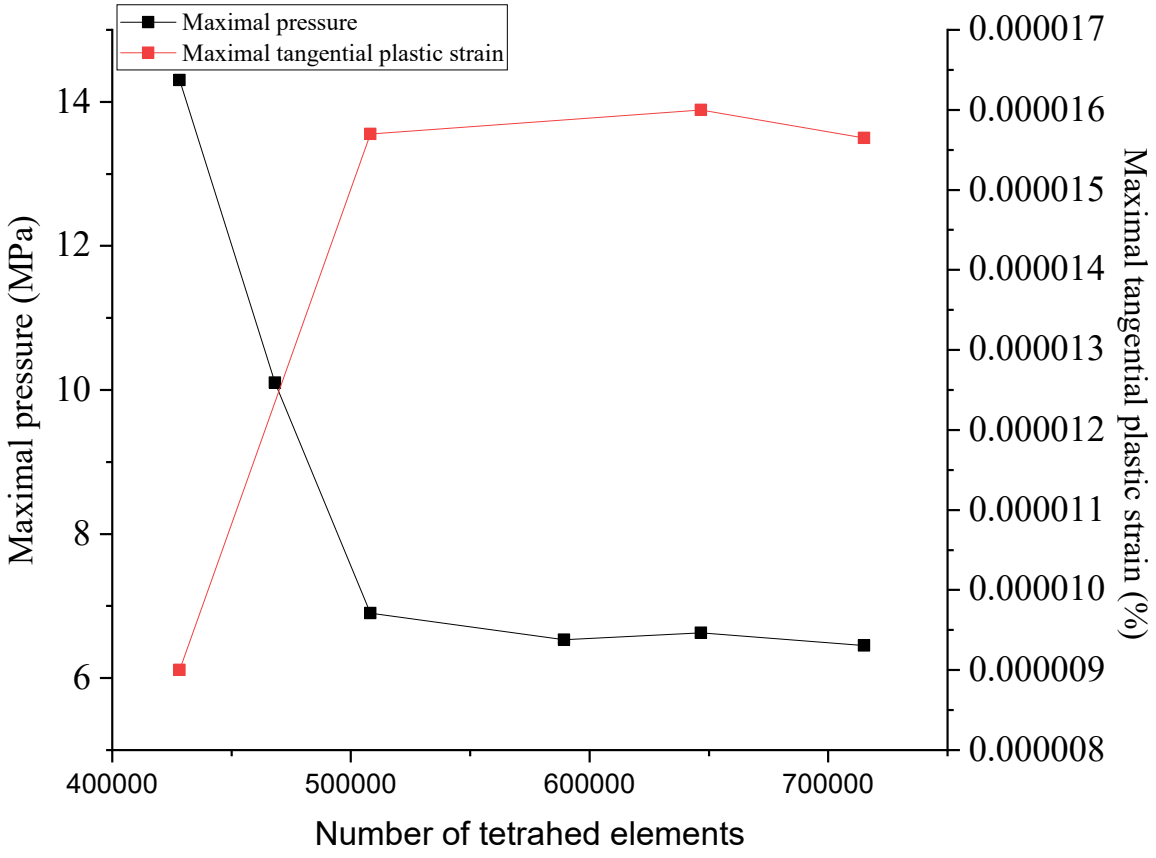
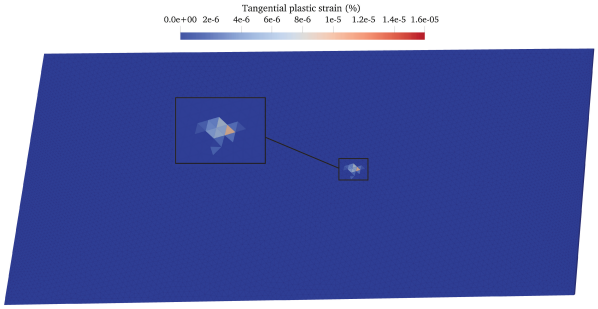


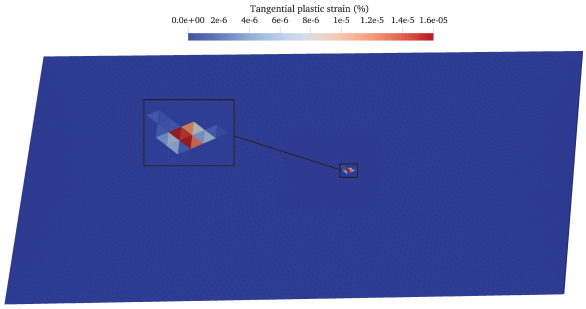
Figure 3.5: Mesh convergence study for plastic strain and pore pressure

3.5 Simulation results

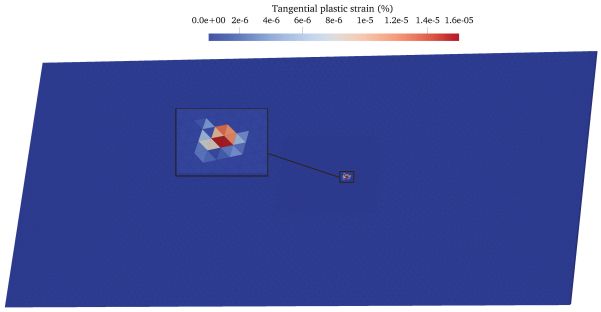
In this section, I present the numerical results of the simulation. The simulation used Table 3.1 as input, with the first four steps modeled for pressure control and steps five and six for flow rate control. The experimental results and associated calibrated numerical results are shown in Fig. 3.7. The first four steps of the injection were



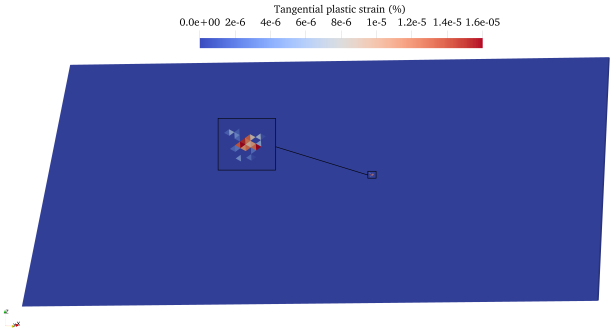
(a) 428 192 elements



(b) 508 132 elements



(c) 646 644 elements



(d) 715 056 elements

Figure 3.6: Tangential plastic strain at mesh density; a) 428 192 elements b) 508 132 elements c) 646 644 elements d) 715 056 elements

modeled as pressure controlled steps, and therefore match the experimental results closely (shown in Fig. 3.7a). The corresponding flow rates during these steps (Fig. 3.7b) showed a sudden increase during the first three steps, followed by reaching a steady state. In contrast, the experimental results show a similar, but slightly higher, initial increase in flow rate, which then more gradually decreased in a hyperbolic manner until a steady state was reached at a value that matches well the numerical results. In the fourth step, the flow rate exhibits a more pronounced increase and subsequently undergoes a more minor decay before reaching a steady state. This is interpreted as the initiation of hydraulic shearing.

During the first shut-in phase, the measured injection pressure exhibited a slight decrease, reaching a value of 3.6 MPa, while numerically, it sharply dropped to 1.84 MPa (Fig. 3.7a), most likely due to the model boundary conditions that allow a leak off. The pressure response during the last two steps, under flow rate control, show a good qualitative agreement between the numerical simulation and the field data, albeit with the numerical results requiring a higher injection pressure than in the experiment. At a flow rate of 15 l/min, the injection pressure stabilized at 4.95 MPa in the field and at 5.37 MPa in the numerical simulation. Similarly, at a flow rate of 25 l/min, the injection pressure stabilized at 5.37 MPa in the field and at 6.45 MPa in the numerical simulation. After the final shut-in period, the injection pressure decreases sharply to 2.23 MPa in the numerical simulation, whereas experimentally, it gradually decreased to 4.73 MPa, again probably due to the model boundary conditions.

The pressure monitoring point PRP2, shown in Fig. 3.7c, shows an excellent general agreement with the experimental results. It initially showed a value of 1.17 MPa, and exhibited a slight increase during the first three steps, both numerically and experimentally. At the end of the third step, the measured pressure reached 1.45 MPa, while the numerical simulation yielded a value of 1.38 MPa. During the fourth step, the fracture pressure increased at higher rates due to shear induced changes in permeability. Numerically, the fracture pressure at PRP2 reached 1.54 MPa, while the on-site measurement was 1.55 MPa. During the first shut-in period, the pressure of the numerical simula-

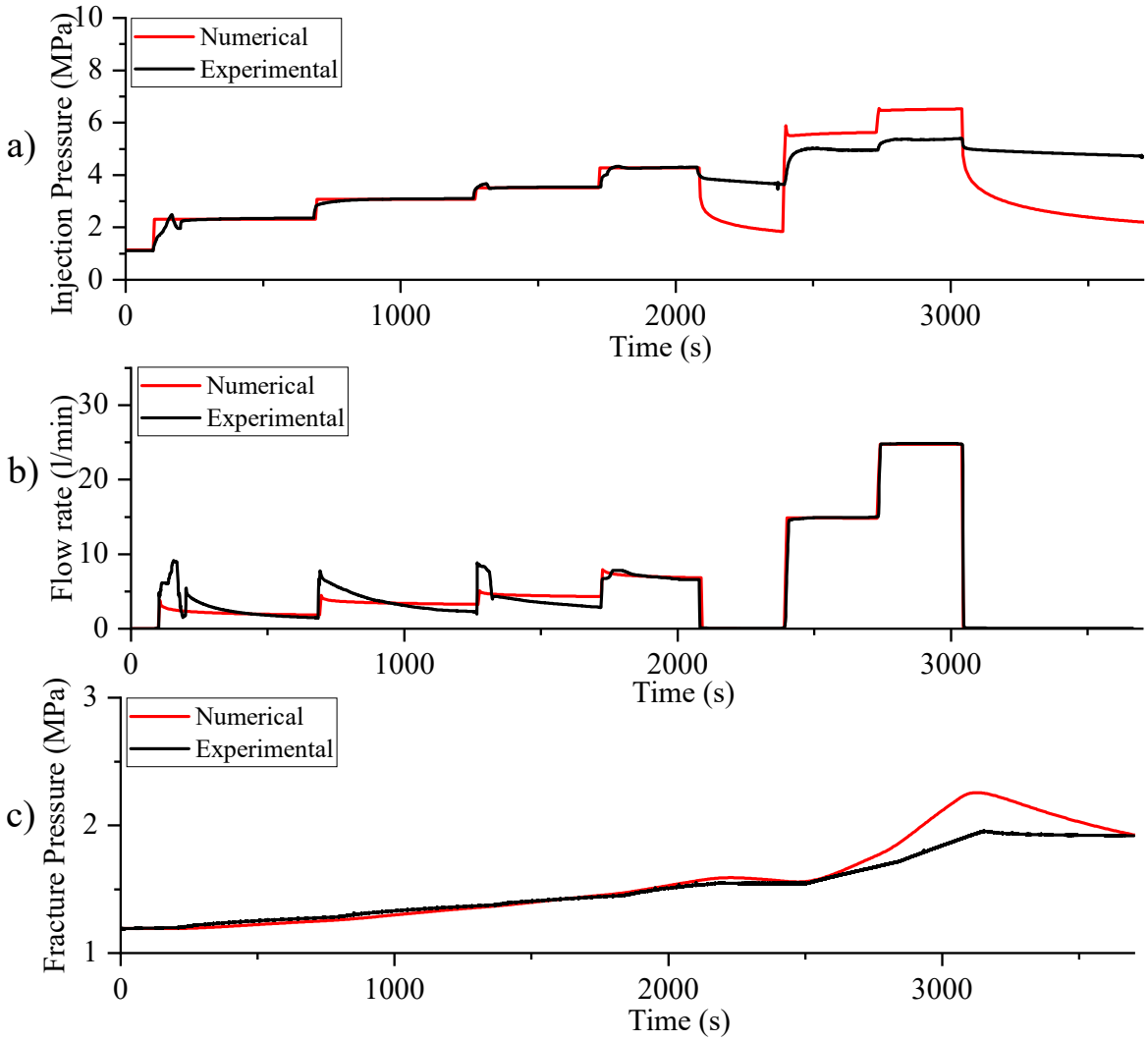


Figure 3.7: a) Injection pressure at INJ2, b) Flow rate at INJ2, c) Fracture pressure at PRP2

tion and the actual measured values remained virtually constant. Higher permeability changes were observed during the two flow rate injection steps. At the end of the fifth steps, the modelled fracture pressure at PRP2 reached 1.92 MPa, whereas the on-site measurement reached 1.76 MPa. During the final step the on-site fracture pressure reached a maximum of 1.95 MPa, while numerically it increases to 2.21 MPa. During the shut-in period, the on-site fracture pressure remains constant at 1.95 MPa, while numerically it dropped to 1.92 MPa (Fig. 3.7c).

The flow rate and pressure at steady state are presented in Fig. 3.8. I calculated

the average flow rate and injection pressure for the final 50 seconds of each step. As shown in Fig. 3.8, the numerical simulation accurately captures the behavior up to the fourth step, which are mostly controlled by recoverable normal opening. The last two steps show an approximate match with the numerical flow rate at 5.37 MPa in the fifth step (compared to the experimental value of 4.91 MPa) and at 6.45 MPa during the last step (compared to the experimental value of 5.36 MPa). In the elastic region, up to 3.51 MPa, the relationship between flow rate and pressure was linear, reflecting the linear elastic granite behaviour. However, for larger pressures a sharp increase in the relationship between flow rate and fracture pressure was observed. Fig. 3.8 suggests a jacking pressure between 3.51 and 4.27 MPa.

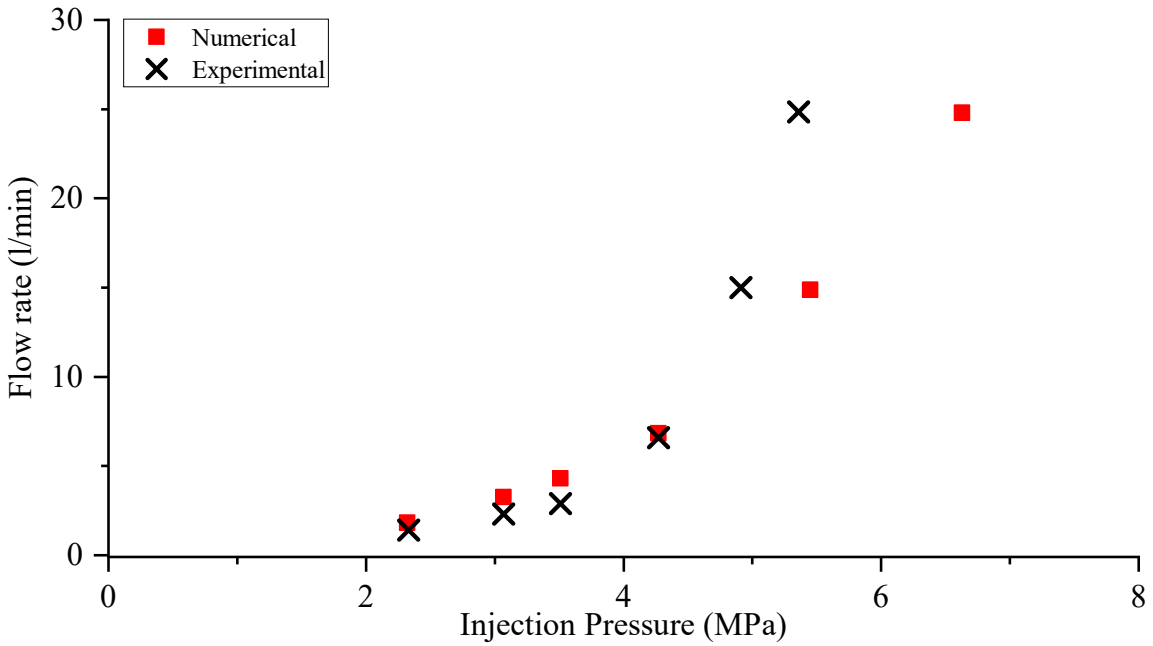


Figure 3.8: Flow rate vs Injection pressure at INJ2

The presented model shows reversible permeability changes during the initial three steps. Specifically, the numerical analysis shows that the fracture opens in a reversible manner. At this stage, the permeability is solely governed by the elastic deformation, denoted as b_{el}. However, the onset of plasticity was observed when the fracture pressure exceeded 4 MPa. This is numerically represented by sliding and dilation of the frac-

ture. Plastic deformations, being irreversible upon pressure release, lead to the creation of irreversible permeability.

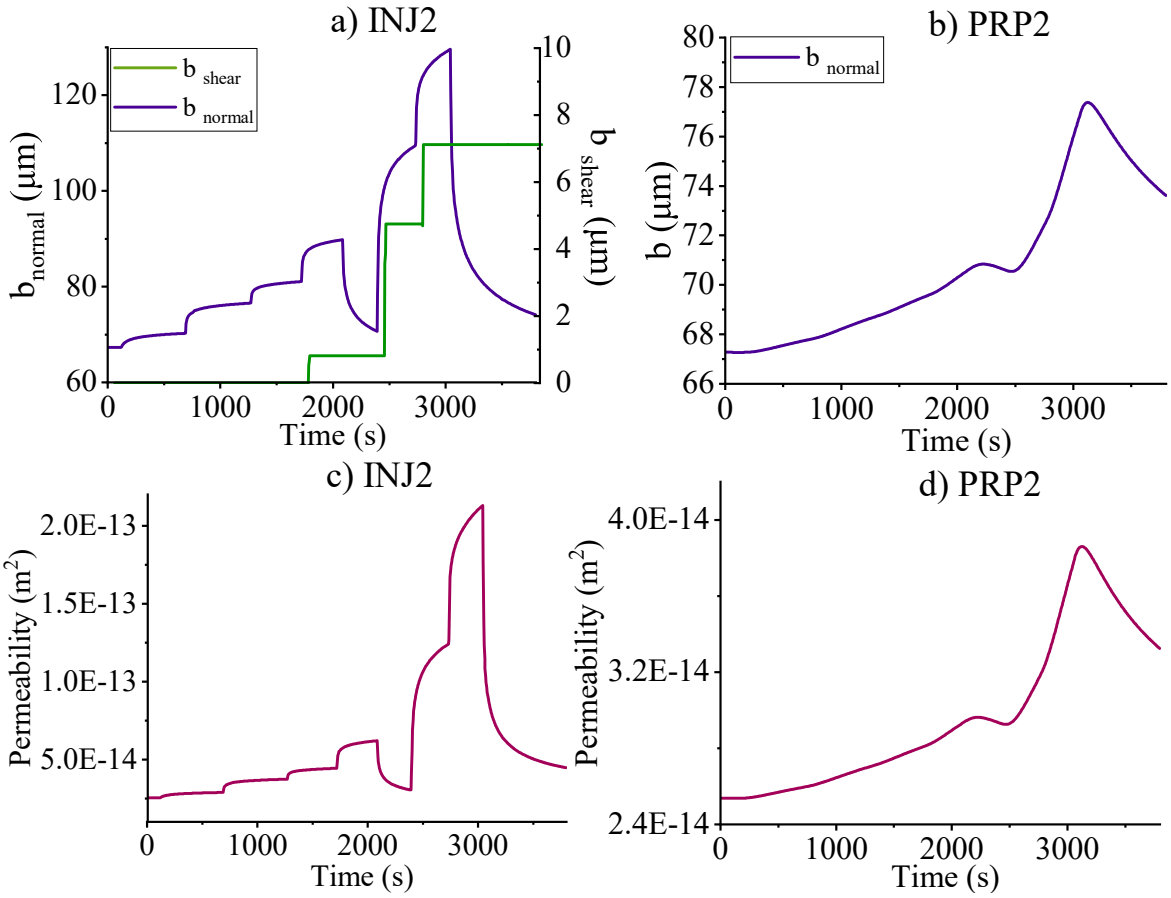


Figure 3.9: Fracture permeability and aperture change; a) Aperture variation over time at INJ2, b) aperture variation over time at PRP2, c) permeability change at INJ2, d) permeability change at PRP2

Fig. 3.9a shows the normal opening (b_{normal}) and shear opening (b_{shear}) of the fault at INJ2. Major fluctuations are observed in the normal opening (b_{normal}), with an initial value of 67.27 μm and a final value of 74.33 μm. The maximum aperture at the highest flow rate was 129.6 μm. Fig. 3.9 - a also suggests that the majority of aperture changes was reversible.

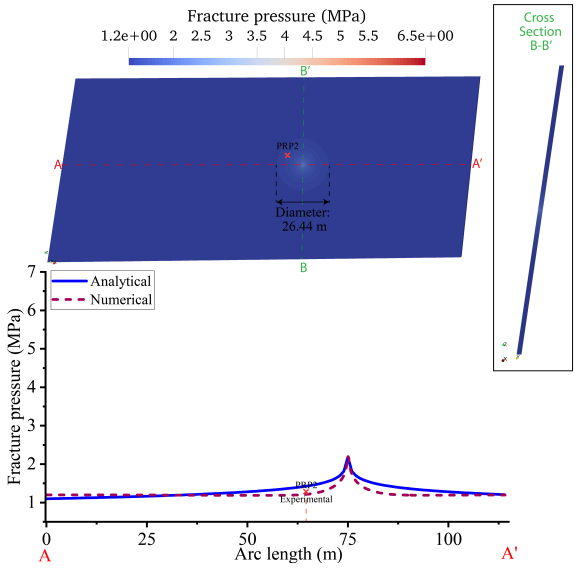
The onset of shear displacement and related aperture changes occured during the 4th step at 1725 seconds, coinciding with an injection pressure of 4.27 MPa. At this stage, the shear aperture reached 0.82 μm. Subsequently, during the 5th step, the shear

aperture further increased to 4.75 μm. In the final step, at a flow rate of 25 l/min, the aperture changes related to shear reached its maximum value of 7.12 μm. Due to irreversible plastic straining of the fault zone, the shear aperture remained (i.e. irreversible) after shut-in, as shown in Fig. 3.9a.

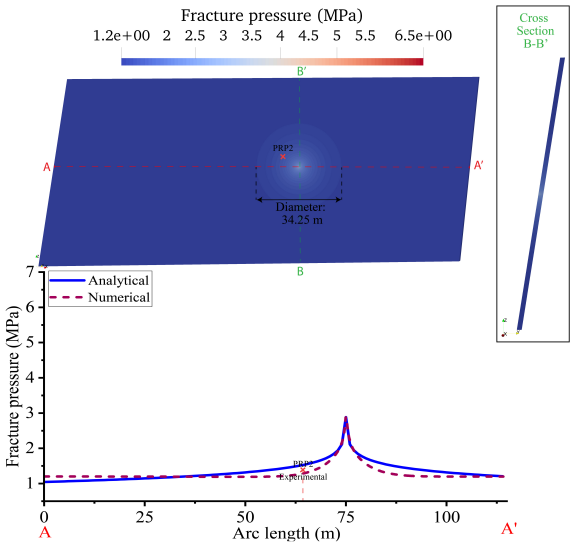
Fig. 3.9c shows the permeability at INJ2. The initial permeability was 2.53 $\times$ 10^{-14} m^2. Over the first three steps, the permeability increased only due to normal opening, reaching 4.44 $\times$ 10^{-14} m^2 by the end of the third steps. In the fourth step, the permeability increased substantially to a value of 6.24$\times$ 10^{-13} m^2, mainly due to normal opening with a minor contribution from shear opening. Upon injection pressure release, the permeability decreased to 3.12 $\times$ 10^{-14} m^2. In the fifth step, the simultaneous increase in b_{normal} and b_{shear} led to a permeability of 1.26 $\times$ 10^{-13} m^2. Finally, during the last step, the permeability reached its maximum value of 2.11$\times$ 10^{-13} m^2. During venting the wellbore, permeability changes were primarily controlled by b_{normal}, and the related permeability at the end of the test was determined to be 4.52 $\times$ 10^{-14} m^2 Fig. 3.9c.

At monitoring point PRP2, no changes in shear displacement (b_{shear}) were detected. Initially, the normal opening (b_{normal}) at PRP2 measured 67.27 μm with a corresponding permeability of 2.53 $\times$ 10^{-14} m^2. The evolution of the normal opening was notably influenced by pressure diffusion. Over the first three steps, a slight increase in b_{normal} was observed, reaching 69.74 μm, accompanied by a gradual rise in permeability to 2.85 $\times$ 10^{-14} m^2. Subsequently, during the fourth step, the increase in b_{normal} became more pronounced due to the initiation of hydraulic shearing at INJ2, resulting in a b_{normal} value of 70.80 μm and a permeability of 2.96 $\times$ 10^{-14} m^2. The maximum value of b_{normal} reached 77.13 μm, with a corresponding permeability of 3.86 $\times$ 10^{-14} m^2, observed when the flow rate was 25 l/min. During the second venting phase, the normal opening gradually decreased, reaching a final value of 73.7 μm, with a permeability of 3.32 $\times$ 10^{-14} m^2 Fig. 3.9b. Notably, since the fracture pressure did not revert to its initial value, the final b_{normal} value exceeded the initial measurement.

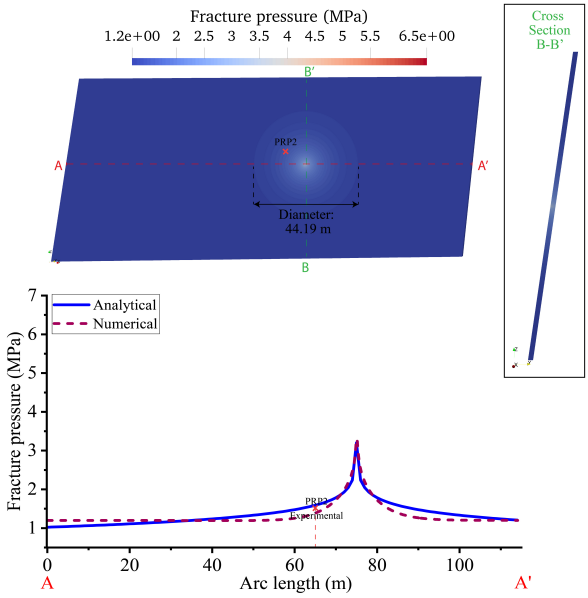
Fig. 3.10 illustrates the spatial variation of pore pressure in the fault zone, termed



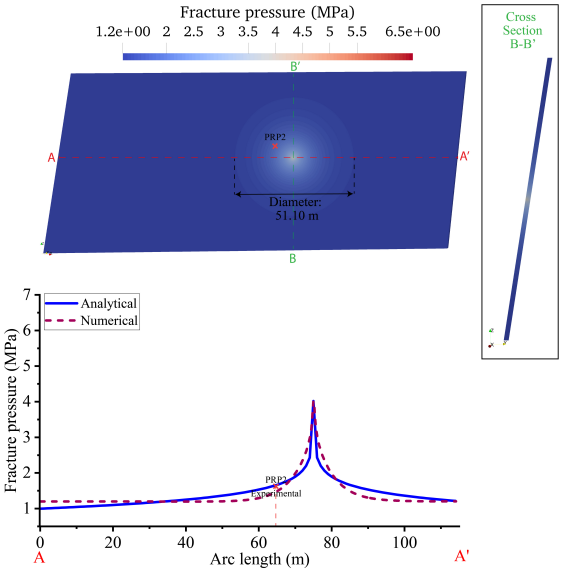
(a) Step 1



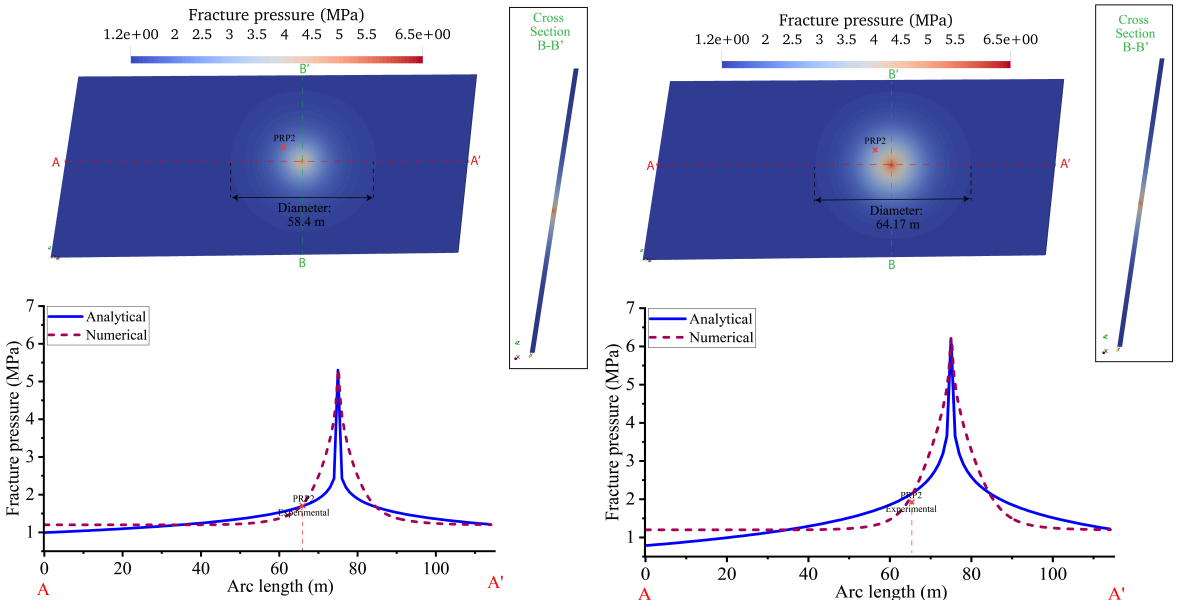
(b) Step 2



(c) Step 3



(d) Step 4



(e) Step 5 (f) Step 6

Figure 3.10: Fracture pressure at different steps; **a)** Step 1 : Injection pressure 2.33 MPa; flow rate 1.82 l/min; time 680 s, **b)** Step 2: Injection pressure 3.07 MPa; flow rate 3.26 l/min; time 1260 s, **c)** Step 3: Injection pressure 3.51 MPa; flow rate 4.3 l/min; time 1720 s, **d)** Step 4: Injection pressure 4.27 MPa; flow rate 6.57 l/min; time 2080 s **e)** Step 5: Injection pressure 5.37 MPa; flow rate 15.00 l/min; time 2730 s , **f)** Step 6: Injection pressure 6.45 MPa; flow rate 25.00 l/min; time 3000 s

the fracture pressure. Each sub-figure represents the fracture pressure at the end of an injection step, showing both a contour plot of the pressure in the fault zone and the values on a section through the fault below (dashed red line). At the end of each injected step, an approximate radial diffusion pattern is shown within the fault. An analytical solution to the radial diffusivity equation for a confined aquifer under semi-steady state conditions [Dake, 1983] is overlain with a solid blue line. This solution uses assumptions that the reservoir is homogeneous in all rock properties, the domain is infinite and isotropic in permeability. Additionally, it assumes that the producing well is completed across the entire formation thickness, ensuring fully radial flow. Furthermore, the formation is considered to be completely saturated with a single fluid. The analytical solution generates a hyperbolic pressure profile in all steps, indicating that the fracture pressure diffuses along the fracture. However, the analytical solution does not stabilize the fracture pressure significantly far away from the injection point. Instead, the fracture pressure decays hyperbolically in all steps until reaching the model's limits. The numerical solution of pressure propagation exhibits a limited radial perturbation of fracture pressure along the fault zone, attributed to the increase in permeability in that zone. Additionally, cross section B-B' in Fig. 3.10 illustrates radial diffusion in the transversal plane. This radial diffusion in the transversal plane shows the same diffusion pattern as the diffusion in the longitudinal plane.

The experimental data obtained at PRP2 show strong agreement with both the numerical model and analytical solution illustrated in Fig. 3.10 across all stages. However, beginning from the fourth stage, stronger disparities emerge between the analytical and numerical solutions regarding fracture pressure around the injection site. This variance becomes more pronounced due to the onset of hydraulic shearing occurring at step 4, and further consequential increases in permeability in this zone. The linear diffusion model does not include a finite domain and the influence of pressure-dependent permeability or aperture increases due to shearing, with only the storage being pressure-dependent. In contrast, the model incorporated the aperture change of the fault with pressure and shear deformation. Consequently, the numerical model predicts a larger

area experiencing higher pressures compared to the analytical solution. As the pressure increases, this disparity between the numerical and analytical models further magnifies.

3.6 Discussion and conclusion

In this chapter, I present a model for permeability enhancement during hydraulic stimulation of a meso-scale reservoir. Our model was designed to represent the conditions observed at the Grimsel ISC test site, and specifically the HS1 stimulation test. The proposed permeability function accounts for both reversible normal opening and irreversible shear opening, providing a comprehensive representation of the system. The model deviates from the experimental results during shut in periods, most likely due to the boundary conditions and limited domain of the model.

Specifically, our investigation revealed that for pressures below the jacking pressure, permeability changes occurred exclusively in an elastic manner. Once the jacking pressure was exceeded, the permeability was controlled by both elastic normal opening and fracture sliding. Our model revealed a permeability increase of approximately 1 magnitude, mostly due to recoverable opening.

To further refine the results, the injection model could incorporate the behavior of a packer system. This method could enhance our simulation results by increasing the accuracy of flow rate versus injection pressure relationship at the INJ2 borehole. Crack formation and extension, which were thought to have occurred during step 3 [Krietsch et al., 2020], but were not integrated into our model, are likely to have impacted the results. These cracks might have a significant influence on injectivity and pressure response and correspond with the mismatch in results in the last two steps. During the last two steps, the injection pressure responses in the numerical model were consistently higher than those observed in the experimental data. A greater fracture opening or additional cracks in our model would align more closely with the experimental results.

I have showcased, supported by reasonable assumptions, the model's capability to capture the transient propagation of pressure within the system. At PRP2, I provide

evidence of the existence of elastic opening only. The numerical changes of fracture pressure at PRP2 are reproduced accurately. A greater variation in permeability of the fracture would have led to lower fracture pressure during the last two steps. By adequately incorporating this opening phenomenon into the model, I anticipate a less pronounced response in facture pressure to the injection. Consequently, the fracture pressure at PRP2 would have been diminished, aligning more closely with the site measurements. I demonstrated that the utilization of the radial diffusivity equation for a confined aquifer under semi-steady state condition equation results in a good agreement with the fracture pressure modeled for the first 4 steps, with higher deviation occurring during the last 2 steps.

The significance of hydromechanical interactions in the vicinity of a stimulation campaign is highlighted, which is of particular relevance for Enhanced Geothermal Systems (EGS). The proposed model effectively captures the behavior by integrating elastic and plastic responses that enhance permeability. The Equivalent Continuum Modeling approach enables a solution that can be replicated by engineers providing a realistic representation of the dynamics involved during such operations.

Chapter 4

Numerical Analysis of Far-Field Fault Reactivation Induced by Reservoir Cooling[c]

Abstract

This chapter presents thermo-hydro-mechanical framework to model hydrothermal systems within a simplified faulted synthetic reservoir, replicating current production scenarios in the Netherlands and Germany. The reservoir, composed of porous and permeable sandstone, and the confining layer, made of porous but less permeable shale, undergoes a process where cold water is injected and hot water is extracted. A fault, situated 750 meters from the injection well, is investigated to examine the conditions when fault slip could occur. Various fault and formation stiffnesses are modeled to assess their impact on fault stability. Our analysis reveals that stress changes induced by hydrothermal operations can lead to fault reactivation, with the stiffness contrast between the reservoir and confining layers playing a significant role in when and where fault reactivation can occur. Stiffer confining layers lead to reactivation occurring more closely associated with the passage of the cooling front. In contrast, a stiffer reservoir results in greater and more gradual stress changes, making reactivation more closely related to the total volume of cooled rock.

[c] This chapter has been published in Geothermics [Ouf et al., 2025].

4.1 Introduction

In hydrothermal systems, hot fluid is extracted at a production well, energy is then removed and the resulting colder fluid is reinjected via an injection well. This fluid circulation alters the initial pore pressure regime, impacting effective stress [Terzaghi, 1943, Skempton, 1954, Biot, 1955]. Injection and extraction of a fluid also induce deformation of the solid skeleton of the rock that leads to changes in stress [Geertsma, 1957a, Zimmerman, 1990]. As the cold fluid comes into contact with the hotter rock, the fluid absorbs energy from the rock, causing the rock to cool down [Tadmor et al., 2012, Zoback, 2010]. The introduction of colder fluid from the injection well therefore causes the progression of a cooling front, primarily driven by advection [Cathles, 1977, 1990]. This reservoir cooling leads to a change of stress and deformation within the reservoir [Geertsma, 1957b, McTigue, 1986]. The resulting stress change has implications for fault stability. Depending on the fault orientation, the normal effective stress may decrease while the tangential stress increases, leading to an overall increase in fault instability [Jaeger et al., 2009, Zoback, 2010].

Upon fluid injection or extraction, the initial pore pressure is disturbed. During injection, the pore pressure near the well increases, leading to a pressure gradient that causes water to diffuse away from the well [Zoback, 2010]. During extraction, the pore pressure near the well decreases, resulting in a pressure gradient that causes water to flow toward the well [Dake, 1983]. After fluid is injected or extracted from the rock matrix, the pore volume changes due to the (de)pressurized water occupying the pore space [Zimmerman, 1986, Chilingarian and Wolf, 1975]. The increase or decrease in volumetric stress caused by poroelastic effects progresses more extensively and rapidly compared to the spread of pore pressure during injection, as shown by e.g. Duboeuf et al. [2021], Krietsch et al. [2020], Boyet et al. [2023]. This poroelastic phenomenon, induced by fluid injection or extraction imposing tensile or compressive stress increments, has the potential to either enhance or diminish fault stability based on stress orientations [Segall and Lu, 2015, Zaal et al., 2021]. The advancement of the cooling

front in the reservoir exhibits less prominence in spatial distribution and is observed to propagate at a slower rate compared to the effects of poroelasticity and fluid propagation, as demonstrated by Jeanne et al. [2014], Blöcher et al. [2018].

Changes in pore pressure and temperature can affect the stability of faults [Geertsma, 1957b, Lord and Shulman, 1967]. This phenomenon can be illustrated by a Mohr-Coulomb failure envelope, where stress states are represented by Mohr's circle (see Fig. 4.1). Injection activities lead to an increase in fluid pressure [Dake, 1983]. Subsequent cooling of the reservoir causes contraction, reducing horizontal stresses due to geometric constraints, while vertical effective stress remains unaffected by thermal effects, offset by overburden pressure [Cryer, 1963, Mandel, 1953]. A fault nearing or reaching its failure threshold under stress conditions is considered critically stressed, indicating potential for seismic activity [Jaeger et al., 2009, McClure and Horne, 2014, Buijze et al., 2019]. Slip is predicted to arise when Mohr's circle is predicted to intersect or exceed the failure envelope, as shown in Fig. 4.1.

Seismicity has been observed to occur after pore pressures have stabilised, pointing to other triggering mechanisms such as the thermal effects [Kivi et al., 2022, Buijze et al., 2023]. Noteworthy events with magnitudes $M_L \geq 2$ in Unterhaching (Germany) were observed within a few months to three years after pore pressure stabilisation, suggesting cooling as a triggering factor [Megies and Wassermann, 2014]. Similarly, in Poing (Germany), two events with $M_L \geq 2$ occurred five years post-circulation commencement, indicating again cooling as a potential trigger as pore pressures would have been stable long before then [Seithel et al., 2019]. Moreover, in the Californië geothermal field in the Netherlands, cooling of the fractured carbonates reservoir induced events with a magnitude (M_L) of 1.7. This led to the suspension of the Dutch project due to concerns related to induced seismicity [Vörös and Baisch, 2022].

Numerical modeling can enhance the comprehension of the impact of stress changes within cooling reservoirs, arising from alterations in pore pressure and temperature [Rutqvist and Tsang, 2002, Rutqvist et al., 2013]. In a study conducted by Jacquey et al. [2015], the analysis of a synthetic case revealed that a fault situated between an injector and

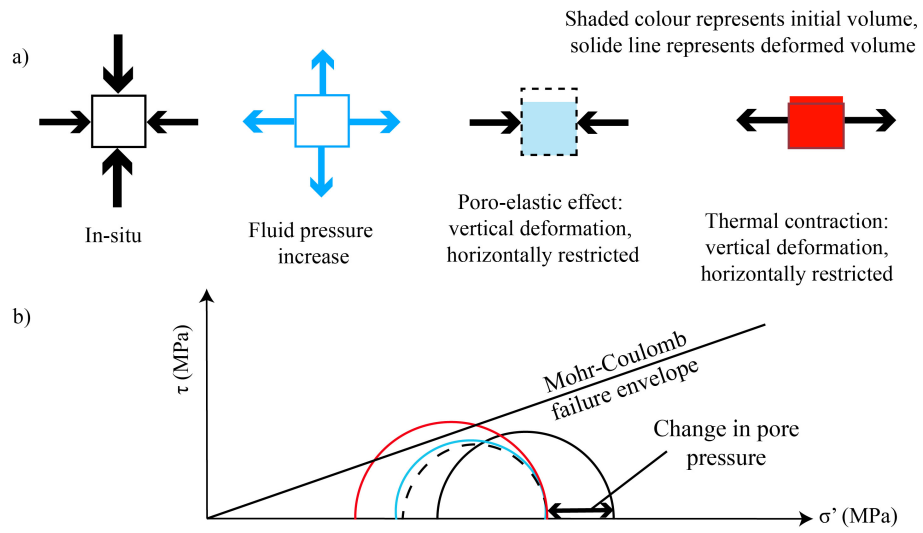


Figure 4.1: Diagram illustrating stress changes in a geothermal reservoir [Vardon, 2024] (Personal Communication): a) Components contributing to the final stress state; b) Mohr's circle and failure envelope demonstrating thermo-hydro-mechanical stress alterations. Line colors/types in (a) correspond to Mohr's circles in (b).

a producer well predominantly experiences slipping due to thermal effects rather than pore pressure effects. In a numerical poro-thermo-elasticity study conducted by Jacquey et al. [2016], the investigation focused on assessing the influence of pore pressure and temperature changes on the stability of the fault at the Groß Schönebeck geothermal site. The study underscored the significance of coupling these factors in numerical simulations [Jacquey et al., 2016]. Furthermore, in a 2D synthetic model, Kivi et al. [2022] demonstrated that faults located 1 km away from the injector and producer can undergo reactivation primarily due to thermal effects. In this scenario, the stress change at the fault was a result of reservoir contraction elsewhere in the system, as the cooling front does not reach the fault [Kivi et al., 2022].

From a modeling prespective, fractures can be implicitly represented using an equivalent porous media approach. Prominent codes that utilize this method include OpenGeoSys [Kolditz et al., 2012], the MOOSE framework [Permann et al., 2020], TOUGHFLAC [Itasca, 2011, Rutqvist, 2017], and CODE_BRIGHT [Gens et al., 1996]. Conversely, the explicit representation of fractures aims to realistically capture the geome-

try and impact of fractures, often requiring specialized treatment. Notable techniques for explicit fracture modeling include FEM-DEM/cohesive zone modeling [Lisjak et al., 2014, Grasselli et al., 2015], Discrete Fracture Network using interface elements [Gischig and Preisig, 2015], and Embedded lower-dimensional elements [Watanabe et al., 2012]. In this work, I use a continuous FEM approach, with a fracture zone that incorporate a zero-thickness element to replicate the fracture.

The current study aims to develop a numerical model for a synthetic geothermal project in a sandstone hydrothermal reservoir. The reservoir includes a fault zone located at 750m away from the injection point. The reservoir properties and the depiction of the heat extraction scenario draw inspiration from the comparative analysis presented in Buijze et al. [2023] and the Tiefe Geothermie 2023/24 project in Germany [Piesnack, 2023]. These detail current hydrothermal projects, including reservoir properties and injection scenarios, and discuss fault stability [Buijze et al., 2023, Piesnack, 2023]. Our modeling approach integrates a coupled poro-thermo-hydro-mechanics framework, including key couplings.

The critical parameters for fault reactivation need to be investigated to identify cases where faults are more prone to reactivation [Rutqvist et al., 2013, Kivi et al., 2022], and to investigate how reactivation evolves. To address this issue, this study investigates and quantifies the impact of fault, reservoir and caprock stiffness.

The primary focus is on investigating the potential reactivation of a fault situated 750 meters away from the injection well. The specific objectives include:

- Assessing the slip tendency of a fault located at a 750m away from the injection well.
- Investigating the triggering mechanism, considering poro-thermo-hydro-mechanics.
- Sensitivity analysis of the system by examining the effects of varying stiffness properties.
- Evaluating the propagation of ruptured area.

By addressing these objectives, our study seeks to provide an insight of fault behavior in a hydrothermal reservoir.

4.2 Modeling approach

4.2.1 Fully coupled numerical simulator

In our investigation, the PorousFlow and TensorMechanics modules within the MOOSE framework, developed by the Idaho National Laboratories, were used to construct our numerical model [Permann et al., 2020, Wilkins et al., 2020, 2021]. MOOSE makes use of advanced mesh libraries such as libMesh to enable parallel computations with adaptive mesh refinement (AMR) [Kirk et al., 2006]. It also leverages PETSc to achieve scalable solutions for scientific applications that involve partial differential equations in a parallel computing environment [Balay et al., 2017]. MOOSE framework, in conjunction with the GOLEM application [Cacace and Jacquey, 2017], was utilised by Jacquey et al. [2018] to simulate hydraulic stimulation at the Geothermal Site of Groß Schönebeck. Moreover, Sheldon et al. [2021] employed MOOSE with PorousFlow module to investigate the thermo-hydraulics of an aquifer thermal energy storage system. Additionally, Smith et al. [2022] utilized MOOSE with PorousFlow module to calculate permeability of fractures and its implications for geothermal fluid flow and the influence of seismic-scale faults.

4.2.2 Coupled thermo-hydro-mechanical equations

Mechanical formulation

The momentum balance, neglecting inertial effects, can be written as:

$$\nabla \cdot \boldsymbol{\sigma'} - \rho g = 0 \tag{4.1}$$

where $\boldsymbol{\sigma'}$ is the effective stress tensor, ρ the density and g the acceleration.

The effective stress $\boldsymbol{\sigma'}$ in Eq. 4.1, incorporating both hydraulic and thermal components (differently from Chapters 2 and 3), can be calculated as follows:

$$\Delta\boldsymbol{\sigma'} = \mathbb{C} : \Delta(\boldsymbol{\varepsilon_{mechanical}} - \boldsymbol{\varepsilon_{thermal}}) - \alpha_b \Delta p_f \boldsymbol{I} \tag{4.2}$$

where $\mathbb{C}$ is a tensor incorporating the constitutive behaviour, $\boldsymbol{\varepsilon}$ is the strain tensor (small strain assumption), α_b is the Biot coefficient, p_f is the pore pressure and $\boldsymbol{I}$ is the identity tensor.

The remaining part of the mechanical theory, i.e. the part relating to yield and plasticity is presented in Section 2.2.2. Softening is not modeled in this chapter.

Hydraulic formulation

The same formulation as Chapter 2 is used for this model. Fracture aperture stays constant.

Thermal formulation

The equation for the energy balance of in a porous medium is:

$$\frac{\partial \boldsymbol{\xi}}{\partial t} + \boldsymbol{\xi}\frac{\partial \varepsilon_{vol}}{\partial t} = -\nabla \cdot \boldsymbol{F}^T + q^T \tag{4.3}$$

where ε_{vol} is the volumetric strain of the bulk, $\boldsymbol{\xi}$ is the thermal energy per unit volume in the rock-fluid system, $\boldsymbol{F}^T$ the heat flux, q^T the heat forcing term (injection/production).

The thermal energy per unit volume in the rock-fluid system, $\boldsymbol{\xi}$ in Eq. 4.3 is expressed as:

$$\boldsymbol{\xi} = (1-n)\rho_r C_r T + n\rho_f C_f T \tag{4.4}$$

where ρ_r is the density of the rock, C_r is the volumetric heat capacity of the rock, T temperature, ρ_f density of the fluid, C_f volumetric heat capacity of the fluid.

The heat flux equation in Eq. 4.5 is as follow:

$$\boldsymbol{F}^T = \boldsymbol{q}_f h + \lambda \nabla T \tag{4.5}$$

where h is the enthalpy of the liquid phase and λ is the thermal conductivity, the bulk thermal conductivity is three times the linear thermal conductivity.

4.2.3 Model Set up

The domain, measuring 6500m x 6500m x 800m, encompasses the fracture zone, reservoir, and confining layer, as illustrated in Fig. 4.2. The model includes two confining layers, each 300 meters thick, which confine a 200 meter thick reservoir. A fault is included in the model, and is represented by a zero-thickness element within a 20 m-wide fault zone. This fault is inclined at a 60° angle between the Z and X axes and has an offset of 30 m. The center of the fault is positioned at the X coordinate of 2590 m and the fault runs parallel to the Y axis (Fig. 4.2). The injection well is located at a distance of 750 meters along the X coordinate from the fault and Y = 3250 m. This well is modeled as a 1D line with a length of 180 m perpendicular to the Z axis, with the lowest point being 10 m from the bottom of the reservoir. The production well is situated 1600 m away from the injection well. As for the injection well, it is modeled as a 1D line, 180 m in length in the direction of the Z axis, and again the lowest point is 10 m from the reservoir's bottom. The well to well distance aims to prevent rapid thermal breakthrough and maximize the project's lifespan. In all simulations, a constant injection and flow rate of 150 l/s was utilised, with the fluid introduced at a temperature of 30°C. The producer extracts fluid at a flow rate of 150 l/s and a temperature of 134°C. Around 50 years of production is simulated. This scenario is typical of Dutch and German projects [Buijze et al., 2019, Piesnack, 2023]. This chapter presents models of four different scenarios, each representing varying levels of stiffnesses for different materials in the domain. Detailed material properties can be found in Tables 4.1,4.2

and 4.3.

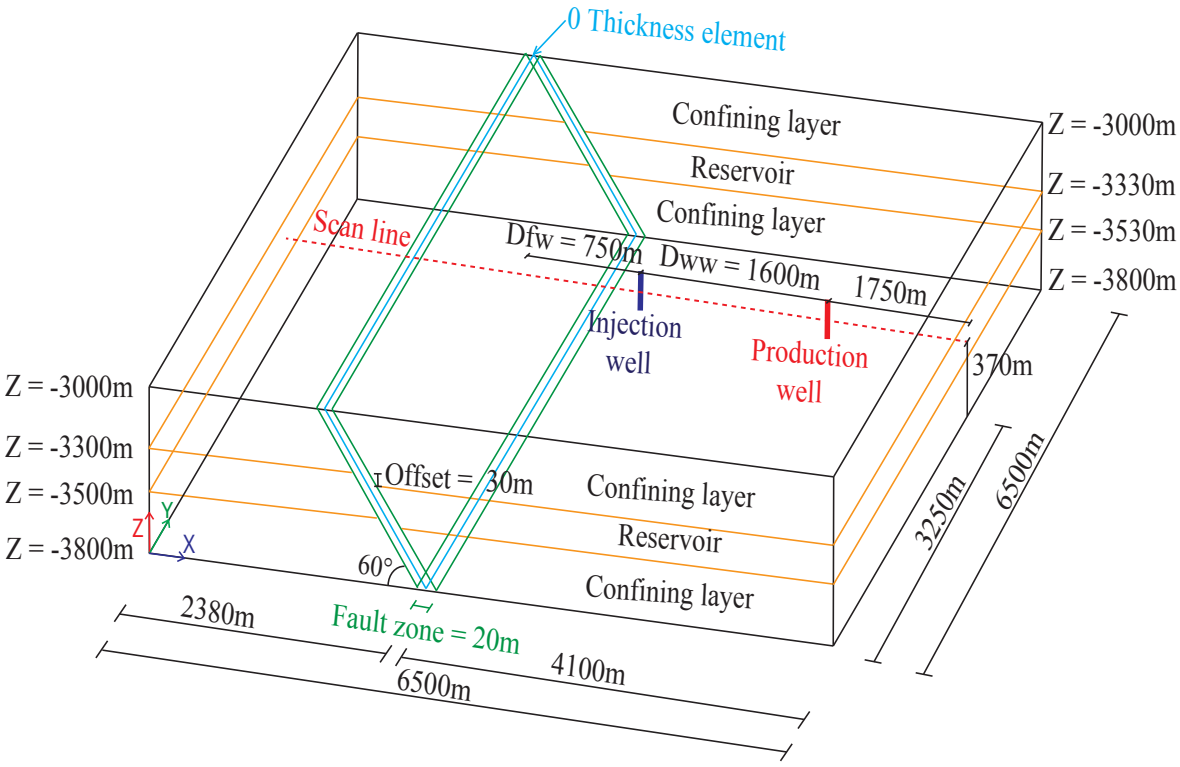


Figure 4.2: Model domain and geometry

The reservoir is considered to be composed of sandstone and characterized by properties inspired by Buijze et al. [2023]. Hydraulically, the reservoir is considered to be a permeable porous medium, governed by Darcy's law. The thermal aspect encompasses conduction and fluid heat advection. Mechanically, the sandstone reservoir is considered to adhere to Hooke's law, i.e. it is perfectly linearly elastic. The confining layer represents a shale, which is a porous medium with low permeability, that follows Darcy's law, and thermal behaviour considers both conduction and fluid advection. Mechanically, the confining layers are linear elastic, i.e. adhere to Hooke's law. The fault zone is modelled with the Mohr-Coulomb constitutive model (Eqs. 2.4 and 2.5). The relevant properties are detailed in Table 4.1, which were chosen to be representative of field conditions [Buijze et al., 2023]. The fault zone hydraulically is modeled as a 2D element embedded in a 3D permeable porous medium, governed by Darcy's law,

with heat transport again including both conduction and fluid advection. Within this fault zone, a zero-thickness element (2D) is employed to allow the influence of a realistic fault aperture on the hydraulic properties. The permeability for the zero-thickness element is represented by an equivalent transmissivity, calculated as: $T = k \cdot a$, k represents the permeability of the fault (m^2), a signifies the fault aperture (m). The transmissivity T has units of (m^3) (or equivalently $m^2 \cdot m$), reflecting the product of permeability and aperture. Similarly, the porosity is expressed as a 3D equivalent, denoted as $n_{0thickness} = n \cdot a$, where a is the fault aperture, and n represents the fault porosity. A constant aperture has been assumed, set at 1.1 micrometers. Consequently, $T_{0thickness}$ equals $1.1 \cdot 10^{-19}$ m^3, and $n_{0thickness}$ equals $8.25 \cdot 10^{-5}$m. The fault is considered with transverse and longitudinal properties being the same. This method guarantees that the lower-dimensional fracture elements are connected to the porous matrix elements, which represent the fault zone. By employing fully-implicit time-stepping with PorousFlow's complete Jacobian, I enhance numerical performance [Permann et al., 2020]. The mechanical properties are incorporated directly into the fault zone, while the thermal-hydraulics are accounted for within both the zero-thickness elements and the fault zone. Other properties of the fault zone are chosen to match the reservoir.

The model's initial temperature is set at 134 °C, based on a calculated gradient of 35 °C/km and a surface temperature of 15 °C. Considering that the center of the reservoir is located at a depth of -3.4 km. This temperature is uniformly applied throughout the model, as depicted in Fig. 4.3. All the thermal boundary conditions are fixed at 134 °C. The hydraulic initial condition is characterized by a hydrostatic pressure gradient assuming pure water, ranging from 30 MPa at the top to 38 MPa at the bottom, with the boundary conditions maintaining this gradient.

The initial vertical (Z-direction) stress at the top of the domain is set as $\sigma_{zz} = 75$ MPa, corresponding to a 3 km overburden with a density of 2500 kg/m^3. The initial stress σ_{zz}, exhibits a gradient of 25 MPa/km across the entire domain. The initial major horizontal stress (Y-direction) is the intermediate stress, set as $\sigma_{yy} = 61.5$ MPa at the top, with a gradient of 20.5 MPa/km depth. The initial stress in the X-direction is the

Table 4.1: Thermal, hydraulic and mechanical properties of the rock. Properties are based on Buijze et al. [2023]

Parameters	Unit	Reservoir	Confining layer	Fault zone
Rock properties				
Biot coefficient (α_b)	-	1	1	1
Young modulus (E)	GPa	Table 4.3	Table 4.3	Table 4.3
Poisson's ratio (ν)	-	0.33	0.3	0.3
Density (ρ_r)	kg/m^3	2500	2500	2500
Porosity (n)	%	25	20	75
Permeability (k)	m^2	10^{-13}	10^{-19}	10^{-13}
Thermal conductivity (λ)	W/(m·K)	2.5	2.5	2.5
Specific heat capacity (C_r)	J/(kg·K)	1200	1200	1200
Linear thermal expansion coefficient (α_{rl})	-	$3{\cdot}10^{-5}$	$3{\cdot}10^{-5}$	$3{\cdot}10^{-5}$
Cohesion (c)	MPa	-	-	0
Friction angle (ϕ)	°	-	-	30
Dilation angle (ψ)	°	-	-	2

Table 4.2: Fluid properties of the model. Properties from International Association for the Properties of Water and Steam Wagner and Pruß [2002]

Parameters	
Density (ρ_f)	1000 kg/m^3
Viscosity (μ_f)	10^{-9} MPa·s
Bulk modulus (K_f)	2 GPa
Thermal conductivity (λ_f)	0.6 W/(m·K)
Linear thermal expansion coefficient (α_{fl})	$2.14{\cdot}10^{-4}$ (K^{-1})
Specific heat capacity (C_f)	4000 (J/kg·K)

minor stress σ_{xx}, which is set at 52.5 MPa at the top, with a stress gradient of 17.3 MPa/km along the Z-direction. This latter value was determined via elastic theory $\sigma'_{hmin}/\sigma'_v = \sigma'_{xx}/\sigma'_{zz} = (\nu/(1-\nu))$ [Eaton, 1969], therefore not considering tectonic changes, and is therefore suitable only for exploratory analyses. The mechanical top boundary condition is defined by $\sigma_{zz} = 75$ MPa, and the bottom boundary condition

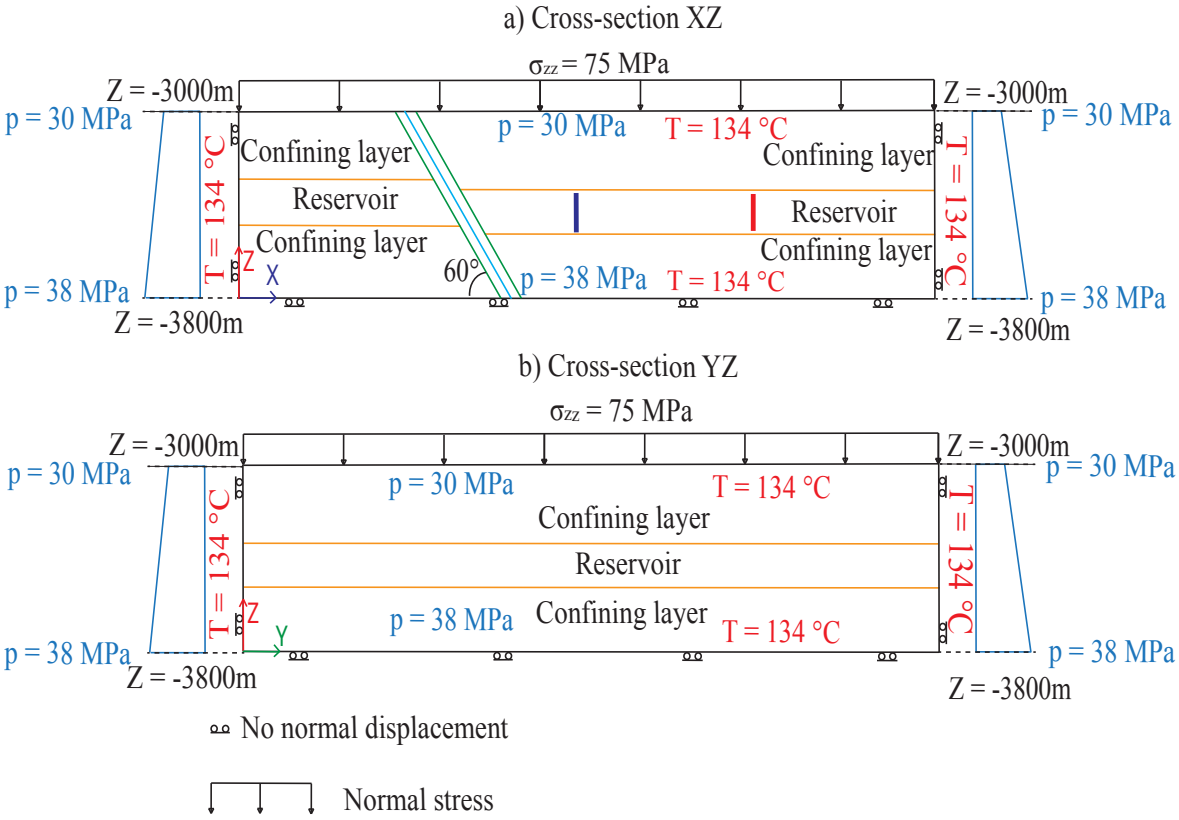


Figure 4.3: Boundary conditions of the model (locations of the cross-sections refer to Fig. 2 at the center-point of the Y and X axes of the domain, respectively): a) Cross-section XZ , b) Cross-section YZ.

is set to having no normal displacement in the Z-direction and is free to move in the other directions. The Y- and X-direction boundary conditions are also set to have no normal displacement and are free in the other directions (see Fig. 4.3).

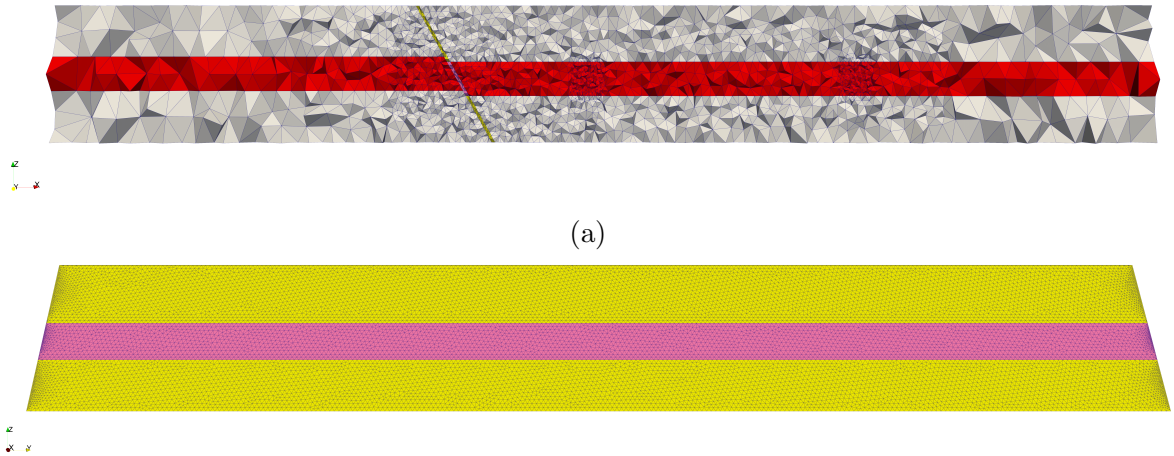
Table 4.3: Parameters of the different scenarios modeled. Properties are based on Buijze et al. [2023]

Scenario	E_{Fault}	$E_{Reservoir}$	E_{Conf}
1	4 MPa	7 MPa	20 MPa
2	7 MPa	7 MPa	20 MPa
3	4 MPa	20 MPa	7 MPa
4	7 MPa	20 MPa	7 MPa

In this configuration, the stress regime on the fault is characterized as a normal fault [Zoback et al., 2003, Jaeger et al., 2009]. A normal fault regime is typical in many deep

geothermal projects, such as the Groß Schönebeck (DE), Essen (DE), Poeldijk (NL) and de Lier (NL) [Moeck et al., 2009b, Buijze et al., 2019].

The model is assumed to be fully saturated and gravity is taken into account. However, changes in fluid properties, which depend on water pressure and temperature are not incorporated into the model, with the fixed values found in Table 4.2. This was chosen as the details of, for example, bouyancy driven flow are thought to be of secondary importance for fault reactivation. Changes in fault permeability due to the evolution of aperture are not modeled. The model used 171 820 nodes and 972 427 tetrahedral elements. The mesh has been refined at the locations of the wells, on the fault and between the fault and the injection well, as shown in Fig. 4.4. Prior to injection, the model is in hydraulic, thermal and mechanical equilibrium. Variations in (comparative) stiffnesses were investigated, as shown in Table 4.3. These values are typical for Dutch projects [Buijze et al., 2023].



(a)

(b)

Figure 4.4: Nodes and meshes: a) Reservoir cross section, b) Fault

4.2.4 Slip Tendency

Slip tendency is a quantification of how close a material is to slipping. It is defined as the ratio of shear stress to normal effective stress [Morris et al., 1996]. This equation

is a linearised Mohr–Coulomb relationship, i.e., not taking into account any cohesion, which can be defined as:

$$ST = \frac{\tau}{\sigma'_n} \leq tan(\phi) \tag{4.6}$$

where τ is the shear stress acting on the fault, σ'_n the normal effective stress acting on the fault and ϕ the friction angle.

If the slip tendency ratio is equal to $tan(\phi)$, and the fault does not have cohesion, then the fault is considered to be slipping. Here, a friction angle of 30° has been assumed to be indicative of a typical fault [Healy et al., 1984, Zoback, 2010].

4.2.5 Limitations

It is important to note that the transition from fault slippage to seismic activity is not accounted for. To achieve this, calculating the seismic moment tensor and employing more advanced constitutive models are necessary. These models would allow for the accumulation of strain energy, which could be released during specific events, leading to an uncertain frequency or magnitude of such occurrences. Additionally, incorporating changes in fluid properties with temperature would improve the accuracy of the scenarios, particularly for site-specific analyses. However, the simulations presented here depict a hypothetical geothermal exploitation scenario, and have been simplified to enhance the interpretation.

4.3 Results

In a uniform elastic medium, thermo-elastic stress predominantly relies on the Young's modulus and the linear thermal expansion coefficient, coupled with temperature changes [Soltanzadeh and Hawkes, 2009a,b]. Hence, the investigation is made with different Young's moduli for the fault zone, reservoir and confining layers (see Table 4.3). This choice aims to explore how varying stiffness affects stress variation and the ruptured area of the fault within a nonhomogeneous thermo-poro-elasto-plastic model.

4.3.1 Reservoir pore pressure and temperature

Cold water injection and water extraction significantly influence the pore pressure and temperature fields within the reservoir. In Fig. 4.5, the evolution of pore pressure and temperature in the reservoir along the scan line of Fig. 4.2 over different time intervals is presented. As fluid circulates, the pore pressure increases near the injector and decreases near the producer, stabilizing after one year. The pore pressure profile at 1 year and 55 years is virtually identical, indicating that the system reaches equilibrium after a year of injection. Although minor changes in pore pressure might continue if permeability is assumed to change with porosity, the overall effect of injection and extraction is a stable pore pressure distribution over time. This highlights the system's tendency to equilibrate, with long-term stability in pore pressure despite the initial perturbations (see Fig. 4.5a).

The non-linear pore pressure spatial gradients are due to the radial flow away and towards the wells. The magnitude of variation in pore pressure at the wells aligns consistently with on-site measurements from Dutch geothermal projects, as documented by Buijze et al. [2023].

As fluid circulates, the temperature around the injector decreases. Fig. 4.5b illustrates the temperature variation within the model at different time intervals. Initially, when at rest, the temperature is at 134°C. As fluid circulates, the temperature around the injector decreases. After 1 year, the temperature immediately around the injector drops to 30°C, with a cooling diameter of approximately 500 m. After 10 years, the cooling radius extends to 1230 m. The cooling front makes direct contact with the fault after 27.5 years of production. By the 55th year, the diameter reaches approximately 2415 m. The cooling front advances more rapidly towards the producer (right side of the figure) from the injector, seen most clearly in the later stages of the analysis. The current design does not have thermal breakthrough in the investigated time.

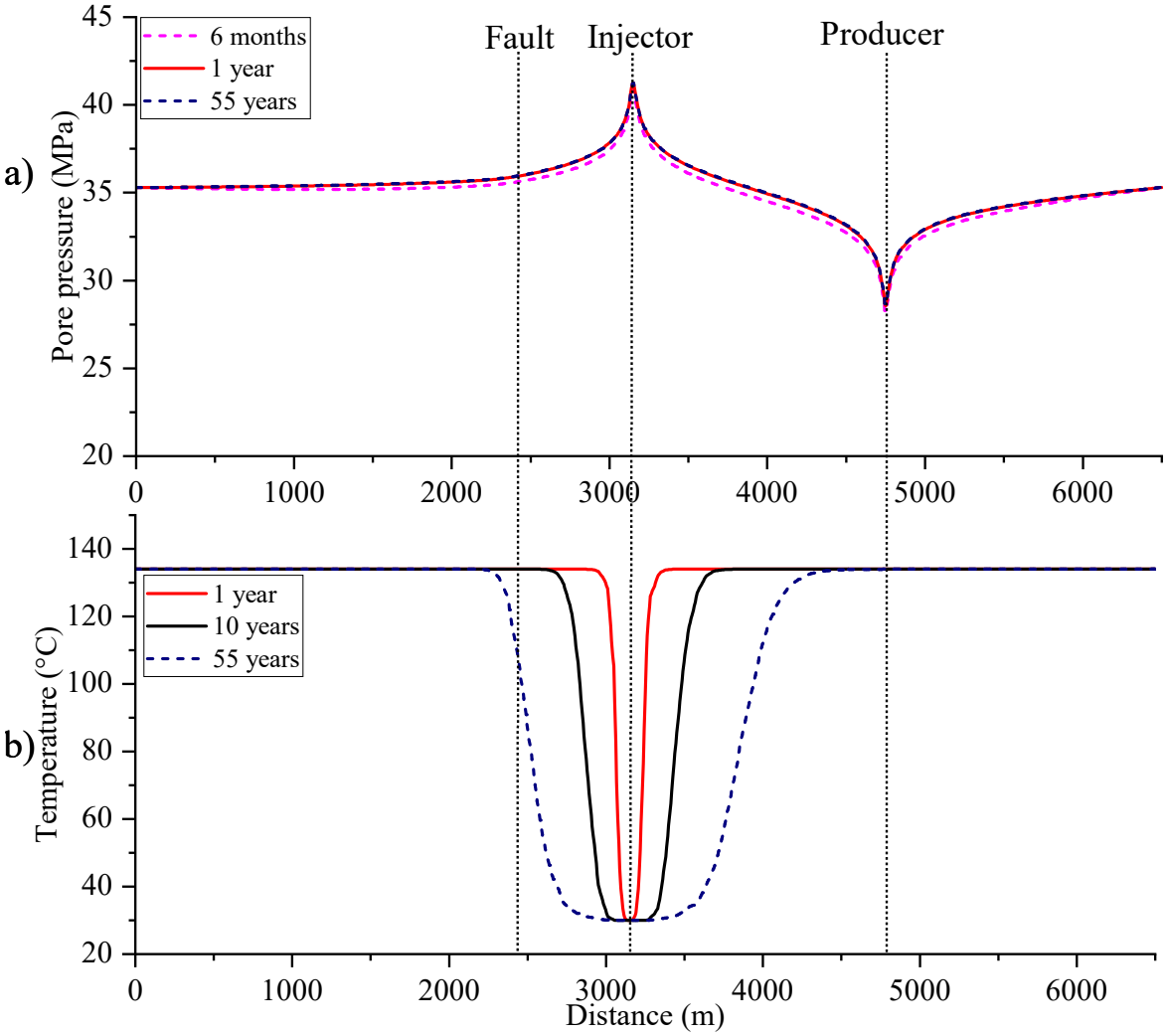
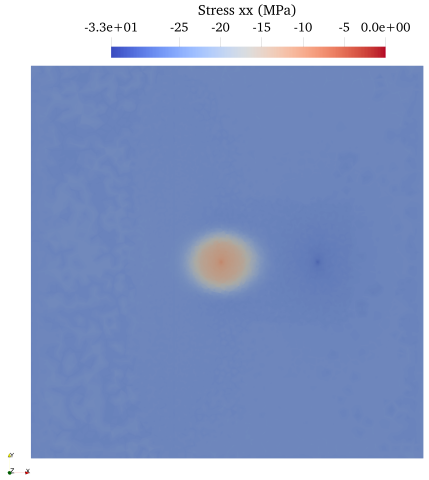


Figure 4.5: Distribution inside the reservoir of a) Pore pressure, b) Temperature.Distance is along the scan line in figure 4.2

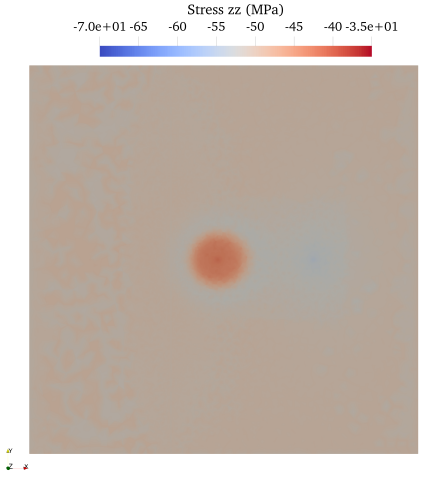
4.3.2 Stress changes within the reservoir

The perturbation of pore pressure and temperature impacts the fault stress field, with varying effects depending on the reservoir stiffness. As shown in Fig. 4.6, stress around the injection wells decreases, while stress near the production wells increases, although to a smaller degree. In stiffer reservoirs, stress redistribution leads to greater destressing around the injection site. The horizontal stress perturbation is more elliptical, with the most significant reservoir distress occurring along the x-axis than the z-axis (see

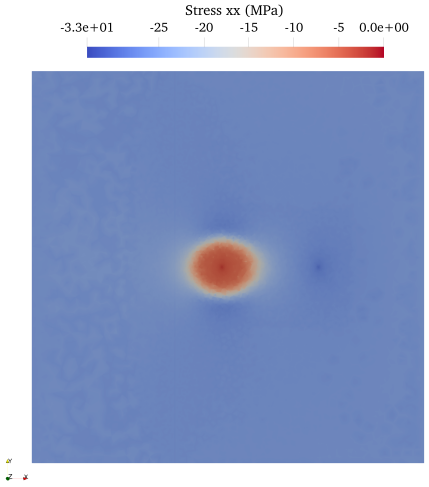
Fig. 4.6). These findings highlight the importance of reservoir stiffness in influencing the stress distribution and fault behavior during injection and production processes.



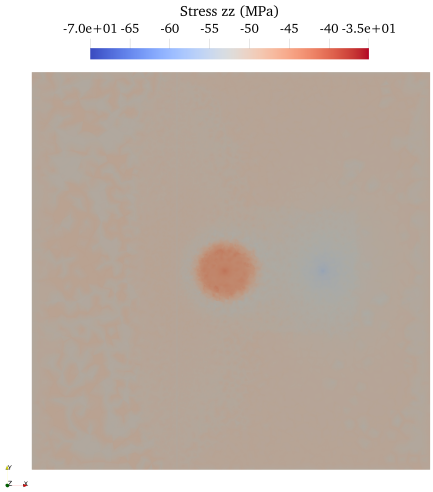
(a) σ'_{xx} - Scenario 1



(b) σ'_{zz} - Scenario 1



(c) σ'_{xx} - Scenario 3



(d) σ'_{zz} - Scenario 3

Figure 4.6: Plan view of stresses at the center of the reservoir after 27.5 years of injection a) σ'_{xx} - Scenario 1 b) σ'_{zz} - Scenario 1 c) σ'_{xx} - Scenario 3 d) σ'_{zz} - Scenario 3

4.3.3 Stress changes at the fault

The changes in the stress field within the reservoir have a direct impact on the local fault stress. The local changes in temperature, pore pressure, and stress are depicted

in Fig. 4.7. The evolution of pore pressure and temperature at the center point of the fault is depicted in Fig. 4.7a. The pore pressure exhibits a stabilisation after one year of injection (from 35.3 MPa to 36.06 MPa).

The temperature of the fault (see Fig. 4.7a) begins at an initial temperature of 134°C. After around 27.5 years of injection, the cold front reaches the fault, causing the temperature to sharply decrease. The smooth, but accelerating, reduction in temperature is due to the thermal conductivity reducing the severity of the thermal front. After 49.13 years of production, the initial patch undergoes reactivation, coinciding with a temperature of 117.5°C at that time. Upon completion of the simulation, the center of the fault's temperature has reduced to 110°C.

The contrasting behaviors highlight the critical role of stiffness. Higher reservoir stiffness increases fault reactivation and increases the rate of tangential stress accumulation (as shown in Fig. 4.7). Cooling further accelerates failure in Scenarios 3 and 4, demonstrating that thermal effects can significantly alter fault stability when coupled with poroelastic stress changes. The tangential shear stress acting on the fault evolves due to the interplay between cooling, pore pressure changes, and stiffness. As shown in Fig. 4.7b, the initial shear stress on the fault is 11.5 MPa. Over time, the stress evolution varies significantly between scenarios. In Scenarios 1 and 2, the shear stress increases throughout the simulation, reaching 13.38 MPa and 13.56 MPa, respectively, after 55 years of injection. The larger fault stiffness in Scenario 2 leads to a higher rate of stress increase compared to Scenario 1. In contrast, Scenarios 3 and 4 show fault failure due to cooling effects and lower stiffness. Scenario 3 reaches a peak stress of 14.73 MPa after 51.2 years, while Scenario 4 reaches 14.85 MPa after 49 years. Post-failure, both scenarios exhibit a reduction in stress due to stress redistribution and sliding along the failure plane.

The observed variations underscore the impact of material stiffness. Lower reservoir stiffness amplifies stress redistribution, accelerating fault instability. Conversely, stiffer confining layer exhibit more gradual stress changes, delaying fault reactivation. Effective normal stress, which governs fault stability, is also influenced by pore pressure and

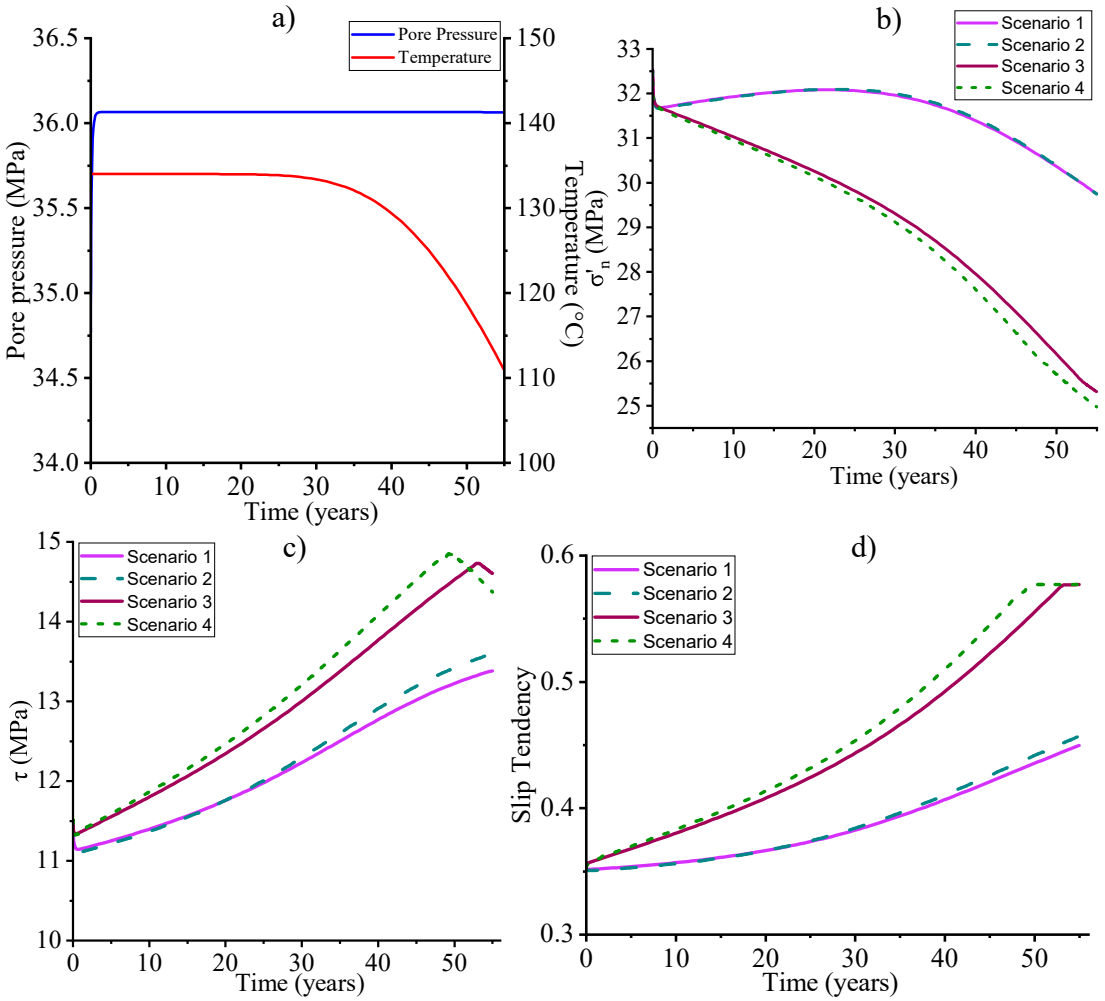
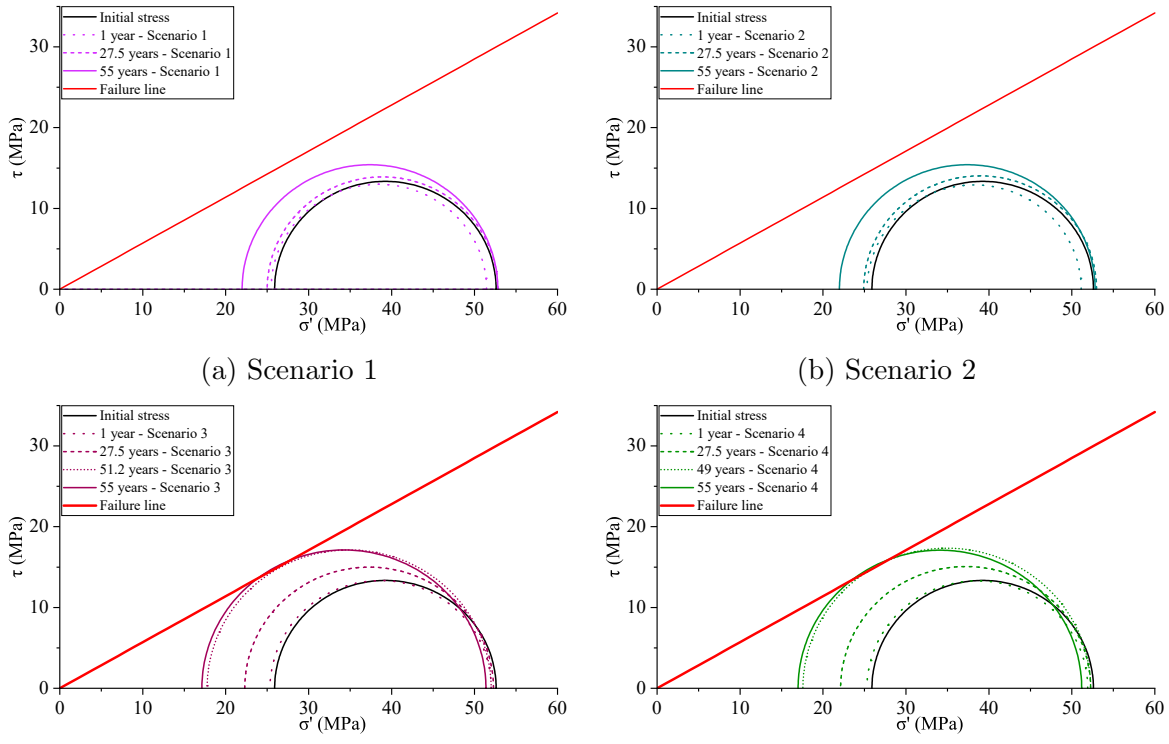


Figure 4.7: a) Temperature and pore pressure at middle of the fault b) Tangential shear stress acting on the middle of the c) Normal effective stress acting on the middle of the fault d) Fault Slip Tendency Evolution

temperature changes (Fig. 4.7c). Initially, the normal effective stress is 32.5 MPa, but injection-induced changes vary across scenarios. In Scenarios 1 and 2, effective normal stress reduces and then increases slightly during the first 27.5 years due to poroelastic effects, reaching 32.1 MPa, before decreasing to 29.8 MPa after 55 years as cooling effects dominate. In Scenarios 3 and 4, the normal effective stress decreases steadily to 29.61 MPa and 29.43 MPa, respectively, after 27.5 years, and further declines to 25.31 MPa and 24.97 MPa at the end of the simulation. Cooling fronts and stiffness contrasts exacerbate stress reduction, leading to earlier reactivation in these scenarios.

Slip tendency results indicate that systems with lower confining layer stiffness are more prone to instability, due to the clamping effect of the confining layer. Monitoring slip tendency evolution can serve as an early warning for fault reactivation during geothermal operations. Slip tendency, defined as the ratio of tangential shear stress to effective normal stress, evolves with injection and cooling (Fig. 4.7d). In Scenarios 1 and 2, the slip tendency increases gradually, reaching 0.445 and 0.457 after 55 years. Faults remain stable throughout the simulation due to limited reductions in effective normal stress and moderate increases in shear stress. In Scenarios 3 and 4, slip tendency increases monotonically, eventually reaching the critical value of 0.577. Failure occurs at 51.2 years in Scenario 3 and 49 years in Scenario 4. The acceleration of slip tendency is driven by the combined effects of cooling and reduced stiffness, which amplify stress perturbations.



(a) Scenario 1

(b) Scenario 2

(c) Scenario 3

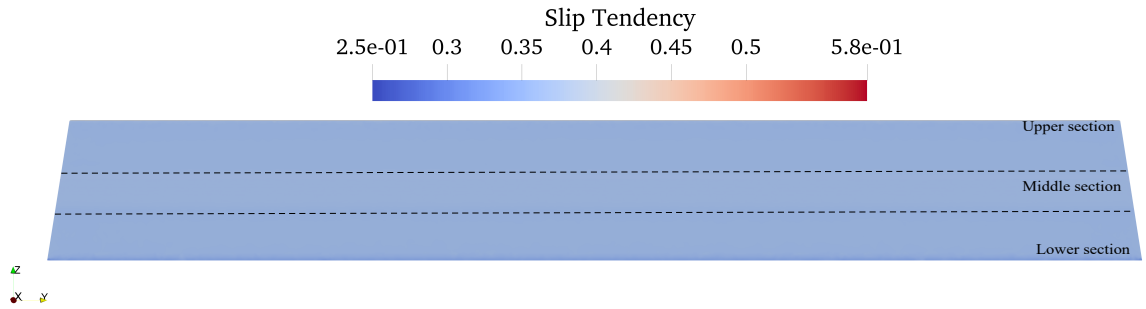
(d) Scenario 4

Figure 4.8: Representation of effective stress evolution at the middle of the fault at Z = -3470m with Mohr's Circles; a) Scenario 1, b) Scenario 2, c) Scenario 3, d) Scenario 4

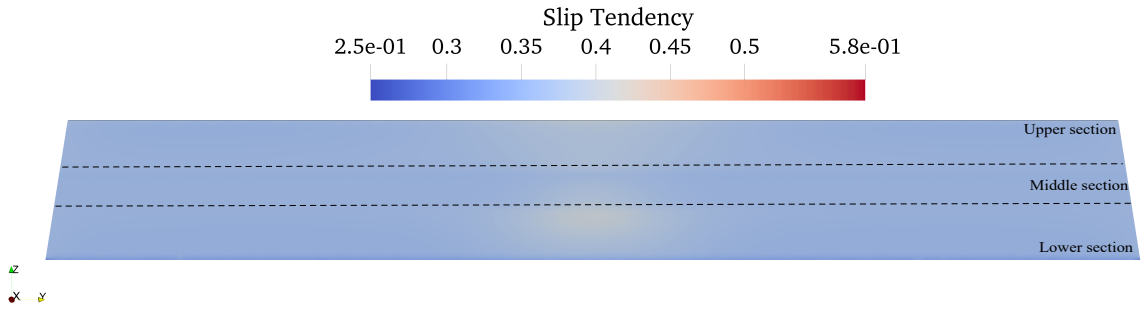
Poroelastic effects lead to reductions in minor stress, while cooling causes further expansion of the Mohr's circle, particularly affecting minor stress as explained in Fig. 4.1b. These effects, combined with changes in stress distributions, ultimately lead to fault reactivation in scenarios 3 and 4, as the minor stress reaches critical levels required for failure. During different stress perturbation regimes in the reservoir, fault stress experiences significant changes. Fig. 4.8a and 4.8b illustrate the stress state at the center of the fault at a depth of Z = -3470 m for Scenarios 1 and 2, where the Mohr's circle initially shows major and minor stresses. As fluid is extracted and injected, the Mohr's circle moves laterally without changing size due to increased fluid pressure, which isotropically affects the effective stress. However, due to the poroelastic effect and horizontal movement restrictions, the circle reduces in size. Cooling further causes the Mohr's circle to expand due to volumetric changes restrained by horizontal stress within the reservoir. The effects of stress perturbations over time vary across different scenarios. After 1 year, the major and minor stresses decrease, with Scenario 1 showing a larger decrease in the major stress compared to Scenario 2 as shown in 4.8a and b. After 27.5 years, both scenarios show a decrease in minor stress, but the major stress increases in both cases. At the end of the simulation, further cooling leads to a substantial reduction in minor stress, while the major stress remains largely unchanged. The stiffness of the reservoir and confining layer plays a key role in how stress is distributed. In Scenarios 3 and 4, the poroelastic effect has a lower impact on major stress due to the lower stiffness of the overburden, leading to less stress arching. After 1 year of production, both scenarios show a decrease in minor and major stresses, with Scenario 4 showing slightly larger reductions than Scenario 3. Over time, the cooling process increases the diameter of the Mohr's circle, primarily affecting minor stress as the volume of cooled rock expands. As the fault reaches the failure line, the Mohr's circle slides along it, perturbing both major and minor stresses. By the end of the simulation, further changes in stress are observed, with a notable decrease in both major and minor stresses in both scenarios as shown in Fig. 4.8.

Figure 4.9 illustrates the evolution of slip tendency across the fault zone. Slip ten-

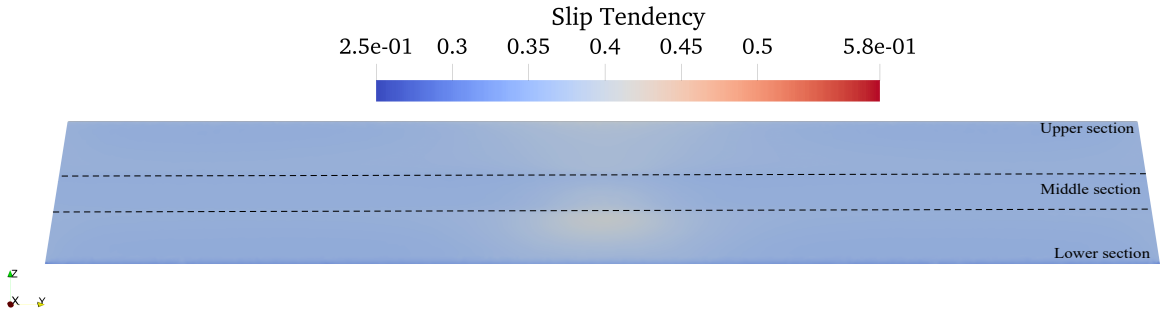
dency evolves over time due to variations in pore pressure and temperature, leading to different spatial distributions across the fault depending on the stiffness scenarios. Initially, the slip tendency is uniform along the fault, but after 27.5 years of operation, areas at the top and bottom of the fault show increased slip tendency, indicating reduced stability (see Fig. 4.9). In contrast, the central section remains stable until the cold front reaches it. Over the course of the 55 year simulation, the instability in the central and outer sections of the fault continues to evolve, with the fault becoming progressively more unstable, particularly in the middle section, where the cold plume impacts the fault. These changes highlight how fault stability is influenced by thermal and pressure perturbations, with significant variations between the different stiffness scenarios as shown in Fig. 4.9.



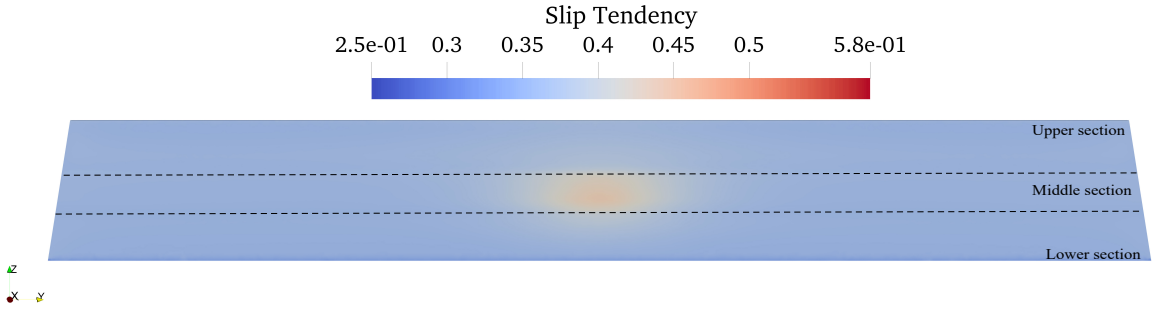
(a) Initial Condition



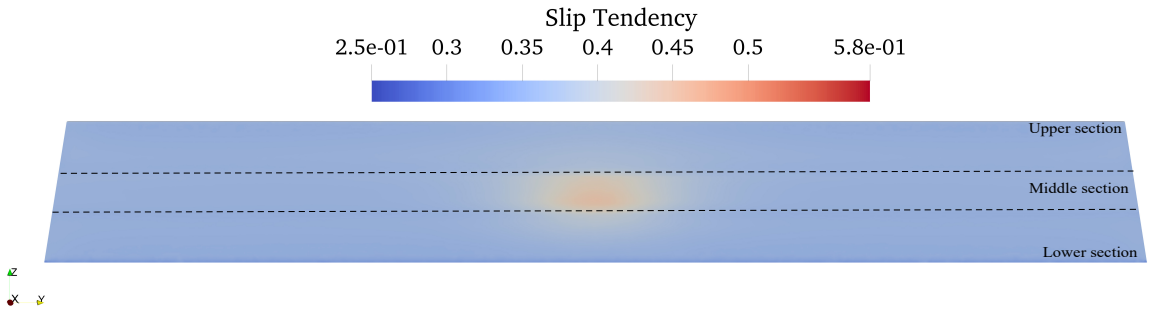
(b) Scenario 1 - 27.5 years production



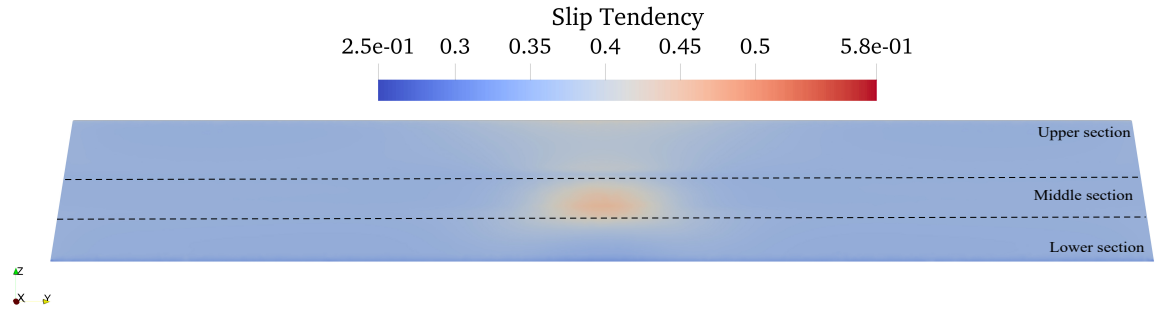
(c) Scenario 2 - 27.5 years production



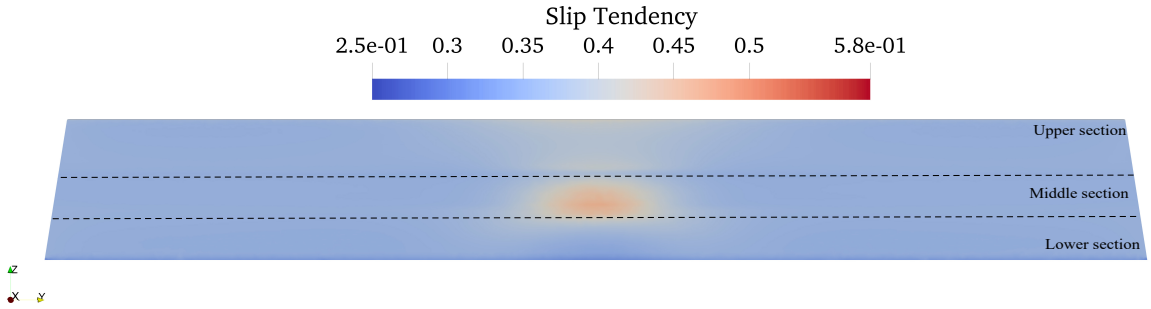
(d) Scenario 3 - 27.5 years production



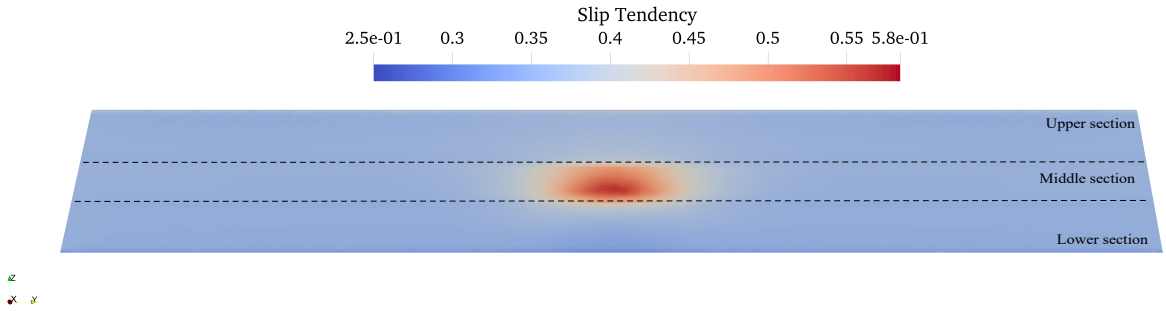
(e) Scenario 4 - 27.5 years production



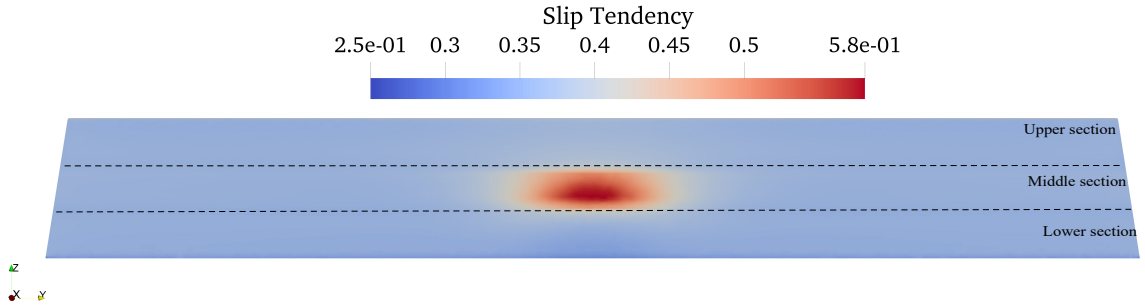
(f) Scenario 1 - 55 years production



(g) Scenario 2 - 55 years production



(h) Scenario 3 - 55 years production



(i) Scenario 4 - 55 years production

Figure 4.9: Fault slip tendency: a) Initial Condition b) Scenario 1 - 27.5 years production c) Scenario 2 - 27.5 years production d) Scenario 3 - 27.5 years production e) Scenario 4 - 27.5 years production f) Scenario 1 - 55 years production g) Scenario 2 - 55 years production h) Scenario 3 - 55 years production i) Scenario 4 - 55 years production

Fig. 4.10 illustrates the evolution of the ruptured area of the fault over time for different stiffness scenarios. Reactivation occurs at different points for scenarios 3 and 4, with scenario 4 showing reactivation at 49 years and scenario 3 at 51.2 years. Both exhibit a bi-linear evolution of the ruptured area over time, with inflection points at 50.8 years for scenario 3 and 53.75 years for scenario 4. Scenario 4 experiences a much larger maximum ruptured area compared to scenario 3, indicating a greater degree of fault reactivation under higher stiffness conditions. These findings highlight the sensitivity of fault reactivation to changes in stiffness, with scenario 4 being more prone to significant ruptures.

This value for the ruptured area aligns with findings from other studies on fault reactivation during geothermal operations [Boyet et al., 2023, Kruszewski et al., 2023]. Specifically, Boyet et al. [2023] reported a ruptured area ranging from 846 to 14236 m^2, while Kruszewski et al. [2023] observed values between 8000 and 22000 m^2.

It is seen that the stiffness of the fault results in small changes in the re-activation time, and then a stiffer fault (scenario 4) results in a slower progression of the rupture area - the rate being approximately 50% lower.

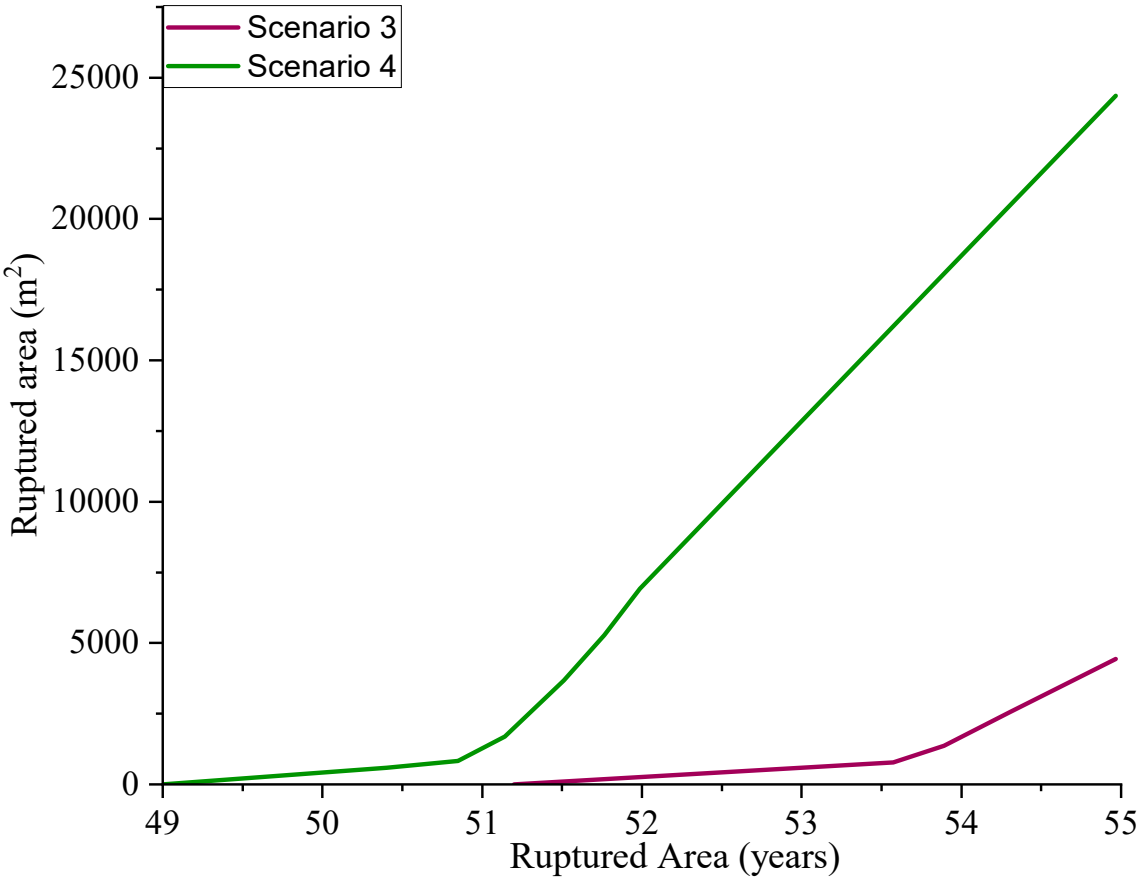


Figure 4.10: Ruptured area of the fault for different fault stiffness

4.4 Discussion

4.4.1 Fault reactivation

Over time, it is observed that different mechanisms contribute to fault reactivation:

- Mechanism 1: Poroelastic response following injection causes the reservoir to expand, resulting in fault contraction.
- Mechanism 2: Changes in water circulation affect pore pressure due to injection.
- Mechanism 3: Reservoir cooling induces reservoir contraction, thereby causing fault expansion.

- Mechanism 4: Cold fronts reaching the fault perturb the stress regime in the fault.

These mechanisms have different dominance over time. Mechanisms 1 and 2 disturbed the stress regime early in the models, while mechanisms 3 and 4 disturbed it more significantly later in the models. The observation that pore pressure stabilizes on a monthly scale while fault reactivation occurs after several years of production indicates that the primary mechanisms driving reactivation are cooling and the percolation of cold fronts (Mechanisms 3 and 4).

The contrast in confining layer and reservoir stiffness plays a key role into how local the horizontal stress changes in the reservoir and confining layers are, and therefore also in the fault where these layers are intersected. When the reservoir is cooled, a thermally induced shrinkage occurs, and due to the overall horizontal constraint (i.e. at the model boundaries), the horizontal stress reduces. In scenarios 1 and 2, the stiff confining layer ensures that the stress changes are more local and do not propagate throughout the reservoir. In scenarios 3 and 4, the stiff reservoir is less easily constrained by the confining layers and the reduction in horizontal stress is able to more easily spread through the domain. This stress change also impacts the confining layers (both due to cooling and the mechanical interaction in other parts of the domain). The fault stiffness plays a secondary role in the resulting slip tendency, with a stiffer fault zone leading to slightly delayed fault reactivation and a higher variation of values across the fault.

4.4.2 Hazards

As mentioned in Section 4.2.5, the focus of this work is on fault rupture, and not the translation into seismicity, although fault rupture is a prerequisite for seismicity. It is seen here that in projects with similar geological conditions and fault strengths [Buijze et al., 2019], the relative stiffness of the caprock and reservoir play an important role. In situations with a stiffer caprock, the likelihood of reactivation is lower leading to a generally safer situation. However, stress changes are more local (when the cold front

reaches the fault), which can reduce the potential to monitor small scale seismicity prior to significant seismicity. In situations with a stiffer reservoir, the likelihood of seismicity is higher, but stress changes are more gradual, linked more to the overall cooling in the system. This implies that seismicity is likely to slowly increase (linked also to the predicted increase of rupture area in this work), and therefore monitoring can be used more effectively as a control tool. Reactivation is seen in this case to occur over a time span of several years. Any seismic impact will vary depending on whether the fault slip occurs incrementally or occurs in a single event and depends on several aspects including the material behaviour and state. This requires further research, linking fault slip and thermo-mechanical state and behaviour to the manifestation of seismicity. It is important to consider that, over a longer simulation period, the rupture area will continue to expand in the scenarios where it ruptures. Faults (or fault zones) with higher rigidity were shown to exhibit a larger slip area compared to a fault with lower rigidity (see Fig. 4.10). However, faults are in most cases avoided during drilling, which means that properties are difficult to estimate. This is the case in the examples considered here. This uncertainty is likely to persist in many projects and should be accounted for when assessing the temporal variation of fault rupture.

4.5 Summary and Conclusion

Understanding the reactivation of faults is crucial for mitigating the risks associated with induced or triggered seismicity in geothermal projects. A key aspect of this concern involves the cooling-induced reactivation of faults. In this study, a coupled thermo-hydro-mechanical model is presented to investigate the reactivation of faults within a porous and permeable sandstone reservoir. This work contributes to expanding our understanding of far-field fault reactivation and the impact of material properties on fault behavior. The fault under consideration was situated at 750 m away from the injection well, as is commonly targeted in hydrothermal systems. The reactivation of the fault occurs more readily in a reservoir with greater stiffness compared to the

caprock.

The normal stress on the fault in this situation is seen to progressively decrease and the shear stress progressively increase. After an initial reactivation, the affected area then expands laterally due to differences in permeability and stiffness between the caprock and the reservoir. In scenarios with a stiffer caprock, the stress changes are seen to be more local to the cooling zone, and the changes progress in a more non-linear manner. In this situation, where the fault was more stable, rupture was not seen to occur. This analysis of varying stiffness provides valuable insights into how fault rigidity influences reactivation behavior, which is crucial information for geothermal development.

In Unterhaching, Germany [Megies and Wassermann, 2014], Poing, Germany [Seithel et al., 2019] and the Californië geothermal field in the Netherlands [Vörös and Baisch, 2022], fault reactivation was primarily attributed to cooling effects rather than pore pressure changes, as seismic activity was observed well after pore pressure had stabilized. Our model supports this conclusion, showing that Mechanisms 1 and 2, which reach their maximum destabilizing effect after one year of production, are not the predominant factors. Instead, cooling appears to be the primary driver of significant changes in critical slip tendency.

It is common practice to ensure that the cooling plume has limited interaction with faults, as they are considered prone to reactivation if they fall within the cooling radius. In this study, the model results partially confirm this criterion. However, it is demonstrated that the escalation of shear stress and reduction in effective normal stress are consequences of coupled mechanisms, and interactions between the caprock and the reservoir. Consequently, if the initial slip tendency value approaches its failure threshold, the fault may slip due to reservoir contraction, prior to or after cold front interaction with the fault. Therefore, consideration should be given to faults that lie both inside and outside the cooling radius, especially where the caprock has a lower stiffness than the reservoir.

Chapter 5

Conclusions & Future Perspectives

Accurate numerical simulations of fracture and fault behavior rely on integrating complex physical processes. By coupling hydraulics, mechanics, and thermal aspects, accurate predictions and forecasts can be made in geothermal projects. These predictions are vital for decision-making processes and the design of geothermal operations. This thesis focuses on developing multiscale continuum equivalent media models to accurately replicate joint behavior. The goal of this thesis was to develop and test this approach to achieve accurate results. This thesis is structured into two main parts: employing this method for modeling joints in both EGS and hydrothermal systems, which are discussed below.

5.1 Efficiency of Enhanced Geothermal Systems

The enhancement of Enhanced Geothermal Systems relies on factors such as fracture orientation, in-situ stress tensor, initial aperture, fracture stiffness, and fracture roughness. The design of the injection scenario should consider the aforementioned factors to effectively stimulate fractures in an efficient manner. Achieving a commercial level of energy mining is contingent upon this enhancement.

In this thesis, the ECM approach is benchmarked against laboratory data. In Chapter 2, numerical modeling has played a pivotal role in quantifying both reversible

and irreversible aspects of fractures. The findings reveal that under smooth isotropic loading conditions, the aperture increases by 40% under an injection pressure of 15 MPa. Conversely, in a rough fracture under isotropic loading conditions, the aperture remains nearly constant under an injection pressure of 4.5 MPa. These results underscore the significant influence of fracture roughness on aperture variation. Rough fractures exhibit a larger initial aperture compared to smooth ones, albeit the relative variation is less pronounced than in smooth fractures. However, initiating hydraulic shearing with a smooth surface is technically more intricate than with a rough fracture surface.

Regarding anisotropic fracture stimulation, as presented in Chapter 2, at the laboratory scale a significant increase of b_{shear} up to 28 μm, accompanied by relatively small increases in normal aperture. In Chapter 3, during experiments at Grimsel that utilized similar injection pressures, the observed fracture behavior differed, with b_{normal} doubling and b_{shear} increasing up to 7.12 μm. In Chapter 2, an unrecoverable increase in permeability was dominant, while in Chapter 3, recoverable permeability was seen to dominant. These differences might be explained mostly by the boundary conditions, and material properties.

The observed water circulation at Grimsel, confirmed by the fracture pressure PRP2, validates the accuracy of the numerical solution. Moreover, the numerical model performs better than linear diffusion models because it considers pressure-dependent permeability. This distinction is crucial as linear diffusion models ignore permeability dependencies, leading to smaller areas experiencing higher pressures. Consequently, this non-conservative approach could result in underestimated ruptured areas and reduced safety in predicting the size of seismic events.

In both Chapters 2 and 3, a reasonable accuracy between the data and numerical model demonstrates that the Equivalent Continuum Model can effectively model stimulation in Enhanced Geothermal Systems. Unrecoverable permeability enhancement can be attained with a rough surface and under anisotropic stress conditions. Throughout these chapters, it is observed that higher injection pressures lead to greater perme-

ability enhancement. However, it is important to note that this increase in injection pressure may also result in induced seismicity, although this aspect has not been investigated in this study. Enhancing the efficiency of EGS ensures a more significant return on investment.

5.2 Safety in Hydrothermal Systems

Using the ECM approach to model faults has revealed that faults in the far-field can be triggered. The extraction of hot fluids and injection of cold fluids perturb pore pressure and temperature. As noted in Chapter 4, this perturbation directly affects fault stability. The degree of stress change on the fault depends on the fault/reservoir/confining layer's stiffness. A softer reservoir and stiffer confining layer is more conservative than a stiffer reservoir and soft confining layer. In all scenario a stiff fault increases the slip tendency leading to a more critical case. The normal effective stress on the fault decreases by up to 25%, while the shear stress acting on the fault increases by up to 28.7%.

When the confining layers are stiffer than the reservoir, fault reactivation is unlikely because stress redistributes along the entire fault rather than concentrating at its center. Conversely, in the opposite scenario, stress predominantly transfers to the fault's center, resulting in reactivation. The ruptured area starts forming near the center of the fault as the cold front reaches it. Its spread is influenced by both cooling and fault stiffness. A fault with high stiffness typically experiences earlier reactivation. However, it is demonstrated here that the rate of reactivation is independent of the fault stiffness. Chapter 4 demonstrates that if the initial slip tendency value approaches its failure threshold, the fault may slip due to reservoir contraction before the cold front penetrates it.

The safety of hydrothermal operation relies on its ability to prevent significant seismic activity. Faults may be reactivated, as demonstrated in Chapter 4, however the resulting seismicity needs to be properly assessed and controlled. However, it is

crucial to carefully limit the heat extraction rate in a hydrothermal system due to the potential for fault reactivation induced by pore pressure changes and cooling, which in turn lead to stress alterations. This research on hydrothermal systems aims to mitigate micro-seismicity, thereby fostering greater public acceptance of geothermal energy and preventing the 'not in my backyard' phenomenon

5.3 Future Perspectives

The modeling results of this thesis provide valuable knowledge about fracture behavior in EGS and the fault reactivation in hydrothermal system. They also make clear that more work must be performed, and indicate a number of recommendation for further study.

In Chapter 2, there is potential for extending this work by introducing a partially saturated condition, considering air/water phases and their interactions to model the on going saturation that took place in the first injection steps. Furthermore, integrating a well simulator to model the packer system can improve the accuracy of the injection modeling. The incorporation of the Step-Rate Injection Method for Fracture In-Situ Properties (SIMFIP) can yield more precise laboratory measurements, including aperture changes. This, in turn, facilitates better comparison and calibration of the model.

In Chapter 3, the formation of cracks and the extension of fractures were not considered in this work, suggesting the potential for further extension of the framework in that direction. Integrating these aspects into the framework would contribute to a better understanding of fracture enhancement. Moreover, extending the framework by including seismicity could enhance the forecasting over the injection scenario by reducing the likelihood of it being seismogenic.

In Chapter 4, is worth noting that the step from fault slippage to seismicity is not included. A calculation of the seismic moment tensor is needed, as well as more sophisticated constituvie models, which allow for a build up of strain energy which can be released in specific events. This results in an unknown frequency or magnitude

for these events. Moreover, integrating changes in fluid properties with temperature would enhance the reliability of the scenarios, specifically useful for a site specific analysis. However, the simulations presented here represent a hypothetical geothermal exploitation scenario. Comparing these simulations with real-world scenarios can contribute to the calibration and accuracy of the model.

References

P. Achtziger-Zupančič, S. Loew, and G. Mariethoz. A new global database to improve predictions of permeability distribution in crystalline rocks at site scale. *Journal of Geophysical Research: Solid Earth*, 122(5):3513–3539, 2017.

M. Almakari, H. Chauris, F. Passelègue, P. Dublanchet, and A. Gesret. Fault's hydraulic diffusivity enhancement during injection induced fault reactivation: application of pore pressure diffusion inversions to laboratory injection experiments. *Geophysical Journal International*, 223(3):2117–2132, 2020.

F. Amann, V. Gischig, K. Evans, J. Doetsch, R. Jalali, B. Valley, H. Krietsch, N. Dutler, L. Villiger, B. Brixel, et al. The seismo-hydromechanical behavior during deep geothermal reservoir stimulations: Open questions tackled in a decameter-scale in situ stimulation experiment. *Solid Earth*, 9(1):115–137, 2018.

S. Baisch, R. Vörös, E. Rothert, H. Stang, R. Jung, and R. Schellschmidt. A numerical model for fluid injection induced seismicity at soultz-sous-forêts. *International Journal of Rock Mechanics and Mining Sciences*, 47(3):405–413, 2010.

S. Balay, S. Abhyankar, M. Adams, J. Brown, P. Brune, K. Buschelman, L. Dalcin, V. Eijkhout, W. Gropp, D. Kaushik, et al. PETSc users manual revision 3.8. Technical report, Office of Scientific and Technical Information (OSTI), 2017.

S.C. Bandis, A.C. Lumsden, and N.R. Barton. Fundamentals of rock joint deformation. In *International Journal of Rock Mechanics and Mining Sciences & Geomechanics Abstracts*, volume 20, pages 249–268. Elsevier, 1983.

R Baria, E Majer, M Fehler, N Toksoz, CJ Bromley, and D Teza. Induced seismicity in geothermal systems and public concern. *Proc, First European Geothermal Review*, pages 29–31, 2007.

N. Barton. Review of a new shear-strength criterion for rock joints. *Engineering Geology*, 7(4):287–332, 1973.

B. Bendall, R. Hogarth, H. Holl, A. McMahon, A. Larking, and P. Reid. Australian experiences in EGS permeability enhancement–a review of 3 case studies. In *Thirty-Ninth Workshop on Geothermal Reservoir Engineering, Stanford University, California*, 2014.

Y. Bernabe. The effective pressure law for permeability in chelmsford granite and barre granite. In *International Journal of Rock Mechanics and Mining Sciences & Geomechanics Abstracts*, volume 23, pages 267–275. Elsevier, 1986.

M.A. Biot. Theory of elasticity and consolidation for a porous anisotropic solid. *Journal of Applied Physics*, 26(2):182–185, 1955.

G. Blöcher, M. Cacace, A. B. Jacquey, A. Zang, O. Heidbach, H. Hofmann, C. Kluge, and G. Zimmermann. Evaluating micro-seismic events triggered by reservoir operations at the geothermal site of Groß Schönebeck (Germany). *Rock Mechanics and Rock Engineering*, 51:3265–3279, 2018.

P. Bossart, F. Bernier, J. Birkholzer, C. Bruggeman, P. Connolly, S. Dewonck, M. Fukaya, M. Herfort, M. Jensen, J.-M. Matray, et al. Mont Terri Rock Laboratory, 20 years of research: Introduction, site characteristics and overview of experiments. *Mont Terri Rock Laboratory, 20 Years: Two Decades of Research and Experimentation on Claystones for Geological Disposal of Radioactive Waste*, pages 3–22, 2018.

A. F. Bower. *Applied Mechanics of Solids*. CRC Press, 2009.

A. Boyet, S. De Simone, S. Ge, and V. Vilarrasa. Poroelastic stress relaxation, slip stress transfer and friction weakening controlled post-injection seismicity at the Basel Enhanced Geothermal System. *Communications Earth & Environment*, 4(1):104, 2023.

K. Breede, K. Dzebisashvili, X. Liu, and G. Falcone. A systematic review of enhanced (or engineered) geothermal systems: past, present and future. *Geothermal Energy*, 1:1–27, 2013.

B. Brixel, M. Klepikova, Q. Lei, C. Roques, M. Jalali, H. Krietsch, and S. Loew. Tracking fluid flow in shallow crustal fault zones: 2. insights from cross-hole forced flow experiments in damage zones. *Journal of Geophysical Research: Solid Earth*, 125(4):e2019JB019108, 2020.

D. Brown. The US hot dry rock program-20 years of experience in reservoir testing. In *Proceedings of the world geothermal congress, Florence, Italy*, volume 4, pages 2607–2611, 1995.

L. Buijze, L. van Bijsterveldt, H. Cremer, B. Paap, H. Veldkamp, B. B. T. Wassing, J.-D. Van Wees, G. C. N. van Yperen, J. H. ter Heege, and B. Jaarsma. Review of induced seismicity in geothermal systems worldwide and implications for geothermal systems in the Netherlands. *Netherlands Journal of Geosciences*, 98:e13, 2019.

L. Buijze, H. Veldkamp, and B. Wassing. Comparison of hydrocarbon and geothermal energy production in the Netherlands: reservoir characteristics, pressure and temperature changes, and implications for fault reactivation. *Netherlands Journal of Geosciences*, 102:e7, 2023.

M. Cacace and A. B. Jacquey. Flexible parallel implicit modelling of coupled thermal–hydraulic–mechanical processes in fractured rocks. *Solid Earth*, 8(5):921–941, 2017.

F. Cappa, Y. Guglielmi, J. Rutqvist, C.F. Tsang, and A. Thoraval. Hydromechanical modelling of pulse tests that measure fluid pressure and fracture normal displacement

at the coaraze laboratory site, france. *International Journal of Rock Mechanics and Mining Sciences*, 43(7):1062–1082, 2006.

F. Cappa, Y. Guglielmi, C. Nussbaum, L. De Barros, and J. Birkholzer. Fluid migration in low-permeability faults driven by decoupling of fault slip and opening. *Nature Geoscience*, 15(9):747–751, 2022.

LM Cathles. An analysis of the cooling of intrusives by ground-water convection which includes boiling. *Economic Geology*, 72(5):804–826, 1977.

L.M. Cathles. Scales and effects of fluid flow in the upper crust. *Science*, 248(4953): 323–329, 1990.

G.V. Chilingarian and K.H. Wolf. *Compaction of coarse-grained sediments, I.* Elsevier, 1975.

T. Cladouhos, S. Petty, B. Larson, J. Iovenitti, B. Livesay, and R. Baria. Toward more efficient heat mining: A planned enhanced geothermal system demonstration project. *GRC Transactions*, 33:165–170, 2009.

C. Clauser, K. Willbrand, M. Ziegler, M. Feinedegen, P. Siebert, T.-P. Fries, and N. Weber. Entwicklung eines werkzeus zur auslegung von HDR-risssystemen, 2015.

N.G.W. Cook. Natural joints in rock: mechanical, hydraulic and seismic behaviour and properties under normal stress. In *International Journal of Rock Mechanics and Mining Sciences & Geomechanics Abstracts*, volume 29, pages 198–223. Elsevier, 1992.

C. W. A. Cryer. A comparison of the three-dimensional consolidation theories of biot and terzaghi. *The Quarterly Journal of Mechanics and Applied Mathematics*, 16(4): 401–412, 1963.

L. P. Dake. *Fundamentals of reservoir engineering.* Elsevier, 1983.

P. Deb, S. Düber, C. Guarnieri Calo'Carducci, and C. Clauser. Laboratory-scale hydraulic fracturing dataset for benchmarking of enhanced geothermal system simulation tools. *Scientific Data*, 7(1):220, 2020.

P. Deb, S. Salimzadeh, D. Vogler, S. Düber, C. Clauser, and R.R. Settgast. Verification of coupled hydraulic fracturing simulators using laboratory-scale experiments. *Rock Mechanics and Rock Engineering*, 54:2881–2902, 2021.

N. Deichmann and D. Giardini. Earthquakes induced by the stimulation of an enhanced geothermal system below basel (switzerland). *Seismological Research Letters*, 80(5): 784–798, 2009.

J. Doetsch, V. Gischig, H. Krietsch, L. Villiger, F. Amann, N. Dutler, R. Jalali, B. Brixel, M. Klepikova, C. Roques, et al. Grimsel isc experiment description. Technical report, ETH Zurich, 2018.

J. Doetsch, H. Krietsch, C. Schmelzbach, M. Jalali, V. Gischig, L. Villiger, F. Amann, and H. Maurer. Characterizing a decametre-scale granitic reservoir using ground-penetrating radar and seismic methods. *Solid Earth*, 11(4):1441–1455, 2020.

L. Duboeuf, L. De Barros, M. Kakurina, Y. Guglielmi, F. Cappa, and B. Valley. Aseismic deformations perturb the stress state and trigger induced seismicity during injection experiments. *Geophysical Journal International*, 224(2):1464–1475, 2021.

J.M.C. Duhamel. *Mémoire sur la Méthode générale relative au Mouvement de la chaleur dans les corps solides plongés dans des milieux dont la température varie avec le temps: Résumé de deux autres Mém. présentés à l'Institut; Avec notes.* 1832.

B. A. Eaton. Fracture gradient prediction and its application in oilfield operations. *Journal of Petroleum Technology*, 21(10):1353–1360, 1969.

T. Einarsson. *Über das Wesen der Heissen Quellen Islands: Mit einer Übersicht über die Tektonik des Mittleren Nordislands.* Vísindafélag Íslendinga, 1942.

K. F. Evans, H. Moriya, H. Niitsuma, R. H. Jones, W. S. Phillips, A. Genter, J. Sausse, R. Jung, and R. Baria. Microseismicity and permeability enhancement of hydrogeologic structures during massive fluid injections into granite at 3 km depth at the soultz HDR site. *Geophysical Journal International*, 160(1):388–412, 2005.

I. Fatt and D. H. Davis. Reduction in permeability with overburden pressure. *Journal of Petroleum Technology*, 4(12):16–16, 1952.

J. Geertsma. The effect of fluid pressure decline on volumetric changes of porous rocks. *Transactions of the AIME*, 210(01):331–340, 1957a.

J. Geertsma. A remark on the analogy between thermoelasticity and the elasticity of saturated porous media. *Journal of the Mechanics and Physics of Solids*, 6(1):13–16, 1957b.

A Gens, J Carrera, and EE Alonso. Numerical formulation for a simulator (code_bright) for the coupled analysis of saline media. *Engineering computations*, 13(7):87–112, 1996.

S. Gentier, J. Riss, G. Archambault, R. Flamand, and D. Hopkins. Influence of fracture geometry on shear behavior. *International Journal of Rock Mechanics and Mining Sciences*, 37(1-2):161–174, 2000.

S. Ghabezloo and J. Sulem. Stress dependent thermal pressurization of a fluid-saturated rock. *Rock Mechanics and Rock Engineering*, 42:1–24, 2009.

V. S. Gischig and G. Preisig. Hydro-fracturing versus hydro-shearing: A critical assessment of two distinct reservoir stimulation mechanisms. In *ISRM Congress*, pages ISRM–13CONGRESS. ISRM, 2015.

V. S. Gischig, D. Giardini, F. Amann, M. Hertrich, H. Krietsch, S. Loew, H. Maurer, L. Villiger, S. Wiemer, F. Bethmann, et al. Hydraulic stimulation and fluid circulation experiments in underground laboratories: Stepping up the scale towards

engineered geothermal systems. *Geomechanics for Energy and the Environment*, 24: 100175, 2020.

G. Giudicelli, A. Lindsay, L. Harbour, C. Icenhour, M. Li, J. E. Hansel, P. German, P. Behne, O. Marin, R. H. Stogner, J. M. Miller, D. Schwen, Y. Wang, L. Munday, S. Schunert, B. W. Spencer, D. Yushu, A. Recuero, Z. M. Prince, M. Nezdyur, T. Hu, Y. Miao, Y. S. Jung, C. Matthews, A. Novak, B. Langley, T. Truster, N. Nobre, B. Alger, D. Andrš, F. Kong, R. Carlsen, A. E. Slaughter, J. W. Peterson, D. Gaston, and C. F Permann. 3.0 - MOOSE: Enabling massively parallel multiphysics simulations. *SoftwareX*, 26:101690, 2024. ISSN 2352-7110.

A. Golchin, P. J. Vardon, M. A. Hicks, W. M. Coombs, and I. A. Pantev. On the numerical implementation of a thermomechanical hyperplasticity model for fine-grained soils. In *Challenges and Innovations in Geomechanics: Proceedings of the 16th International Conference of IACMAG-Volume 1 16*, pages 422–429. Springer, 2021.

A. Golchin, P. J. Vardon, and M. A. Hicks. A thermo-mechanical constitutive model for fine-grained soils based on thermodynamics. *International Journal of Engineering Science*, 174:103579, 2022.

R. E. Goodman. The mechanical properties of joints. *Proc 3rd Int Congr International Society of Rock Mechanics*, pages 1–7, 1974.

R.E. Goodman. *Methods of geological engineering in discontinuous rocks*. West Publishing Company, 1976.

M. Grant. *Geothermal Reservoir Engineering*. Elsevier, 2013.

G. Grasselli, A. Lisjak, O.K. Mahabadi, and B.S.A. Tatone. Influence of pre-existing discontinuities and bedding planes on hydraulic fracturing initiation. *European Journal of Environmental and Civil Engineering*, 19(5):580–597, 2015.

Y. Guglielmi, F. Cappa, J.-P. Avouac, P. Henry, and D. Elsworth. Seismicity triggered by fluid injection–induced aseismic slip. *Science*, 348(6240):1224–1226, 2015.

Y. Guglielmi, J. Birkholzer, J. Rutqvist, P. Jeanne, and C. Nussbaum. Can fault leakage occur before or without reactivation? Results from an in situ fault reactivation experiment at Mont Terri. *Energy Procedia*, 114:3167–3174, 2017.

Y. Guglielmi, C. Nussbaum, J. Rutqvist, F. Cappa, P. Jeanne, and J. Birkholzer. Estimating perturbed stress from 3-D borehole displacements induced by fluid injection in fractured or faulted shales. *Geophysical Journal International*, 221(3):1684–1695, 2020.

Y. Guglielmi, C. Nussbaum, F. Cappa, L. De Barros, J. Rutqvist, and J. Birkholzer. Field-scale fault reactivation experiments by fluid injection highlight aseismic leakage in caprock analogs: Implications for CO2 sequestration. *International Journal of Greenhouse Gas Control*, 111:103471, 2021.

A. Gérard, A. Genter, T. Kohl, P. Lutz, P. Rose, and F. Rummel. The deep EGS (enhanced geothermal system) project at Soultz-sous-Forêts (Alsace, France). *Geothermics*, 35(5):473–483, 2006.

G. Han and M. B. Dusseault. Description of fluid flow around a wellbore with stress-dependent porosity and permeability. *Journal of Petroleum Science and Engineering*, 40(1-2):1–16, 2003.

M. O. Häring, U. Schanz, F. Ladner, and B. C. Dyer. Characterisation of the basel 1 enhanced geothermal system. *Geothermics*, 37(5):469–495, 2008.

J. H. Healy, S. H. Hickman, M. D. Zoback, and W. L. Ellis. Report on televiewer log and stress measurements in core hole USW-G1, Nevada Test Site, December 13-22, 1981. Technical report, Geological Survey, Menlo Park, CA (United States); US Geological Survey, 1984.

S. Hirschberg, S. Wiemer, and P. Burgherr. *Energy from the Earth: Deep Geothermal as a Resource for the Future?*, volume 62. vdf Hochschulverlag AG, 2014.

E. Huenges. In-situ geothermielabor Groß Schönebeck 2000/2001. *Scientific Technical Report/Geoforschungszentrum Potsdam*, 2002.

IPCC. *Synthesis Report: Climate Change 2014*. IPCC, 2014.

IRENA. *Renewable energy statistics 2023*. IRENA, 2023.

T. Ishibashi, D. Elsworth, Y. Fang, J. Riviere, B. Madara, H. Asanuma, N. Watanabe, and C. Marone. Friction-stability-permeability evolution of a fracture in granite. *Water Resources Research*, 54(12):9901–9918, 2018.

FLAC Itasca. FLAC-Fast lagrangian analysis of continua, ersion. 7.0. *Itasca Consulting Group Inc., Minneapolis*, 2011.

A. B. Jacquey, M. Cacace, G. Blöcher, and M. Scheck-Wenderoth. Numerical investigation of thermoelastic effects on fault slip tendency during injection and production of geothermal fluids. *Energy Procedia*, 76:311–320, 2015.

A. B. Jacquey, M. Cacace, G. Blöcher, N. Watanabe, E. Huenges, and M. Scheck-Wenderoth. Thermo-poroelastic numerical modelling for enhanced geothermal system performance: Case study of the Groß Schönebeck reservoir. *Tectonophysics*, 684:119–130, 2016.

A. B. Jacquey, L. Urpi, M. Cacace, G. Blöcher, G. Zimmermann, and M. Scheck-Wenderoth. Far field poroelastic response of geothermal reservoirs to hydraulic stimulation treatment: Theory and application at the Groß Schönebeck geothermal research facility. *International Journal of Rock Mechanics and Mining Sciences*, 110:316–327, 2018.

J.C. Jaeger, N.G.W. Cook, and R. Zimmerman. *Fundamentals of rock mechanics*. John Wiley & Sons, 2009.

M. Jalali, M. Klepikova, J. Doetsch, H. Krietsch, B. Brixel, N. Dutler, V. Gischig, and F. Amann. A multi-scale approach to identify and characterize the preferential

flow paths of a fractured crystalline rock. In *ARMA International Discrete Fracture Network Engineering Conference*, page D033S020R001. ARMA, 2018.

P. Jeanne, J. Rutqvist, P. F. Dobson, M. Walters, C. Hartline, and J. Garcia. The impacts of mechanical stress transfers caused by hydromechanical and thermal processes on fault stability during hydraulic stimulation in a deep geothermal reservoir. *International Journal of Rock Mechanics and Mining Sciences*, 72:149–163, 2014.

P. Jeanne, Y. Guglielmi, J. Rutqvist, C. Nussbaum, and J. Birkholzer. Permeability variations associated with fault reactivation in a claystone formation investigated by field experiments and numerical simulations. *Journal of Geophysical Research: Solid Earth*, 123(2):1694–1710, 2018.

R. Jung. Hydraulic in situ investigations of an artificial fracture in the Falkenberg granite. In *International Journal of Rock Mechanics and Mining Sciences & Geomechanics Abstracts*, volume 26, pages 301–308. Elsevier, 1989.

S. Kelkar, G. WoldeGabriel, and K. Rehfeldt. Lessons learned from the pioneering hot dry rock project at Fenton Hill, USA. *Geothermics*, 63:5–14, 2016.

H. R. Keusen, J. Ganguin, P. Schuler, and M. Buletti. Felslabor Grimsel geologie nagra technischer bericht ntb 87-14. 166. *Nagra & Geotest*, 1989a.

H. R. Keusen, J. Ganguin, P. Schuler, and M. Buletti. Grimsel test site: geology. Technical report, Nationale Genossenschaft fuer die Lagerung Radioaktiver Abfaelle (NAGRA), 1989b.

K. Kim, J. Ree, Y. Kim, S. Kim, S. Y. Kang, and W. Seo. Assessing whether the 2017 $M_w 5.4 Pohang earthquake in South Korea was an induced event$. *Science*, 360 (6392) : 1007 − −1009, 2018.

B. S. Kirk, J. W. Peterson, R. H. Stogner, and G. F. Carey. libMesh: a C++ library for parallel adaptive mesh refinement/coarsening simulations. *Engineering with Computers*, 22:237–254, 2006.

I. R. Kivi, E. Pujades, J. Rutqvist, and V. Vilarrasa. Cooling-induced reactivation of distant faults during long-term geothermal energy production in hot sedimentary aquifers. *Scientific Reports*, 12(1):2065, 2022.

I. R. Kivi, A. Boyet, H. Wu, L. Walter, S. Hanson-Hedgecock, F. Parisio, and V. Vilarrasa. Global physics-based database of injection-induced seismicity. *Earth System Science Data Discussions*, 2023:1–33, 2023.

O. Kolditz, S. Bauer, L. Bilke, N. Böttcher, J.-O. Delfs, T. Fischer, U. J. Görke, T. Kalbacher, G. Kosakowski, C. I. McDermott, et al. OpenGeoSys: an open-source initiative for numerical simulation of thermo-hydro-mechanical/chemical (THM/C) processes in porous media. *Environmental Earth Sciences*, 67:589–599, 2012.

H. Krietsch. *Hydro-mechanical responses of a fractured rock mass during decameter-scale hydraulic stimulation experiments*. PhD thesis, ETH Zurich, 2019.

H. Krietsch, J. Doetsch, N. Dutler, M. Jalali, V. Gischig, S. Loew, and F. Amann. Comprehensive geological dataset describing a crystalline rock mass for hydraulic stimulation experiments. *Scientific Data*, 5(1):1–12, 2018.

H. Krietsch, V. Gischig, K. Evans, J. Doetsch, N. O. Dutler, B. Valley, and F. Amann. Stress measurements for an in situ stimulation experiment in crystalline rock: integration of induced seismicity, stress relief and hydraulic methods. *Rock Mechanics and Rock Engineering*, 52:517–542, 2019.

H. Krietsch, V.S. Gischig, J. Doetsch, K.F. Evans, L. Villiger, M. Jalali, B. Valley, S. Löw, and F. Amann. Hydromechanical processes and their influence on the stimulation effected volume: observations from a decameter-scale hydraulic stimulation project. *Solid Earth*, 11(5):1699–1729, 2020.

M. Kruszewski, G. Montegrossi, and E. H. Saenger. The risk of fluid-injection-induced fault reactivation in carbonate reservoirs: an investigation of a geothermal system

in the Ruhr region (Germany). *Geomechanics and Geophysics for Geo-Energy and Geo-Resources*, 9(1):38, 2023.

I. T. Kukkonen, P. J. Heikkinen, P. E. Malin, J. Renner, G. Dresen, A. Karjalainen, J. Rytkönen, and J. Solantie. Hydraulic conductivity of the crystalline crust: Insights from hydraulic stimulation and induced seismicity of an enhanced geothermal system pilot reservoir at 6 km depth, Espoo, southern Finland. *Geothermics*, 112:102743, 2023.

R. Law. Deep geothermal UK-United downs project, Redruth. In *UK: Proceedings of the ground source live workshop*, 2011.

H.S. Lee and T.F. Cho. Hydraulic characteristics of rough fractures in linear flow under normal and shear load. *Rock Mechanics and Rock Engineering*, 35(4):299–318, 2002.

Z. Li, X. Ma, X.-Z. Kong, M. O. Saar, and D. Vogler. Permeability evolution during pressure-controlled shear slip in saw-cut and natural granite fractures. *Rock Mechanics Bulletin*, 2(2):100027, 2023.

A. Lisjak, O.K. Mahabadi, P. Kaifosh, T. Vietor, and G. Grasselli. A preliminary evaluation of an enhanced FDEM code as a tool to simulate hydraulic fracturing in jointed rock masses. In *ISRM EUROCK*, pages ISRM–EUROCK. ISRM, 2014.

J. C. S. Long, J. S. Remer, C. R. Wilson, and P. A. Witherspoon. Porous media equivalents for networks of discontinuous fractures. *Water Resources Research*, 18 (3):645–658, 1982.

Harold Wesley Lord and Y Shulman. A generalized dynamical theory of thermoelasticity. *Journal of the Mechanics and Physics of Solids*, 15(5):299–309, 1967.

S.-M. Lu. A global review of enhanced geothermal system (EGS). *Renewable and Sustainable Energy Reviews*, 81:2902–2921, 2018.

W. Luo, A. Kottsova, P.J. Vardon, A.C. Dieudonné, and M. Brehme. Mechanisms causing injectivity decline and enhancement in geothermal projects. *Renewable and Sustainable Energy Reviews*, 185:113623, 2023.

W. Luo, J. Liaudat, J. Ouf, A.C. Dieudonné, F. Amann, and P.J. Vardon. Numerical modelling of fracturing processes during cold water injection into geothermal reservoirs: Verification and qualitative validation. *Computers and Geotechnics*, 183:107186, 2025. ISSN 0266-352X. doi: https://doi.org/10.1016/j.compgeo.2025.107186. URL blackhttps://www.sciencedirect.com/science/article/pii/S0266352X25001351.

Q. J. Ma, C. W. W. Ng, D. Mašín, and C. Zhou. An approach for modelling volume change of fine-grained soil subjected to thermal cycles. *Canadian Geotechnical Journal*, 54(6):896–901, 2017.

X. Ma, M. Hertrich, F. Amann, K. Bröker, N. G. Doonechaly, V. Gischig, R. Hochreutener, P. Kästli, H. Krietsch, M. Marti, et al. Multi-disciplinary characterizations of the bedretto lab–a unique underground geoscience research facility. *Solid Earth Discussions*, 2021.

L. E. Malvern. *Introduction to the Mechanics of a Continuous Medium*. Prentice-Hall, 1969.

J. Mandel. Consolidation des sols (étude mathématique). *Géotechnique*, 3(7):287–299, 1953.

G. Mandl. *Rock joints*. Springer, 2005.

C. E. Manning and S. E. Ingebritsen. Permeability of the continental crust: Implications of geothermal data and metamorphic systems. *Reviews of Geophysics*, 37(1): 127–150, 1999.

M.W. McClure and R.N. Horne. An investigation of stimulation mechanisms in enhanced geothermal systems. *International Journal of Rock Mechanics and Mining Sciences*, 72:242–260, 2014.

D.F. McTigue. Thermoelastic response of fluid-saturated porous rock. *Journal of Geophysical Research: Solid Earth*, 91(B9):9533–9542, 1986.

T. Megies and J. Wassermann. Microseismicity observed at a non-pressure-stimulated geothermal power plant. *Geothermics*, 52:36–49, 2014.

K.B. Min, J. Rutqvist, C.F. Tsang, and L. Jing. Stress-dependent permeability of fractured rock masses: a numerical study. *International Journal of Rock Mechanics and Mining Sciences*, 41(7):1191–1210, 2004.

I. Moeck, G. Kwiatek, and G. Zimmermann. Slip tendency analysis, fault reactivation potential and induced seismicity in a deep geothermal reservoir. *Journal of Structural Geology*, 31(10):1174–1182, 2009a.

Inga Moeck, Heinz Schandelmeier, and Heinz-Gerd Holl. The stress regime in a rotliegend reservoir of the northeast german basin. *International Journal of Earth Sciences*, 98:1643–1654, 2009b.

A. Morris, D. A. Ferrill, and D. B. Henderson. Slip-tendency analysis and fault reactivation. *Geology*, 24(3):275–278, 1996.

V. N. S. Murthy. Soil mechanics and foundation engineering. *Sai Kripa Technical Consultants*, 1, 1989.

R. Myers and A. Aydin. The evolution of faults formed by shearing across joint zones in sandstone. *Journal of Structural Geology*, 26(5):947–966, 2004.

M. Oda. A method for evaluating the representative elementary volume based on joint survey of rock masses. *Canadian Geotechnical Journal*, 25(3):440–447, 1988.

R. Olsson and N. Barton. An improved model for hydromechanical coupling during shearing of rock joints. *International Journal of Rock Mechanics and Mining Sciences*, 38(3):317–329, 2001.

J. Ouf, K. Khaledi, P.J Vardon, W Luo, M. Jalali, and F. Amann. Numerical modeling of hydro-mechanical processes during hydraulic testing of fractures at the grimsel test site, switzerland. *Geomechanics for Energy and the Environment*, 40, 2024a.

J. Ouf, J. Osten, W. Luo, K. Khaledi, M. Jalali, P.J. Vardon, and F. Amann. Experimental and numerical analysis of injection-induced permeability changes in pre-existing fractures. *Geomechanics for Energy and the Environment*, 39:100576, 2024b.

J. Ouf, P.J. Vardon, K. Khaledi, W. Luo, M. Jalali, and F. Amann. Numerical analysis of far-field fault reactivation induced by reservoir cooling. *Geothermics*, 127:103234, 2025. ISSN 0375-6505.

V.V. Palciauskas and P.A. Domenico. Fluid pressures in deforming porous rocks. *Water Resources Research*, 25(2):203–213, 1989.

A. Palmstrom. *RMi-A Rock Mass Characterization System for Rock Engineering Purposes - Ph.D. Thesis*. na, 1995.

S.N. Pandey, V. Vikram, and A. Chaudhuri. Geothermal reservoir modeling in a coupled thermo-hydro-mechanical-chemical approach: A review. *Earth-Science Reviews*, 185:1157–1169, 2018.

M.L. Panel. The future of geothermal energy: Impact of enhanced geothermal systems (EGS) on the United States in the 21st century. *Geothermics*, 17(5/6):881–882, 2006.

J.-W. Park, Y. Guglielmi, B. Graupner, J. Rutqvist, T. Kim, E.-S. Park, and C. Lee. Modeling of fluid injection-induced fault reactivation using coupled fluid flow and mechanical interface model. *International Journal of Rock Mechanics and Mining Sciences*, 132:104373, 2020.

R. Parri and F. Lazzeri. Larderello: 100 years of geothermal power plant evolution in Italy. In *Geothermal Power Generation*, pages 537–590. Elsevier, 2016.

C.J. Permann, D.R. Gaston, D. Andrš, R.W. Carlsen, F. Kong, A.D. Lindsay, J.M. Miller, J.W. Peterson, A.E. Slaughter, R.H. Stogner, and R.C. Martineau. MOOSE: Enabling massively parallel multiphysics simulation. *SoftwareX*, 11:100430, 2020. doi: 10.1016/j.softx.2020.100430.

S. Petty, Y. Nordin, W. Glassley, T. T. Cladouhos, and M. Swyer. Improving geothermal project economics with multi-zone stimulation: Results from the Newberry Volcano EGS demonstration. In *Proceedings of the Thirty-Eighth Workshop on Geothermal Reservoir Engineering*, pages 11–13, 2013.

S. Piesnack. Tiefe geothermie in Deutschland 2023/24. *Bundesverband Geothermie*, 2023.

R. J. Pine and A. S. Batchelor. Downward migration of shearing in jointed rock during hydraulic injections. In *International Journal of Rock Mechanics and Mining Sciences & Geomechanics Abstracts*, volume 21, pages 249–263. Elsevier, 1984.

J. D. Platt, J. W. Rudnicki, and J. R. Rice. Stability and localization of rapid shear in fluid-saturated fault gouge: 2. localized zone width and strength evolution. *Journal of Geophysical Research: Solid Earth*, 119(5):4334–4359, 2014.

N.J. Price. *Fault and joint development: in brittle and semi-brittle rock*. Elsevier, 2016.

A. Puzrin. *Constitutive Modelling in Geomechanics: Introduction*. Springer Science & Business Media, 2012.

H. Rattez, I. Stefanou, and J. Sulem. The importance of thermo-hydro-mechanical couplings and microstructure to strain localization in 3D continua with application to seismic faults. Part I: Theory and linear stability analysis. *Journal of the Mechanics and Physics of Solids*, 115:54–76, 2018a. doi: https://doi.org/10.1016/j.jmps.2018.03.004.

H. Rattez, I. Stefanou, J. Sulem, M. Veveakis, and T. Poulet. The importance of thermo-hydro-mechanical couplings and microstructure to strain localization in 3D continua with application to seismic faults. Part II: Numerical implementation and post-bifurcation analysis. *Journal of the Mechanics and Physics of Solids*, 115:1–29, 2018b.

A. Reinicke, G. Zimmermann, E. Huenges, and H. Burkhardt. Estimation of hydraulic parameters after stimulation experiments in the geothermal reservoir Groß Schönebeck 3/90 (North-German Basin). *International Journal of Rock Mechanics and Mining Sciences*, 42(7-8):1082–1087, 2005.

A. P. Rinaldi, J. Rutqvist, E. L. Sonnenthal, and T. T. Cladouhos. Coupled THM modeling of hydroshearing stimulation in tight fractured volcanic rock. *Transport in Porous Media*, 108(1):131–150, 2015.

A.P. Rinaldi and J. Rutqvist. Joint opening or hydroshearing? Analyzing a fracture zone stimulation at Fenton Hill. *Geothermics*, 77:83–98, 2019.

J. Rutqvist. Determination of hydraulic normal stiffness of fractures in hard rock from well testing. In *International Journal of Rock Mechanics and Mining Sciences & Geomechanics Abstracts*, volume 32, pages 513–523. Elsevier, 1995.

J. Rutqvist. Fractured rock stress–permeability relationships from in situ data and effects of temperature and chemical–mechanical couplings. *Crustal Permeability*, pages 65–82, 2012.

J. Rutqvist. An overview of TOUGH-based geomechanics models. *Computers & Geosciences*, 108:56–63, 2017.

J. Rutqvist and C-F. Tsang. Analysis of thermal–hydrologic–mechanical behavior near an emplacement drift at yucca mountain. *Journal of Contaminant Hydrology*, 62: 637–652, 2003.

J. Rutqvist, Y-S. Wu, C-F. Tsang, and G. Bodvarsson. A modeling approach for analysis of coupled multiphase fluid flow, heat transfer, and deformation in fractured porous rock. *International Journal of Rock Mechanics and Mining Sciences*, 39(4): 429–442, 2002.

J. Rutqvist, A. P. Rinaldi, F. Cappa, and G. J. Moridis. Modeling of fault reactivation and induced seismicity during hydraulic fracturing of shale-gas reservoirs. *Journal of Petroleum Science and Engineering*, 107:31–44, 2013.

J. Rutqvist, A. P. Rinaldi, F. Cappa, and G. J. Moridis. Modeling of fault activation and seismicity by injection directly into a fault zone associated with hydraulic fracturing of shale-gas reservoirs. *Journal of Petroleum Science and Engineering*, 127: 377–386, 2015.

J. Rutqvist, B. Graupner, Y. Guglielmi, T. Kim, J. Maßmann, T. S. Nguyen, J.-W. Park, W. Shiu, L. Urpi, J. S. Yoon, et al. An international model comparison study of controlled fault activation experiments in argillaceous claystone at the Mont Terri Laboratory. *International Journal of Rock Mechanics and Mining Sciences*, 136: 104505, 2020.

Jonny Rutqvist and Chin-Fu Tsang. A study of caprock hydromechanical changes associated with co 2-injection into a brine formation. *Environmental Geology*, 42: 296–305, 2002.

M. O. Saar. Geothermal heat as a tracer of large-scale groundwater flow and as a means to determine permeability fields. *Hydrogeology Journal*, 19(1):31, 2011.

M. O. Saar and M. Manga. Depth dependence of permeability in the oregon cascades inferred from hydrogeologic, thermal, seismic, and magmatic modeling constraints. *Journal of Geophysical Research: Solid Earth*, 109(B4), 2004.

M.O. Saar. Novel geothermal technologies, in: Potentials, costs and environmental assessment of electricity generation technologies. Technical report, Swiss Federal Office

of Energy, Swiss Competences Center for Energy Research "Supply of Electricity" and "Biomass for Swiss Energy Future", Bern, Switzerland, 2017.

EA Sammel, SE Ingebritsen, and RH Mariner. The hydrothermal system at newberry volcano, oregon. *Journal of Geophysical Research: Solid Earth*, 93(B9):10149–10162, 1988.

J. Sausse. Hydromechanical properties and alteration of natural fracture surfaces in the Soultz granite (Bas-Rhin, France). *Tectonophysics*, 348(1-3):169–185, 2002.

J. Schmittbuhl, S. Lambotte, O. Lengliné, M. Grunberg, H. Jund, J. Vergne, F. Cornet, C. Doubre, and F. Masson. Induced and triggered seismicity below the city of Strasbourg, France from November 2019 to January 2021. *Comptes Rendus. Géoscience*, 353(S1):561–584, 2021.

R. Schneeberger, M. de La Varga, D. Egli, A. Berger, F. Kober, F. Wellmann, and M. Herwegh. Methods and uncertainty estimations of 3-D structural modelling in crystalline rocks: a case study. *Solid Earth*, 8(5):987–1002, 2017.

P. Segall and S. Lu. Injection-induced seismicity: Poroelastic and earthquake nucleation effects. *Journal of Geophysical Research: Solid Earth*, 120(7):5082–5103, 2015.

R. Seithel, E. Gaucher, B. Mueller, U. Steiner, and T. Kohl. Probability of fault reactivation in the bavarian molasse basin. *Geothermics*, 82:81–90, 2019.

P. Selvadurai, P. A. Selvadurai, and M. Nejati. A multi-phasic approach for estimating the biot coefficient for Grimsel granite. *Solid Earth*, 10(6):2001–2014, 2019.

H. A. Sheldon, A. Wilkins, and C. P. Green. Recovery efficiency in high-temperature aquifer thermal energy storage systems. *Geothermics*, 1234:1234–1234, 2021. doi: 1234.

P. Siebert. *Laborversuche zur hydraulischen Risserzeugung in dreiaxial belasteten Granitquadern-Grundlagen, Versuchsentwicklung,-durchfuehrung und Analyse*. PhD thesis, Dissertation, RWTH Aachen University, 2017, 2020.

P. Siebert, C. Clauser, and M. Ziegler. Laborversuche zur hydraulischen risserzeugung in dreiaxial belasteten granitquadern-grundlagen, versuchsentwicklung,-durchführung und analyse. Technical report, Lehrstuhl für Geotechnik im Bauwesen und Institut für Grundbau, 2017.

A.W. Skempton. The pore-pressure coefficients A and B. *Géotechnique*, 4(4):143–147, 1954.

R. Y. Smith, M. Lesueur, U. Kelka, T. Poulet, and D. Koehn. Using fractured outcrops to calculate permeability tensors: implications for geothermal fluid flow and the influence of seismic-scale faults. *Geological Magazine*, 159(11-12):2262–2278, 2022.

D. T. Snow. *A parallel plate model of fractured permeable media*. University of California, Berkeley, 1965.

H. Soltanzadeh and C. D. Hawkes. Assessing fault reactivation tendency within and surrounding porous reservoirs during fluid production or injection. *International Journal of Rock Mechanics and Mining Sciences*, 46(1):1–7, 2009a.

H. Soltanzadeh and C. D. Hawkes. Induced poroelastic and thermoelastic stress changes within reservoirs during fluid injection and production. *Porous Media: Heat and Mass Transfer, Transport and Mechanics*, 27:27–57, 2009b.

E. Sonnenthal, N. Spycher, O. Callahan, T. Cladouhos, and S. Petty. A thermal–hydrological–chemical model for the enhanced geothermal system demonstration project at Newberry Volcano, Oregon. In *Proceedings of the 37th Workshop on Geothermal Reservoir Engineering, Stanford, CA*, volume 30, 2012.

A. Stathas and I. Stefanou. Fault friction under thermal pressurization during large seismic-slip: Numerical analyses and extension of the model of frictional slip. *International Journal of Mechanical Sciences*, 248:108184, 2023.

E.B. Tadmor, R.E. Miller, and R.S. Elliott. *Continuum mechanics and thermodynamics: from fundamental concepts to governing equations*. Cambridge University Press, 2012.

B.F. Tchanche, M. Pétrissans, and G. Papadakis. Heat resources and organic Rankine cycle machines. *Renewable and Sustainable Energy Reviews*, 39:1185–1199, 2014.

K. Terzaghi. *Theoretical soil mechanics*. 1943.

Y. W. Tsang and P. A. Witherspoon. Hydromechanical behavior of a deformable rock fracture subject to normal stress. *Journal of Geophysical Research: Solid Earth*, 86 (B10):9287–9298, 1981.

F.J. Turner and L.E. Weiss. Structural analysis of metamorphic tectonites. *Geological Society of America Bulletin*, 74:153–166, 1963.

P. Vardon, D. Bruhn, A. Steiginga, B. Cox, H. Abels, A. Barnhoorn, G. Drijkoningen, E. Slob, and K. Wapenaar. A geothermal well doublet for research and heat supply of the TU Delft campus. *arXiv preprint arXiv:2003.11826*, 2020.

R. Vörös and S. Baisch. Induced seismicity and seismic risk management–a showcase from the Californië geothermal field (the Netherlands). *Netherlands Journal of Geosciences*, 101:e15, 2022.

W. Wagner and A. Pruß. The IAPWS formulation 1995 for the thermodynamic properties of ordinary water substance for general and scientific use. *Journal of Physical and Chemical Reference Data*, 31(2):387–535, 2002.

L. Wang, G. Kwiatek, M. Bohnhoff, E. Rybacki, and G. Dresen. Injection-induced fault slip and associated seismicity in the lab: Insights from source mechanisms,

local stress states and fault geometry. *Earth and Planetary Science Letters*, 626: 118515, 2024.

N. Watanabe, W. Wang, J. Taron, U.J. Görke, and O. Kolditz. Lower-dimensional interface elements with local enrichment: application to coupled hydro-mechanical problems in discretely fractured porous media. *International Journal for Numerical Methods in Engineering*, 90(8):1010–1034, 2012.

Q. Wenning, C. Madonna, A. de Haller, and J.P. Burg. Permeability and seismic velocity anisotropy across a ductile–brittle fault zone in crystalline rock. *Solid Earth*, 9(3):683–698, 2018.

A. Wilkins, C.P. Green, and J. Ennis-King. Porousflow: a multiphysics simulation code for coupled problems in porous media. *Journal of Open Source Software*, 5(55): 2176, 2020. doi: 10.21105/joss.02176.

A. Wilkins, C. P. Green, and J. Ennis-King. An open-source multiphysics simulation code for coupled problems in porous media. *Computers & Geosciences*, 154:104820, 2021. doi: 10.1016/j.cageo.2021.104820.

P.A. Witherspoon, J.S.Y. Wang, K. Iwai, and J.E. Gale. Validity of cubic law for fluid flow in a deformable rock fracture. *Water Resources Research*, 16(6):1016–1024, 1980.

Z. Ye and A. Ghassemi. Injection-induced shear slip and permeability enhancement in granite fractures. *Journal of Geophysical Research: Solid Earth*, 123(10):9009–9032, 2018.

I. W. Yeo, M. H. De Freitas, and R. W. Zimmerman. Effect of shear displacement on the aperture and permeability of a rock fracture. *International Journal of Rock Mechanics and Mining Sciences*, 35(8):1051–1070, 1998.

H. Yoo, S. Park, L. Xie, K.-I. Kim, K.-B. Min, J. Rutqvist, and A. P. Rinaldi. Hydro-mechanical modeling of the first and second hydraulic stimulations in a fractured geothermal reservoir in Pohang, South Korea. *Geothermics*, 89:101982, 2021.

Y. Yuan, T. Xu, J. Moore, H. Lei, and B. Feng. Coupled thermo–hydro–mechanical modeling of hydro-shearing stimulation in an enhanced geothermal system in the Raft River Geothermal Field, USA. *Rock Mechanics and Rock Engineering*, 53: 5371–5388, 2020.

C. Zaal, A. Daniilidis, and F.C. Vossepoel. Economic and fault stability analysis of geothermal field development in direct-use hydrothermal reservoirs. *Geothermal Energy*, 9(1):12, 2021.

F. Zhang, M. An, L. Zhang, Y. Fang, and D. Elsworth. Effect of mineralogy on friction-dilation relationships for simulated faults: Implications for permeability evolution in caprock faults. *Geoscience Frontiers*, 11(2):439–450, 2020.

R.W. Zimmerman. Compressibility of two-dimensional cavities of various shapes. 1986.

R.W. Zimmerman. Compressibility of sandstones. 1990.

R.W. Zimmerman and G.S. Bodvarsson. Hydraulic conductivity of rock fractures. *Transport in Porous Media*, 23:1–30, 1996.

G. Zimmermann and A. Reinicke. Hydraulic stimulation of a deep sandstone reservoir to develop an enhanced geothermal system: Laboratory and field experiments. *Geothermics*, 39(1):70–77, 2010.

M. D. Zoback, F. Rummel, R. Jung, and C. B. Raleigh. Laboratory hydraulic fracturing experiments in intact and pre-fractured rock. In *International Journal of Rock Mechanics and Mining Sciences & Geomechanics Abstracts*, volume 14, pages 49–58. Elsevier, 1977.

M. D. Zoback, C. A. Barton, M. Brudy, D. A. Castillo, T. Finkbeiner, B. R. Grollimund, D. B. Moos, P. L. Peska, C. D. Ward, and D. J. Wiprut. Determination of stress orientation and magnitude in deep wells. *International Journal of Rock Mechanics and Mining Sciences*, 40(7-8):1049–1076, 2003.

M.D. Zoback. *Reservoir geomechanics*. Cambridge University Press, 2010.

Appendix A

List of publications, conferences attendances and organised

Publications

- **Josselin Ouf**, Julian Osten, Wen Luo, Kavan Khaledi, Mohammadreza Jalali, Philip J. Vardon, Florian Amanna - *Experimental and numerical analysis of injection-induced permeability changes in pre-existing fractures* - Published - Geomechanics for Energy and the Environment - 2024
  Ouf et al. [2024b]

- **Josselin Ouf**, Wen Luo, Kavan Khaledi, Mohammadreza Jalali, Philip J. Vardon, Florian Amann - *Numerical Modeling of Hydro-Mechanical Processes during Hydraulic Testing of Pre-existing Fractures at the Grimsel Test Site, Switzerland* - Published - Geomechanics for Energy and the Environment - 2024
  Ouf et al. [2024a]

- **Josselin Ouf**, Philip J. Vardon, Kavan Khaledi, Wen Luo, Mohammadreza Jalali, Florian Amann - *Numerical Analysis of Far-Field Fault Reactivation Induced by Reservoir Cooling* - Published - Geothermics - 2025
  Ouf et al. [2025]

- Wen Luo, Joaquin Liaudat, **Josselin Ouf**, Anne Catherine Dieudonne, Florian

Amann, Philip J. Vardon - *Numerical modelling of fracturing processes during cold water injection into geothermal reservoirs: Verification and qualitative validation* - Published - Computers and Geotechnics - 2025
Luo et al. [2025]

- Wen Luo, Anne-Catherine Dieudonne, **Josselin Ouf**, Florian Amann, Philip Vardon. *A numerical tool to simulate fatigue damage under cyclic coupled thermo-hydro-mechanical processes* - International Journal of Rock Engineering and Mining Science - Submitted - 2025

Poster presentations

- **Josselin Ouf**, Kavan Khaledi, Mohammadreza Jalali, Wen Luo, Florian Amann, Philip J. Vardon - *Large scale cooling induced stress changes around deep geothermal reservoirs* - Efficiency and Safety in Geothermal Operations Workshop - Delft, NL - September 2021

- **Josselin Ouf**, Kavan Khaledi, Mohammadreza Jalali, Wen Luo, Florian Amann, Philip J. Vardon - *Numerical Modeling of Short-term HM processes during Hydraulic Stimulation at the Grimsel Test Site* - Efficiency and Safety in Geothermal Operations Workshop - Aachen, DE - April 2022

- **Josselin Ouf**, Kavan Khaledi, Mohammadreza Jalali, Wen Luo, Florian Amann, Philip J. Vardon - *Numerical Validation of Hydro-Shearing Using Laboratory-Scale Experiments* - GSE Research Day - Delft, NL - October 2023

- **Josselin Ouf**, Kavan Khaledi, Mohammadreza Jalali, Wen Luo, Florian Amann, Philip J. Vardon - *Numerical Simulation of Hydraulic stimulation and its Verification Using Laboratory-Scale Experiments* - Efficiency and Safety in Geothermal Operations Workshop - Volterra, IT - May 2023

- **Josselin Ouf**, Kavan Khaledi, Mohammadreza Jalali, Wen Luo, Florian Amann, Philip J. Vardon - *Numerical Simulation of Hydraulic stimulation and its Verifi-*

cation Using Laboratory and Field Scale Experiments - DECOVALEX - Troyes, FR - November 2023

- **Josselin Ouf**, Kavan Khaledi, Mohammadreza Jalali, Wen Luo, Florian Amann, Philip J. Vardon - *Numerical Analysis of Far-Field Fault Reactivation Induced by Reservoir Cooling* Efficiency and Safety in Geothermal Operations Workshop - Zurich, CH - July 2024

Talks

- **Josselin Ouf**, Kavan Khaledi, Mohammadreza Jalali, Wen Luo, Florian Amann, Philip J. Vardon - *Large scale cooling induced stress changes around deep geothermal reservoirs* - Efficiency and Safety in Geothermal Operations Workshop - Delft, NL - September 2021

- **Josselin Ouf**, Kavan Khaledi, Mohammadreza Jalali, Wen Luo, Florian Amann, Philip J. Vardon - *Numerical Modeling of Short-term HM processes during Hydraulic Stimulation at the Grimsel Test Site* - Efficiency and Safety in Geothermal Operations Workshop - Aachen, DE - April 2022

- **Josselin Ouf**, Kavan Khaledi, Mohammadreza Jalali, Wen Luo, Florian Amann, Philip J. Vardon - *Comparison of two approaches for modelling fracture opening due to cold water injection in geothermal reservoir* - Symposium on Energy Geotechnics - Delft, NL - October 2023

- **Josselin Ouf**, Kavan Khaledi, Mohammadreza Jalali, Wen Luo, Florian Amann, Philip J. Vardon - *Numerical Analysis of Far-Field Fault Reactivation Induced by Reservoir Cooling* Efficiency and Safety in Geothermal Operations Workshop - Zurich, CH - July 2024

Conference organiser/support

- Organiser of European Geothermal Ph.D Day 2022 - Aachen - Germany
- Support of Symposium on Energy Geotechnics 2023 - Delft - The Netherlands
- Organiser of European Geothermal Ph.D Day 2024 - Delft - The Netherlands

Appendix B

Curriculum Vitae

Josselin Noel Marcel Ouf

Birth date: 13/09/1996

Place of birth: Mont-Saint-Aignan

Nationality: French

Experience

- Ph.D Student / 2021 – 2025
  TU Delft and RWTH Aachen - Germany and The Netherlands
- Engineer in Geotechnics / 2019 – 2020
  Hydrogeotechnique - France
- Teaching Assistant / 2017 – 2018
  Ecole Polytechnique de l'Université Grenoble - France

Education

- M.Sc Geotechnics and Civil Engineering / 2016 - 2019
  Ecole Polytechnique de l'Université Grenoble-Alpes - France
- B.Sc Civil Engineering / 2014 - 2016
  Université du Havre - France